Summer 2020

Enhancing Single and Two-Phase Heat Transfer of Microgap Heat Sinks Using Nano-Structure Coatings

Yueyang Zhao

Enhancing Single and Two-phase Heat Transfer of Microgap Heat Sinks using Nano-Structure Coatings

by

Yueyang Zhao

Bachelor of Engineering
Huazhong University of Science and Technology, 2012

Master of Science
Lehigh University, 2015

Submitted in Partial Fulfillment of the Requirements

for the Degree of Doctor of Philosophy in

Mechanical Engineering

College of Engineering and Computing

University of South Carolina

2020

Accepted by:

Chen Li, Major Professor

Jamil Khan, Committee Member

Yi Wang, Committee Member

Guoan Wang, Committee Member/Outside Member

Cheryl L. Addy, Vice Provost and Dean of the Graduate School

Acknowledgments

I would like to express my deepest and sincere gratitude to my advisor Professor Chen Li. The solid knowledge and foundation of Dr. Li's research work and his innovative thinking and encourage me all the time. His enthusiasm in new technology, methodology and conscientious attitude keep me engaged in my research. I received all necessary help and support during the past five years. I will never forget the times when I felt stressed and lack of study motivation, Dr. Li offered advice and encouragement all the time without hesitation. Without his persistent guidance, my doctoral dissertation would not be completed.

I am very thankful to Professor Jamil Khan, Professor Yi Wang and Professor Guoan Wang for spending time serving on my committee and providing constructive suggestions on my dissertation. They have provided not only professional guidance but also recommendations for potential future work and life wisdom. I would also like to thank Professor Yan Tong for her support during the collaboration, who gave insightful suggestions on two-phase heat transfer and many brilliant ideas on my research work. Many thanks are also to all the professors and faculty members in the department of mechanical engineering for teaching me knowledge and providing various resources and help during my doctoral life.

Last but not the least, I am grateful that my family and friends always support and encourage me to follow my heart and pursue my dream, especially when I was struggling and doubted on my research. Many thanks to their support and love.

Abstract

Due to the shrinking size and increasing power of electronics, the heat flux generated by electronic devices has greatly increased and imposed challenges to thermal management technologies. Numerous cooling technologies have been developed to cool high-power electronics. Among them, flow boiling in microchannels or a microgap has been one of the most efficient ways to remove high heat flux, which requires less coolant compared with single-phase cooling techniques. However, the flow boiling instability is the one of the most challenging issues, which lead to the premature critical heat flux (CHF) conditions and deteriorate heat transfer rate. The capillary force generated along the microchannel or microgap can enhance the liquid rewetting process and hence, delay CHF conditions. Moreover, flow boiling heat transfer coefficient (HTC) can also be enhanced because of promoting thin liquid film evaporation.

Superhydrophilic surfaces can greatly enhance the capillary force in the microchannel or microgap. In this study, a new kind of superhydrophilic nano-structure (CuO) coatings have been developed and applied in the copper microgap. Microgap heat sinks with superhydrophilic nano-structured walls have been systematically characterized. Deionized (DI) water was selected as the coolant. The microgap dimension is 26 mm $\times$ 5.5 mm $\times$ 0.3 mm (length, width, height). Heat was applied on the bottom surface. Single and two-phase heat transfer has been characterized with flow rates ranging from $151 kg/m^2s$ to $757.7 kg/m^2s$ on both bare and black CuO coated surfaces. Visualization studies show the high-frequency rewetting processes and two-layer flow were observed in the entire flow channel, which can significantly enhance the thin film evaporation and delay the dry-out process and increase the CHF. The

CHF on the black CuO coated surface can be enhanced nearly 3 times compared with that on the bare surface at all flow rates. The 170% higher HTC has been realized compared with the bare surface. Higher supersaturations prior to surface flooding cause the decreasing of the surface temperature. Surface temperature became more uniform on the black CuO coated surface because of high frequency rewetting process and thin film evaporation. Note that all enhancements have been achieved only with slightly elevated pressure drop.

Table of Contents

List of Tables

List of Figures

Chapter 1

Introduction

1.1 Motivation to Study

In the past few decades, thermal controlling became more and more critical for almost all kinds of engineering applications, such as power plants, fuel cells, electronic devices, etc (Rovira et al., 2011; Faghri and Guo, 2005; Garimella, 2006). How to release heat from heated surface or body rapidly and efficiently has become a hot topic nowadays. Due to the higher resolution of the nano-fabrication applied to the shrinking electronic integrated circuitry, the thermal issues has become more challenging. The heat flux generated from powerful micro/nano electronic devices has significantly risen these years. Moreover, the power consumption trend shows that the heat density would keep increasing at the module and system level with advancement of technology (Hannemann, 2003; Schaller, 1997). The heat removal target for the coming years would be up to $600W/cm^2$ from micro-nano-chips (Kandlikar et al., 2005). In addition, in recent years on-chip power supply and demands of increasing performance have resulted in larger non-uniform chip heat dissipation, creating localized hot spots, easily exceeding $1kW/cm^2$ in heat flux, and $1kW/cm^3$ in heat density (Bar-Cohen, Wang, and Rahim, 2007). Conventional air cooled designs are no longer enough to remove heat flux higher than $100W/cm^2$ because of the technology limits (Fang, 2011). Thus, advanced cooling solutions are in great demand for the thermal management of increasing powerful electronics.

Two-phase heat transfer can achieve relatively high heat transfer coefficient and reduce power by taking advantage of the latent heat (Zalba et al., 2003; Dai, 2013). Boiling and evaporation are the two primary kinds of two-phase heat transports (Dai, 2013). Using latent heat by evaporation or boiling can significantly increase heat removal from high power density and high heat flux electronics. In this study, we would apply microscale two-phase heat transfer to remove the heat generated by the power supply mainly on copper substrate.

1.2 Introduction of Pool Boiling

In the pool boiling, vapor is generated on a superheated wall, which is smaller compared to a large body of liquid. The fluid near the heated surface relatively moves mainly due to the buoyancy effect. If more heat is applied to the surface, the temperature of the liquid near the surface might reach or exceed the equilibrium saturation temperature. Nucleation boiling occurs when the vapor embryo is formed on the heated surface.

The shape of the vapor embryo is decided by contact angle and interfacial tension in general, and the shape of the surface itself as well. The formation of a vapor embryo occurs in a system with constant liquid temperature and pressure. If the surface is flat, the vapor embryo would be like as shown in Figure 1.1(Phan, 2010).

Once the nucleation is initiated, bubble would grow from the heated solid surface and then detach. The complete process of the boiling cycle includes liquid heating, nucleation, bubble growth and departure. Three main features that affect the heat transfer rate are bubble departure diameter, bubble departure frequency and the number of nucleation sites. The bubble departure frequency is related to the duration of bubble growth time and the waiting time.

Over the past decades, the bubble departure diameter has been the subject of numerous studies. In the experimental studies, bubble departure diameter is typically

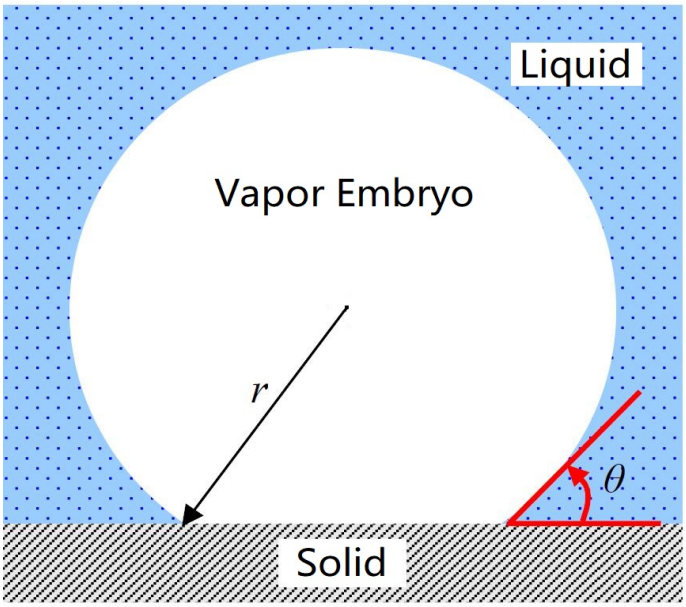

Figure 1.1: Vapor embryo formed at the flat surface with a contact angle θ.

measured from the high speed cameras which could record boiling process. A number of correlations were investigated to estimate the bubble release diameter. The capillary length is an important role in the correlations, and the capillary length can be determined by surface tension force and buoyancy. The density of nucleation sites was found to be related to the contact angles. The correlations are widely used in the boiling studies. However, they are based on a limited quantity of experimental data so that the accuracy has not been verified so far.

Pooling boiling heat transfer regimes are easily understood by referred to as pooling boiling curve. The regimes of pool boiling are indicated in Figure 1.2. The pool boiling curve can be analysed in four regimes, the natural convection, the nucleate boiling, the transition region and film boiling, respectively. Among them, the natural convention and nucleate boiling were discussed in a majority of studies.

During the natural convection, liquid motions are created to remove heat from the heated surface to the liquid surface due to the temperature gradients. The driving force of liquid motions is considered to be the buoyancy force as a result of the fluid density gradients. While more heat is applied to the surface, the superheat is large

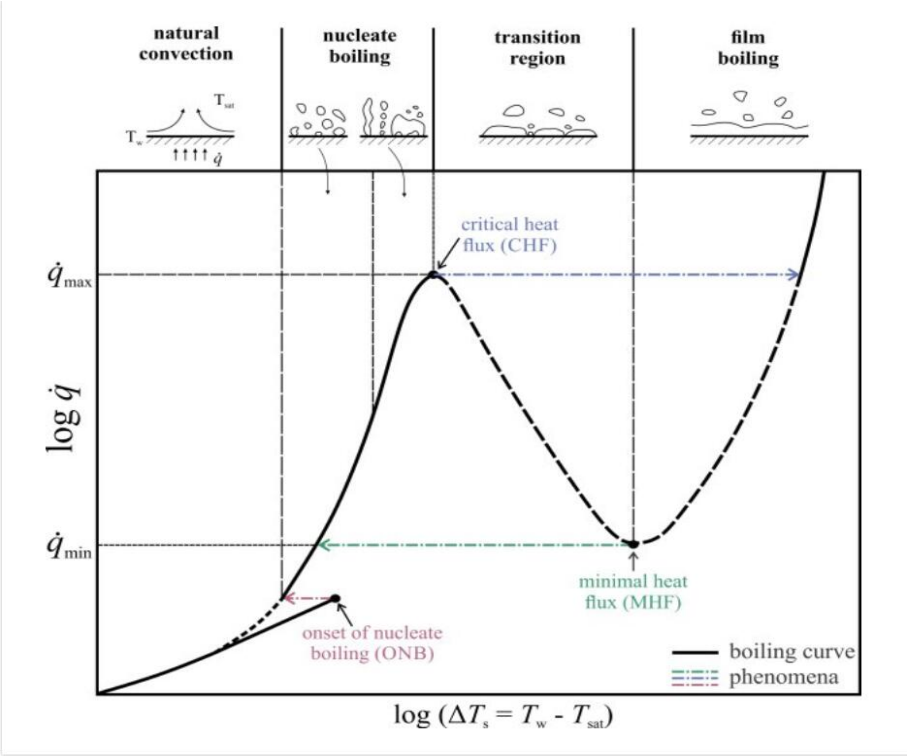

Figure 1.2: Graphical representation of the pool boiling curve.

enough to generate bubbles, and nucleation is initiated at the cavities on the surface. This process is called onset of nucleate boiling. When the superheat is low, bubbles start to form on the surface. More and more bubble are formed on more cavities as the superheat increases. The bubble frequency increases at each site of the surface. Then the nearest bubbles merge together and grow in vertical or horizontal direction. With the continually increasing of the superheat, a vapor film is formed across the surface due to the the bubble coalescence. The vapor film is adjacent to the heated surface instead of the liquid. The heat transfer performance suddenly decreases because of the poor thermal conductivity of vapor. At this point, the heat flux is called the critical heat flux (CHF), which describes the thermal limit of the boiling. The CHF is also the maximum heat flux of the boiling process. Burnout will happen if a higher heat flux, compare to CHF, is applied to the surface.

1.3 Introduction of Flow Boiling

Flow boiling is discussed a lot for circulation of a fluid by using external means such as a pump. The flow boiling process shows that vapour and liquid are in joint motion inside pipes or channels. Boiling would occur on the channel wall and the flow-patterns could vary due to vapour production.

1.3.1 Two-phase Flow Parameters

The classic parameters to characterize a two-phase flow are described as follows.

Superficial velocities

The superficial velocities of vapour and liquid phases are denoted as j_v and j_l,

$$j_v = \frac{G_x}{\rho_v} \tag{1.1}$$

$$j_l = \frac{G(1-x)}{\rho_l}. \tag{1.2}$$

These two velocities equal the velocity of each phase if it circulates at its specified mass flow rate through the channel alone.

Vapor quality

The total mass flow rate $\dot{m}$ equals the summation of the mass flow rates of vapour $\dot{m}_v$ and liquid $\dot{m}_l$ through the channel, which satisfies $\dot{m} = \dot{m}_v + \dot{m}_l$. The vapor quality denoted as x is the ratio of vapor flow to total flow, expressed as $x = \frac{\dot{m}_v}{\dot{m}}$. This parameter x is always determined by establishing an energy balance,

$$x = \frac{q - GC_p(T_s - T_l)}{GH_{lv}}, \tag{1.3}$$

where q is the heat flux, G is the mass velocity defined as $G = \dot{m}/A_c$, C_p is the liquid specific heat and H_{lv} is the vaporisation latent heat of liquid and saturation. Also note that T_l and T_s are the liquid and saturation temperatures, respectively. For the mass velocity G expression, A_c is the cross-section area of the channel.

Void fraction

The void fraction denoted as ε, is one of the main parameters used to characterize two-phase flow. The parameter ε is of great significance in models to predict pressure drop, heat transfer or flow pattern transition. To specify void fraction, different geometric definitions are used, such as local, chordal, cross-sectional and volumetric. The most widely applied definition is the cross-sectional void fraction, which is the ratio of the area occupied by the vapour phase $A_{c,v}$ to the overall area at a cross section A_c,

$$\varepsilon = \frac{A_{c,v}}{A_c}. \tag{1.4}$$

In this definition, the mean velocities of liquid and vapour phases at a cross section in terms of the vapour quality x are given as,

$$U_l = \frac{G}{\rho_l}(\frac{1-x}{1-\varepsilon}), \tag{1.5}$$

$$U_v = \frac{G}{\rho_v}(\frac{x}{\varepsilon}). \tag{1.6}$$

Therefore, the void fraction is expressed as

$$\varepsilon = \frac{1}{1+\frac{1-x}{x}\frac{\rho_v}{\rho_l}S}, \tag{1.7}$$

where S is the velocity ratio or referred to as the slip ratio, and is expressed as $S = \frac{U_v}{U_l}$. For equal velocities in the homogeneous model, we have $S = 1$. U_v is always greater than U_l for upward and horizontal flows, which leads to $S \geq 1$. For downward vertical flows, U_v tends to be less than U_l due to gravity effects and results in $S \leq 1$.

1.3.2 Conventional microchannels flow boiling regimes

The horizontal flow boiling is of great research interest, which schematically shows the flow regimes in Figure 1.3. Bubbly flow can be frequently observed at relatively low vapour quality. Also, bubbles flow appear mainly in the upper portion of the channel due to buoyancy. Coalescence of small bubbles occurs when the vapour

quality increases, which further produces larger plug-type bubbles. This is referred to as plug flow regime.

Stratified flow can be observed when the liquid and vapour are separated in the case of low flow rates and relatively higher vapour qualities. Moreover, for the regime of the stratified flow, if the flow rate is sufficient high to make the liquid-vapour interface unstable, the interface tends to turn wavy. This type of flow is called the wavy flow, which has strong vapour shear on the interface that ejects liquid droplets in the vapour core flow. For higher liquid flow rates, the amplitude of the waves may grow, and form large slug-type bubbles, which is referred to as the slug flow.

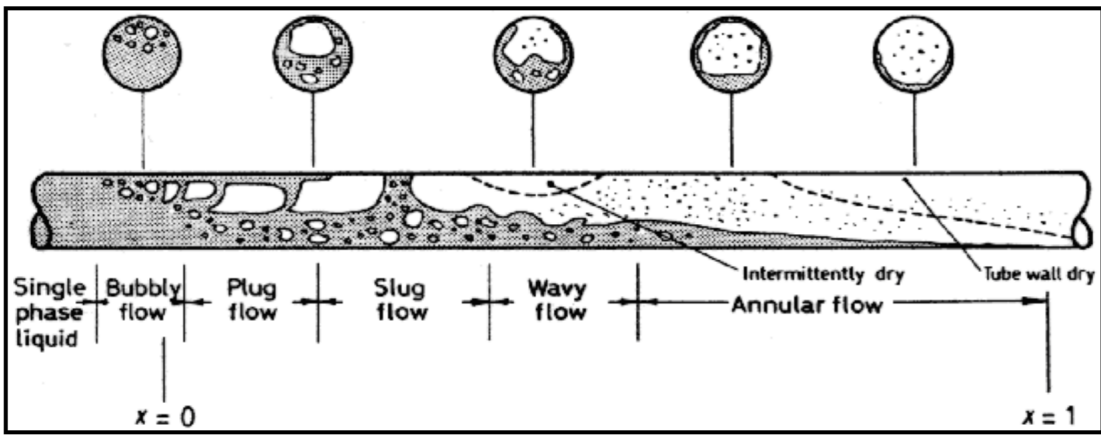

Figure 1.3: Graphical show of flow boiling regimes in a horizontal channel.

Annular flow could be observed for high velocity of vapour and moderate velocity of liquid, and this type of regime is characterized by a thin liquid film on the top of a channel and a thicker liquid film on the bottom of the channel.

1.3.3 Microchannels Flow boiling

The heat transfer phenomena in flow boiling will change as the flow passage size is reduced from macroscale to microscale. However, only part of the available knowledge about macroscale phenomena can be transferred to the microscale.

TRANSITION

From previous studies, the transition from macroscale to microscale in heat transfer was classified by different methods based on the hydraulic diameter, the point at which boiling nucleation is altogether suppressed, or the threshold to confined bubble flow (Thome, 2004). The transition criteria considering the size threshold of hydraulic diameter (Mehendale, Jacobi, and Shah, 2000; Kandlikar and Grande, 2003) have some limits itself, since they do not reflect the influence of channel size on the physical mechanisms. Specifically, they include bubble form and flow transition. The criterion of nucleation suppression (Lin, 1991) results in a critical hydrodynamic diameter on the order of 1 to 2 μm or less, therefore, it is probably better assigned to the micro-to-nanoscale transition. The standard to confined bubble flow (Kew and Cornwell, 1997; Ullmann and Brauner, 2007) is probably the most convenient criterion, because the confinement number C_o, which is defined as the ratio of the capillary length to the hydrodynamic diameter, can be used as a criterion to differentiate between macroscale and microscale flow boiling. The confinement number C_o is calculated as

$$C_o = \left[\frac{\sigma_{lv}}{g(\rho_l - \rho_v)D_h^2}\right]^{1/2}, \tag{1.8}$$

where D_h is the hydrodynamic diameter.

Heat transfer and flow patterns will be significantly different from those observed in convectional size channels. Kew and Cornwell (1997) suggested the criterion of $C_o \geq 0.50$, however, the criterion was recommended by Ullmann and Brauner (2007) as $C_o \geq 0.79$.

Microchannels Flow Patterns

Capillary effects are very important in microchannels to reduce stratification of the liquid. Hence, the channel orientation is mostly of secondary importance. The flow patterns in microchannels were observed by various research groups in the past

decades (Kew and Cornwell, 1997; Serizawa, Feng, and Kawara, 2002; Revellin and Thome, 2007). Similar to the macroscale situation, it is often not feasible to conduct a solid comparison between independent databases, since different variables were used to describe the same pattern. Generally, two-phase flows in microchannels can have four principal flow patterns described in Revellin and Thome (2007). The graphical view of these flow patterns is shown in Figure 1.4.

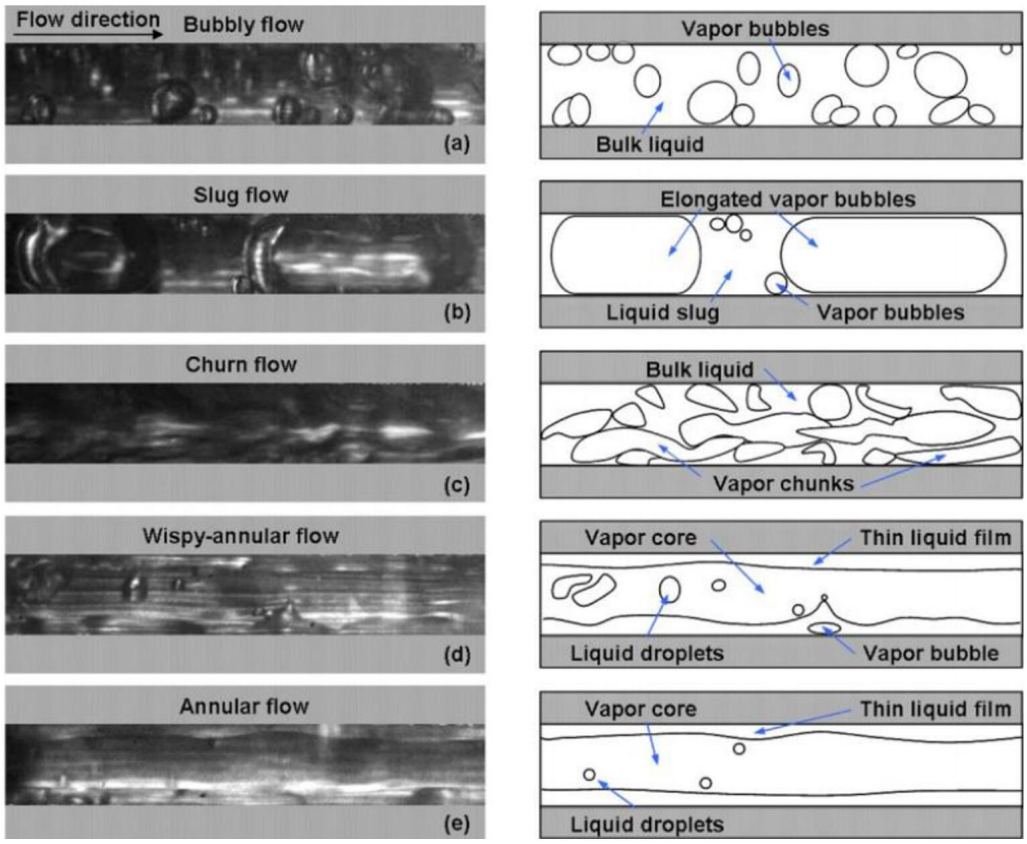

Figure 1.4: Graphical representation of principal flow patterns in microchannel.

Discrete bubbles move inside the liquid phase in bubbly flow. Typically, these bubbles are smaller in diameter than the hydrodynamic diameter of a channel. This type of flow pattern covers the very small vapour qualities range. On the contrary, the bubbles have approximately the same diameter as the channel in slug flow. The bubble nose is hemispherical while the vapour phase is separated from the wall by a thin liquid film. These bubbles are called "elongated bubbles", since they tend to

become longer due to the confinement effect. The liquid phase exists mostly in the liquid slugs which would separate successive vapour bubbles.

Semi-annular flow can be observed when the vapour quality increases. This flow pattern is referred to as the continuous vapour phase at a channel core with some churning liquid zones at the wall. The churning liquid zones are actually created by deformation and coalescence of the previous elongated bubbles. When the churning liquid zones disappear, the flow regime is categorized as annular flow.

MICROCHANNELS DRYOUT

The local heat transfer coefficient tends to increase in microchannel flow boiling as the heat flux tends to reach a critical value of the vapour quality. Beyond that critical value, its deterioration occurs. The deterioration of the heat transfer coefficient is assumed to be caused by the intermittent dryout, which is an unstable breakdown of the liquid film in contact with the wall. As an example of the observation of intermittent dryout, Figure 1.5 from the paper of Caney, Marty, and Bigot (2006) shows that the investigated experimental study of flow boiling of HFE-7100 has 0.84 mm hydraulic diameter for 40 parallel rectangular channels. The critical vapour quality was shown to decrease as the mass velocity increases. The authors also observed the occurrence of intermittent dryout, irrespective of variation of heat flux and mass velocity, at a unique critical value of the total superficial velocity denoted as j, which is expressed as

Madrid, Caney, and Marty (2007) conducted experiments following the same conditions as in Caney, Marty, and Bigot (2006) and got the similar observations. In addition, their experimental results showed no obvious influence of the heat flux on the heat transfer coefficient at a given vapour quality.

Callizo, Ali, and Palm (2008) used refrigerants R-134a, R-22 and R-245fa as working fluids to study the flow boiling in a circular vertical microchannel with internal

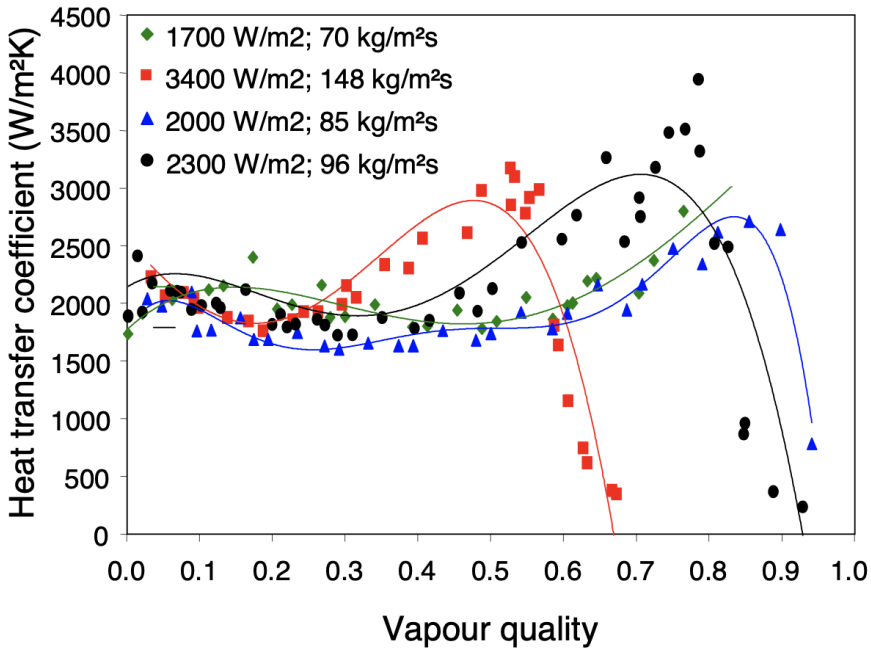

Figure 1.5: Local heat transfer coefficient for different vapour quality.

diameter of 640 μm. As a result, a decrease of the critical vapour quality was observed when the vapour velocity increased. The force balance between gas shear and liquid surface tension was used to explain the intermittent dryout phenomenon.

To summarize from previous studies, the intermittent dryout is more likely due to hydrodynamical instabilities rather than thermal fluctuations. High shear force would make the liquid-vapour interface wavy and cause intermittent dryout if the wave amplitude becomes greater than the liquid film thickness. This method was used by Revellin and Thome (2008) to predict the critical heat flux under uniform or non-uniform heat fluxes in microchannels, which provides a good prediction for a large number of experimental data.

1.4 Wetting Phenomena

For heterogeneous boiling, the nature of the contact between the vapour, liquid and heated surface could highly impact the heat and mass transfer. This type of contact

is mainly dominated by the surface tension forces at scales less than the capillary length, and is also referred to as the wetting phenomena. Knowledge of wetting principle or laws is crucial in understanding and interpreting boiling physics, such as bubble growth in nucleate boiling or dryout in microscale flow boiling.

When liquid drop is small enough to neglect the gravity flattening action, its sticking on a solid surface is referred to as the surface wettability. An important parameter used to characterize the surface wettability is the contact angle denoted as θ made by the liquid on the solid. The solid surface is defined as "wetted" if $\theta < 90°$ (Figure 1.6 and is "unwetted" if $\theta \geq 90°$ (Figure 1.6). In terms of water, the wetted surface is called "hydrophilic" surfaces and the unwetted surface is called "hydrophobic" surfaces.

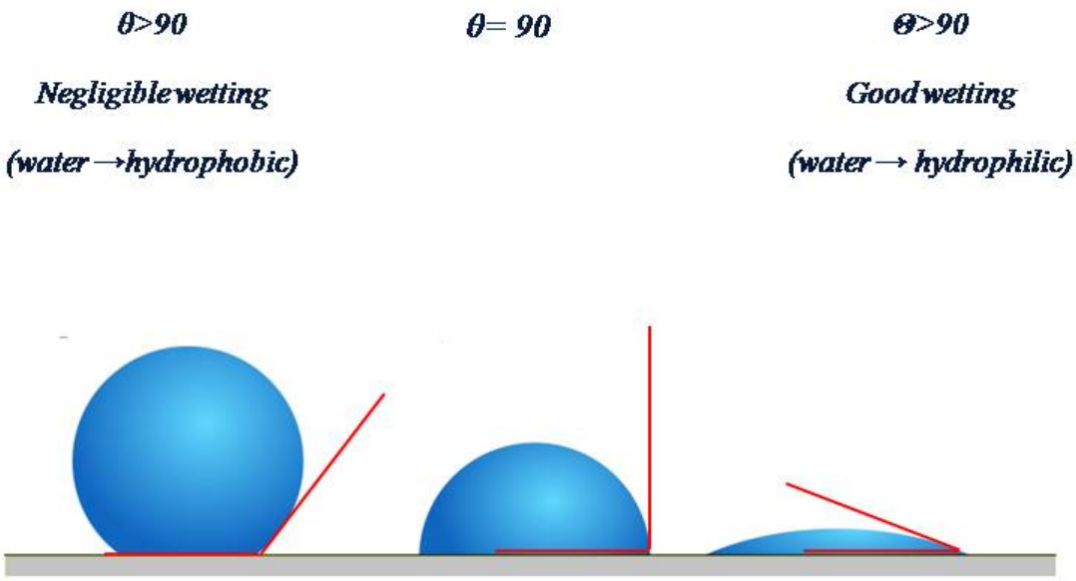

Figure 1.6: Wetting under different conditions of θ.

Young's relation

Young (1805) first discussed the value of the contact angle θ. At the base of the liquid droplet, there are three phases, solid, liquid and vapour coexisting in the "triple

contact line" (TCL). Each interface has the TCL to minimize the corresponding surface area. Thus, balancing the surface tensions on the direction of potential motion, specifically, the horizontal, would enable to determine the contact angle such that

$$\cos\theta = \frac{\sigma_{sv} - \sigma_{sl}}{\sigma_{lv}} \tag{1.9}$$

where σ_{sl}, σ_{sv}, σ_{lv} are the surface tensions, which is the energy for each unit surface of the interface of solid-liquid, solid-vapour and liquid-vapour, respectively.

Contact angle

Solid surface is generally imperfect due to the heterogeneity on surface roughness and chemistry. It can also be polluted by the deposition of external contaminants which float in air. The defects allow the TCL to pin on the surface and generate multiple values for the observed contact angle. This is the so-called contact angle hysteresis (Figure 1.7), which is usually quantified by the measurement of the contact angle with varying the droplet volume (Quéré, 2005).

First, a small droplet is deposited on the solid surface. The measured contact angle equals the static contact angle θ_e as shown in Figure 1.7 (a). The droplet is then slowly fed by using a syringe. The diameter of the TCL will gradually increase if the contact angle is unique. However, the TCL frequently remains pinned, and at the same time the angle is observed to increase. If the droplet volume stops increasing, the contact angle would remain stuck at its last value, which is one of the most possible observable angles. There is a critical value of the droplet volume, beyond which the TCL suddenly widens and the contact angle reaches the maximum value, so-called the "advancing contact angle" θ_a (Figure 1.7 b). On the contrary, decreasing the droplet volume enables observing the minimum contact angle, below which the TCL reduces. This angle is called the "receding contact angle" θ_r (Figure 1.7 c). The contact angle hysteresis is defined as the difference of the advancing and receding contact angles. This phenomenon can also be observed on an inclined solid surface

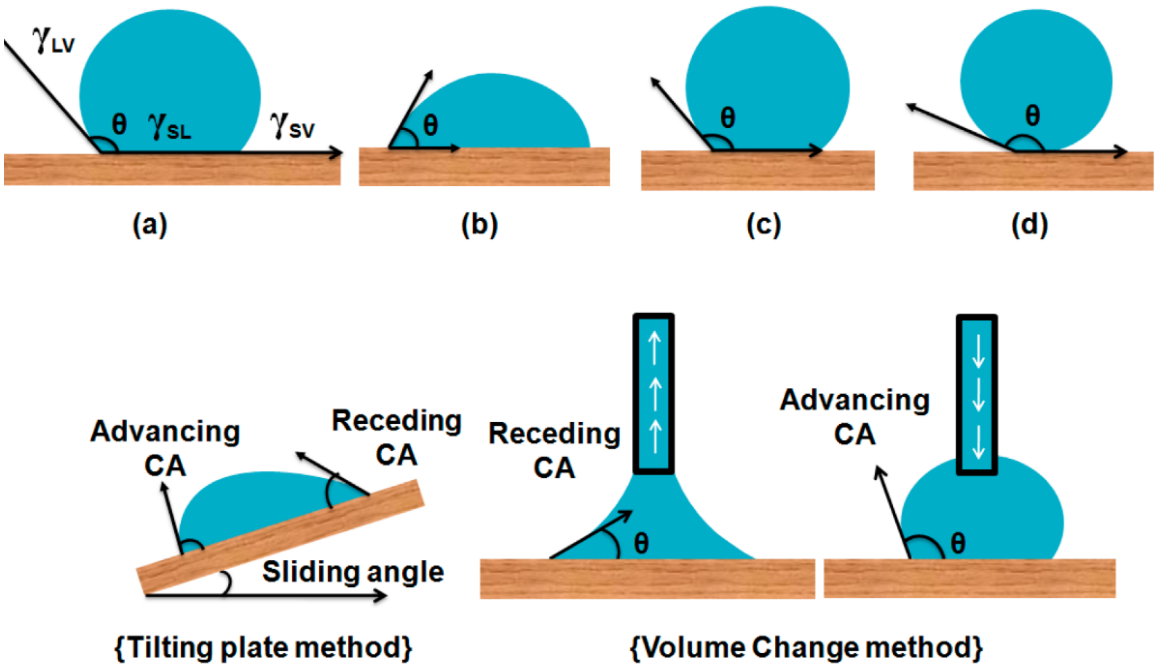

Figure 1.7: Contact angle hysteresis: a) static contact angle θ_e, b) advancing contact angle θ_a, c) receding contact angle θ_r, and d) contact angles of droplet on a inclined surface (Ahmad and Kan, 2016).

where the angle is greater in the front than that on the rear of the droplet (Figure 1.7 d).

Adhesion energy

Due to the gravity, a droplet would necessarily run down on an inclined surface when the contact angle were unique. However, it will still stick on the surface for a threshold of inclined angle. In fact, the contact angle hysteresis generates a capillary force that opposes the gravity. This force would reach its criticle value on the front and rear angles of θ_a and θ_r, respectively. To characterize this adhesion of a liquid droplet on a solid surface, Dupré and Dupré (1869) defined the solid-liquid adhesion energy W_{sl}^a as

$$W_{sl}^a = \sigma_{sv} + \sigma_{lv} - \sigma_{sl}. \tag{1.10}$$

By combining equations (1.9) and (1.10), the well-known Young-Dupré equation is written as

$$W_{sl}^{a} = \sigma_{lv}(1 + \cos\theta). \tag{1.11}$$

1.4.1 SOLID SURFACE TENSION THEORIES

As discussed in the previous sections, the contact angle is a result of minimization of the system energy and can be determined by a balance of the surface tensions. The surface tension of liquid-vapour or called liquid surface tension, is easy in application and can be measured by a variety of techniques. However, that of solid-vapour or called solid surface tension, is more complicated since it cannot be directly measured. In general, the values of the solid surface tension are calculated from a set of contact angles, developed by bringing various liquids in contact with the solid surface. However, there is no universal agreement in literature about its definition. The two most well- known theories are discussed as follows.

ZISMAN THEORY

The Zisman (1964)'s theory is probably the most widely used definition of solid surface tension. Zisman (1964) defined the solid surface tension as the highest liquid-vapour surface tension that a liquid should completely wet the solid surface with a contact angle of θ°. This because the contact angle decreases if the liquid surface tension decreases in general. Figure 1.8 presents an example of how Zisman's theory can be applied. The solid surface is a poly (ethylene) film on which the contact angles of various liquids are measured (Rulison, 1999). According to the Zisman definition, poly (ethylene) has a surface tension of $22.8 mN/m$.

For the surface science, the solid-liquid surface interactions are categorized into the polar types and the dispersive types. The polar interactions account for dipole-dipole, dipole-induced dipole, hydrogen bonding, and other site-specific interactions.

The dispersive interactions account for Van der Waals and other non-site specific interactions. A polar surface is capable of polar-type interactions with liquids. Generally, the Zisman theory works best for non-polar surfaces,such as poly (ethylene) and poly (propylene). However, it becomes inadequate for polar surfaces, such as glasses, ceramics and metals. This is because the Zisman theory is a single parameter model and it only considers the overall values of the surface tensions.

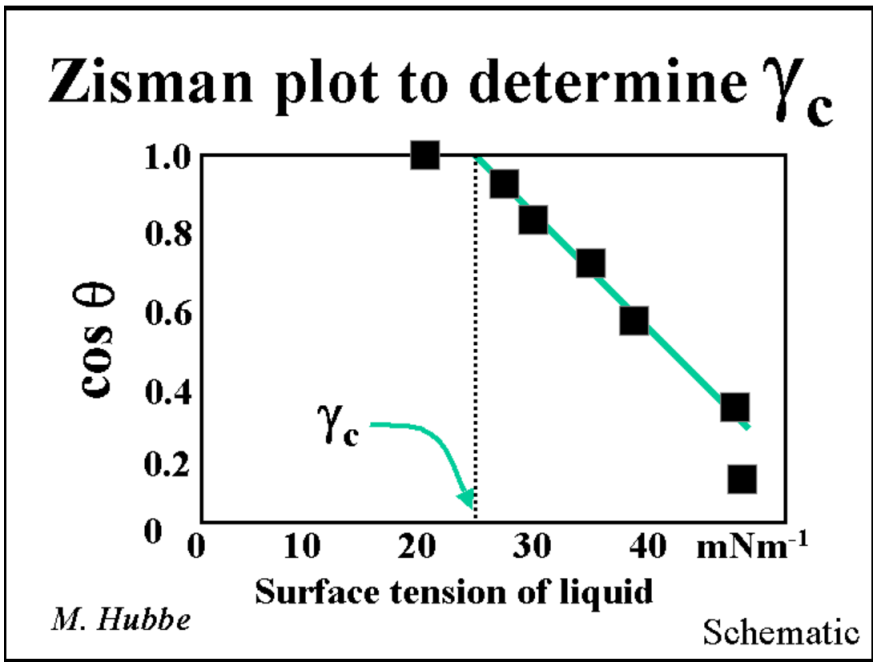

Figure 1.8: Determination of the solid surface tension by Zisman theory.

Owens/Wendt Theory

The Owens/Wendt theory is mostly applicable to surfaces that have low surface charge and are moderately polar in nature. This theory has some limits because it leaves the selection of liquids being used up to the experimenter. Further based on the equation of Owens and Wendt (**??**), Fowkes (1964) suggested a method to determine the solid surface tensions by using contact angle data from two reference liquids, such as diiodomethane and water. Diiodomethane has no polar component to its overall surface tension, thus enables to calculate the dispersive solid surface

tension. Water has both polar and dispersive to its surface tension. It can then be used after diiodomethane and enables the determination of the polar solid surface tension.

Owens and Wendt (1969) developed a theory which accounts for polar-type interactions between liquids and solids surfaces. This theory is based on the equation in Young (1805) and Good and Girifalco (1960) which defines the solid-liquid surface tension as,

$$\sigma_{sl} = \sigma_{sv} + \sigma_{lv} - 2\left(\sigma_{lv}^{D}\sigma_{sv}^{D}\right)^{1/2} - 2\left(\sigma_{lv}^{P}\sigma_{sv}^{P}\right)^{1/2} \tag{1.12}$$

where σ_{lv}^{D} and σ_{lv}^{P} are the dispersive and polar components of the liquid surface tension, and σ_{sv}^{D} and σ_{sv}^{P} are these components of the solid surface tension, respectively.

Once all the values of the liquid surface tensions and the equivalent contact angles are given, the solid surface tensions can be determined by plotting Y versus X. The polar and dispersive solid surface tensions can be calculated from the slope and the intercept of the fit line to the Y/X curve. The overall tension is the summation of these two components.

1.4.2 Effect of surface roughness on wetting

Wetting of a liquid on a solid surface is impacted not only by the surface chemistry, but also by the surface topography. Two distinct models, developed independently by Wenzel (1936) and Cassie and Baxter (1944) which is also called the Cassie model, are commonly used to explain the effect of surface roughness on the apparent area of contact angle of liquid drops.

Wenzel model

Wenzel (1936) is the first person to analyze the effect of surface roughness on the static contact angle. He observed that surface roughness caused a wetted surface to

behave as if it were more wetted, and an unwetted surface to behave as if it were more unwetted. Hence, Wenzel (1936) suggested to modify Young's equation (1.9) by multiplying the numerator of the right side of the equation (1.9) by a roughness factor, r, which is defined as the ratio of the actual area to the apparent area of the contact surface,

$$\cos\theta = r\cos\theta_{smooth} \tag{1.13}$$

where θ_{smooth} is the contact angle measured on a smooth surface of the same material, given by the Young's equation (1.9) as $\cos\theta_{smooth} = (\sigma_{sv} - \sigma_{sl})/\sigma_{lv}$.

Cassie model

The Cassie model (Cassie and Baxter, 1944), on the other hand, postulates that the hydrophobic nature of a rough surface is caused by microscopic pockets of air remaining trapped below the liquid droplet, which leads to a composite interface (Figure 1.9). Defining Φ_s as the fraction of the solid in contact with the liquid, the Cassie equation has

$$\cos\theta = -1 + \Phi_s(1 + \cos\theta_{smooth}). \tag{1.14}$$

Compared to the Wenzel relation, the Cassie model enables the possibility for the case of $\theta > 90°$ even when $\theta_{smooth} < 90°$. The transition from the Wenzel to the Cassie state was observed (He, Patankar, and Lee, 2003; Lafuma and Quéré, 2003) at a critical contact angle θ_{cr} , which is calculated by the equations (1.13) and (1.14) and lead to

$$\cos\theta_{cr} = \frac{\Phi_s - 1}{r - \Phi_s}. \tag{1.15}$$

The critical contact angle is necessarily greater than 90° when $r > 1 > \Phi_s$. Thus, it may be expected that for $\theta < 90°$, a surface cannot exist in the Cassie state or that the creation of highly non-wetting surfaces with $\theta >> 90°$ requires $\theta > \theta_{cr} > 90°$.

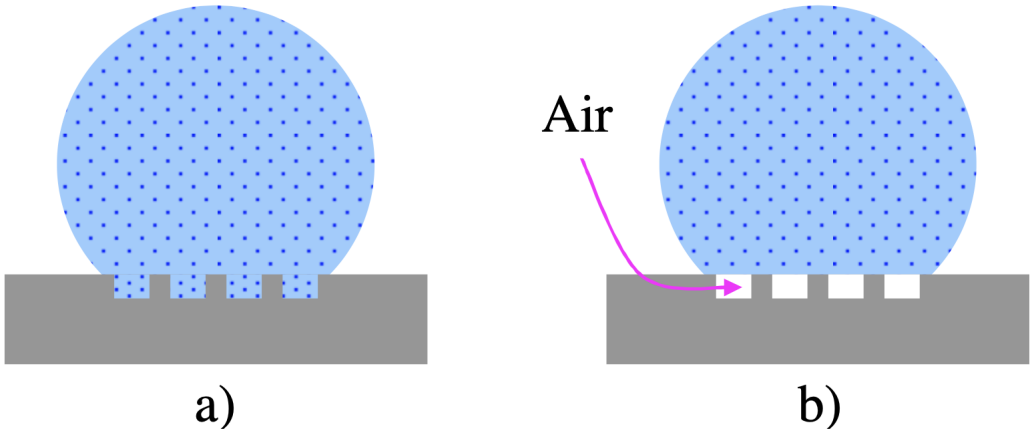

Figure 1.9: Graphical view of a water droplet on a hydrophobic surface, in a) Wenzel state and b) Cassie state.(Phan, 2010)

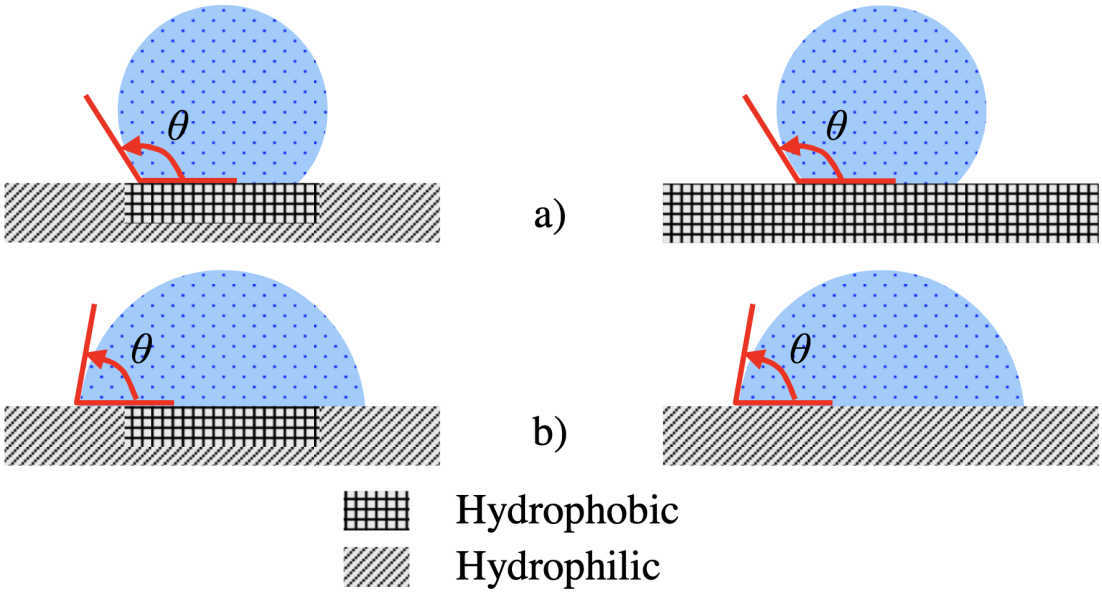

Figure 1.10: Contact angle behaviour determined by solid-liquid interactions at the TCL: a) inside the hydrophobic zone, the water contact angle equals that on the hydrophobic surface and b) if the TCL exceeds the hydrophobic zone, the contact angle equals to that on the hydrophilic surface.(Phan, 2010)

The validation of both the Wenzel and Cassie models were questioned in some previous research work. Previous researchers used three types of two-component surfaces that contain "spots" in a surrounding field, a hydrophilic spot in a hydrophobic field, a rough spot in a smooth field, and a smooth spot in a rough field. They measured water contact angles within the spots and with the spot confined to within the TCL of the droplet. The results show that contact angle behaviour (advancing, receding, and hysteresis) is determined by the interactions of the solid and the liquid at the TCL only, and that the interfacial area within the contact perimeter is not relevant. Figure 1.10 provides an illustration to better understand the suggestion in Gao and McCarthy (2007).

1.5 Microscale Two-Phase Heat Transfer

Microscale two-phase transport is defined as heat transfer and mass transfer in microscale liquid and gas flows. Two-phase flow could occur in different forms, one of which is that flow transit from pure liquid phase towards vapor phase as a consequence of external heat input separated flows. One phase is present in the form of bubbles, droplets and so on in a continuous carrier phase. However, microscale two-phase flow mechanism is significantly different from that of the conventional channels due to the capillary forces in microgaps or microchannels.

With different vapor qualities of the flow, various flow patterns were observed in microchannels as shown in Figure 1.11. Bubbly flow, bubbly-slug flow, slug flow, annular flow are primary flow patterns of two-phase flow in microchannels (Mudawar, 2001; Kandlikar, 2002a; Serizawa, Feng, and Kawara, 2002; Hetsroni et al., 2003). The bubble flow is a type of flow such that small bubbles, whose diameters are smaller than the channel hydraulic diameter, are dispersed or suspended in a liquid continuum. The bubble growth and bubble sizes are influnced by subcooled flow boiling (Wang and Cheng, 2009). When bubble nucleation is generated in a saturated

flow, the small bubbles would gradually grow until reach the solid boundaries of the channel, and then the bubbles would be confined and elongated along microchannels.

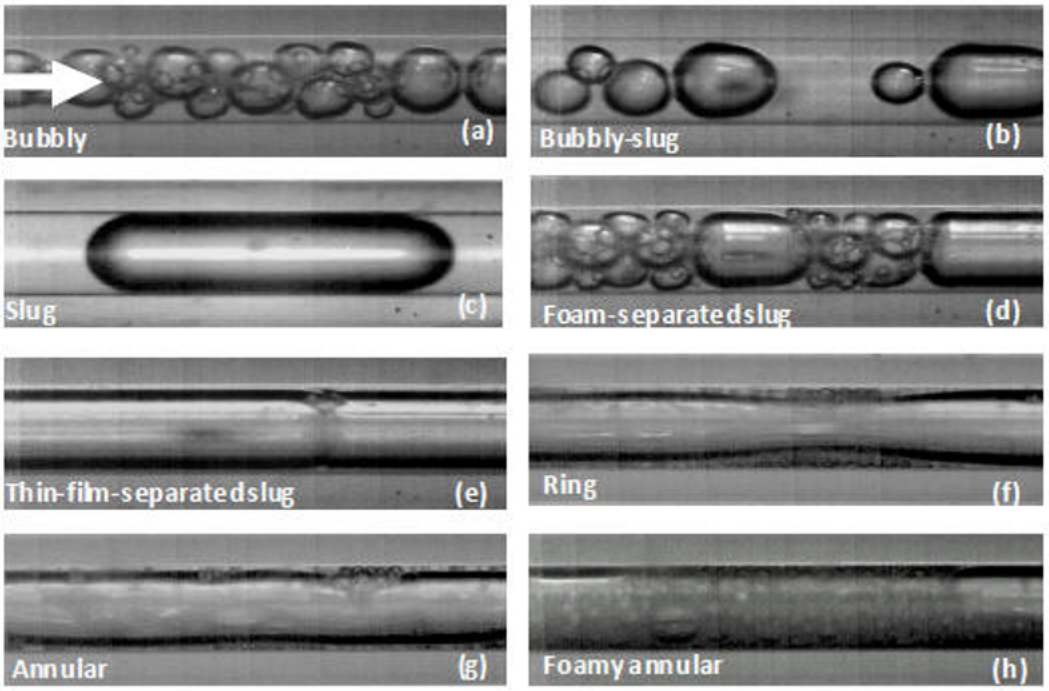

Figure 1.11: Two-phase flow patterns

The elongated bubbles would coalesce into larger size bubbles quickly before bubbly-slug flows are formed along the microchannel as shown in Figure 1.11. However, the slug flow would increase the pressure drop a lot, which may induce a local dry-out (Serizawa, Feng, and Kawara, 2002). Additionally, fast growing vapor slug also may induce reverse flow back to the liquid inlet direction, so that the rewetting process would be hindered. Annular flow is characterized by the presence of a thin liquid film flowing on the wall of the channel with the gas flowing in the gas core as shown in Figure 1.11.

The transitions between different flow patterns of two-phase flow seem to be unpredictable in both microgap and microchannel. Critical flow transition types include the liquid two-phase alternating flow and the liquid two-phase vapor alternating flow (Wu and Cheng, 2003; Wu and Cheng, 2004; Wu, Cheng, and Wang, 2006). These

transitions caused the problems in controlling or stabilizing heat and mass transfer in microchannel. Severe instability of heat and mass transfer in microchannel were observed in some previous studies (Wu and Cheng, 2003; Wu and Cheng, 2004; Wu, Cheng, and Wang, 2006; Bergles and Kandlikar, 2005; Kuo and Peles, 2008; Kuo and Gau, 2010).

The upstream compressible is usually a consequence of the reserve flow in a two-phase flow. The bubbles flow reversely into the subcooled inlet and would cause the condensation between vapor bubbles and subcooled liquid. High inlet pressure of the flow in microchannel may also compress the vapor size. Constant liquid flow rate, therefore, could not be sustained in microchannel. Different flow patterns have their own unique heat transfer modes, such as bubbly flow in nucleate boiling, bubbly slug flow or annular flow in thin-film evaporation. During the nucleation flow, dry-out area on the solid walls could result in the fast increasing of surface temperature and the decreasing of heat transfer coefficient (Bergles and Kandlikar, 2005; Bar-Cohen and Rahim, 2009; Boure, Bergles, and Tong, 1973). The instabilities of two-phase heat transfer along a microchannel usually lead to unstable wall temperatures and premature CHF.

1.6 Microgap and Microchannel Heat Sinks

Among different key cooling strategies, microchannel heat sink has been proven to be a high-performance cooling technique mode to dissipate high heat fluxes from electronic devices. Microchannel heat sink is usually to use a high thermal conductivity solid as the substrate such as copper, silicon, aluminum with microgap or parallel microchannels (Qu, 2004). Over the past decades, high-resolution micro-nano-fabrication technique, such as chemical etching, ion beam, electron beam etching, has greatly improved the fabrication of microchannel on silicon substrate. The shape of the channel cross-section can be triangular, rectangular, or trapezoidal, and typi-

cally a rectangular shape is usually used. The dimension of the microchannel varies from 10 μm to 1000 μm. Coolant such as water was pumped into the microchannel or microgap by a gear pump or a pressurized water tank. The coolant is used to release the heat which is generated by electronic devices. Depending on the heat conditions, the cooling fluid could be in single-phase state or two-phase state along the microchannel.

Chapter 2

Review on the Surface Treatment technology

Chapter 1 presents the benefits of enhanced surfaces in improving boiling heat transfer. Over the past decades, significant advances have been made in fabricating enhanced surfaces. Nowadays, the progress in micro- and nano- technologies enables the fabrication of enhanced surfaces on the lower (micro and nano) scales, where the mechanism of boiling enhancement is different. The wetting phenomenon can actually play an important role at these scales, hence its effects need to be considered in the boiling processes. Some investigations have been carried out to explore the impact of surface wettability on boiling, but few accurate experiments have been conducted so far due to the lack of technology to modify the contact angle without a large change in parameters.

In this chapter, the technology for surface treatment and the methods of surface characterization are described. The sample surfaces are micro-treated or nano-treated by physical techniques (physical vapour deposition) or chemical techniques (chemical vapour deposition). Microscale surface treatments are usually used to create artificial surface geometry, while nanoscale surface treatments can be used to change the surface wettability. Characterization of the surfaces was found by measurements of different parameters, such as surface geometry, surface roughness, contact angle of water or other liquid and thermal resistance. The determination of these parameters is crucial in understanding the physical mechanism at the solid-liquid and solid-vapor interface. This chapter focuses on the experimental principles that are referred to.

2.1 Surface Fabrication

Thin film coating technologies and patterning fabrication techniques have been widely developed over the past years, particularly for the electronic devices and information technology related components and systems. Their direct application in the fields of heat and mass transfer is the most recent and provides large expectations for making new surfaces that have not been assessed before in heat exchange and control systems. Table 2.1 summarizes the surface solutions realized in the present work (Phan, 2010). These studies mainly focused on heat transfer performance, structure and wettability functions which are important to the experimental heat-exchanger systems. Some popular surface-treatment conditions will be presented in the following subsections.

Material	Notation	Technique	Thickness	Function
Titanium	Ti	PVD	3-4 μm	Heating & structuring layer
Diamond-like carbon	DLC	PECVD	0.5-1 μm	Electrical-insulating & structuring layer
Low-carbon $PDMS^2$	SiOx	PECVD	$< 50nm$	Wetting Layer
High-carbon PDMS	SiOC	PECVD	$< 50nm$	Wetting Layer
Teflon-like	Teflon	PECVD	$< 50nm$	Wetting Layer
Iron Oxide	Fe_2O_3	MOCVD	$< 50nm$	Wetting Layer
Platinum	Pt	MOCVD	$< 50nm$	Wetting Layer

Table 2.1: Summary of Coating Processes.

2.2 Physical Vapour Deposition

Definition

Physical vapour deposition (PVD) is a variety of vacuum deposition process used to deposit thin films and coatings. PVD is characterized by a process of condensed phase meterial to a vaporized form of the material and then condense onto sample surfaces again to form a thin film on the surfaces(Mattox, 2010). The coating method involves purely physical processes such as high temperature vacuum evaporation or plasma sputter bombardment. The process of PVD include four steps:

- Evaporation of the material by a high energy source like ion beam or electron beam evaporates atoms from the surface,
- Transport the vapor to the substrate waiting to be coated,
- Reaction between the substrate atoms and the reactive gases such as nitrogen or oxygen,
- Deposit the coating on the substrate surface.

PVD are widely used to form coatings on the substrate because the coatings formed by PVD could have improved characteristics compared with bare substrate material. Moreover, the process is friendly compared with many other coating processes such as electroplating. However, PVD has problems with coating arbitrarily shaped surfaces. The cost of the devices and the coating processes are high and the processes of coating is complex.

Coatings by PVD

In PVD techniques, a physical process of releasing the materials to be deposited in to atomice particles, which are directed to the substrates in a vacuum environment. A higher flexibility of materials to be deposited and deposited films are the results of PVD. Two electrodes with a high voltage power supply and a vacuum chamber consitute the PVD as shown in Figure 2.1. (Billard and Perry, 2005). a illustrates the PVD reactor used in this study. The sputtering source is a magnetron that uses strong electric and magnetic fields to trap electrons close to the surface of the magnetron, which is known as the target (Figure 2.1 b).

For the sputtering process, layers of several materials are applied. A magnetron is placed near the raw material, which is the target substrate, in sputtering processes. In the vacuum chamber, one or several kinds of gases are introduced in. The gases

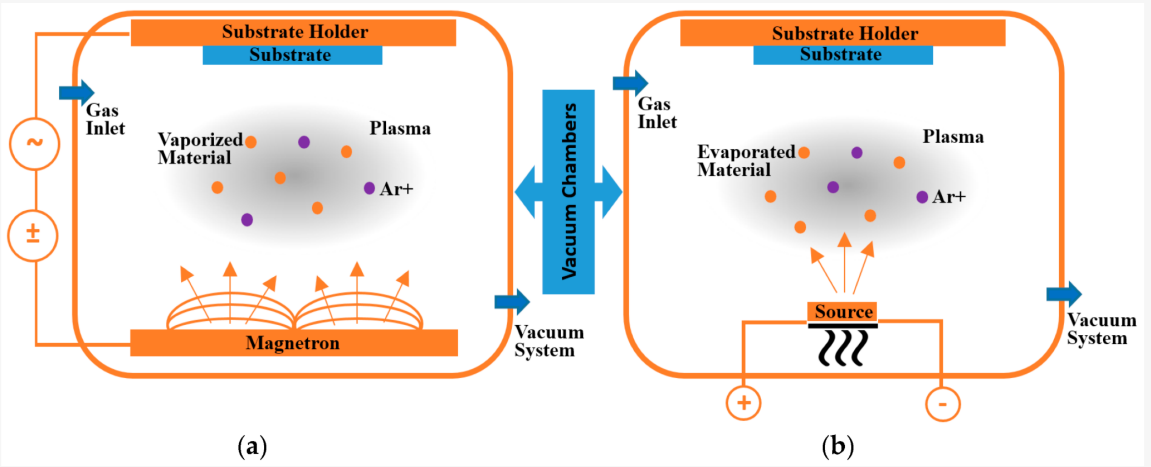

Figure 2.1: Schematic drawing of two conventional PVD processes: (a) sputtering and (b) evaporating using ionized Argon (Ar+) gas (Baptista et al., 2018).

velocity are controlled by a high voltage between the material and the target, producing atomic size particles from the target. These particles get kinetic energy by gas ions and then reached the target to the substrate and create a thin film on the substrate. However, PVD cannot control the film thickness accurately.

2.2.1 Chemical vapour deposition

Definition

Chemical vapour deposition (CVD) is another important process for producing thin films on solid substrates. In a typical CVD process, gas or vapor can react on the substrates at high temperature in a vacuum chamber as shown in figure (Figure 2.2). The gas, such as argon or helium, can be used to improve transport of precursor vapor in the deposition chamber and also to remove the by-products to protect the coatings. CVD techniques are developed for the growth of various nanosheets,such as graphene. By controlling CVD parameters such as temperature, gas velocity the growth of the coating can be tuned. Compare with other coating techniques, CVD has the highest level of controlling the fabrication of nanosheets. CVD offers massive production with high quality, purity and limit defects on the substrates. And the

coated productions are widely used in electronics and solar cell device, etc. However, higher cost is the issue for this technique. Figure 2.3 and figure 2.4 is a lab use CVD system for graphene coating.

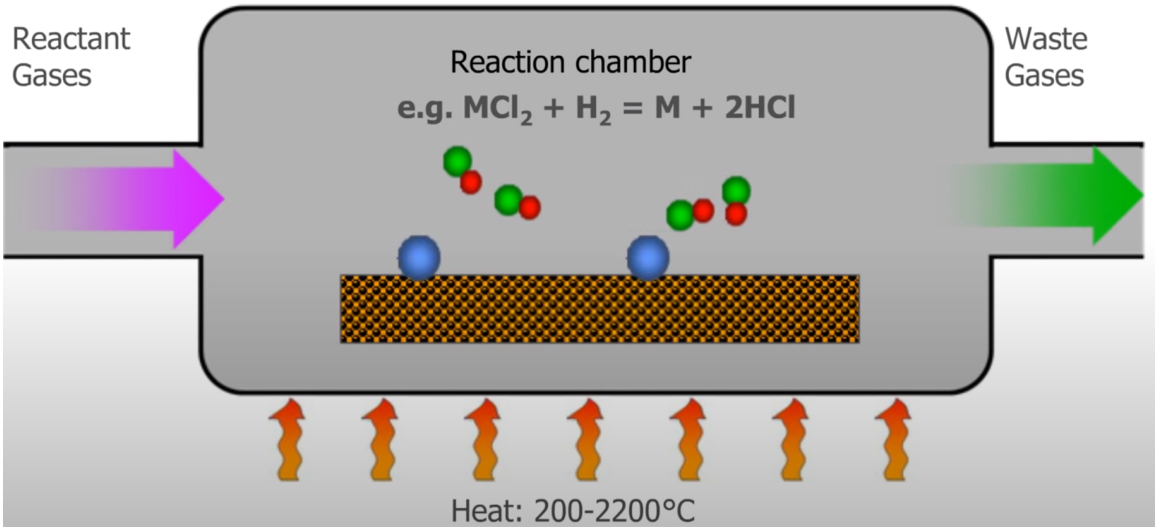

Figure 2.2: Sketch view of CVD processes.

Plasma enhanced chemical vapour deposition (PECVD) is the most common use in the lab. Compared with standard CVD teniques, PECVD do not require high operating temperatures. In the PECVD, the plasma is generated by radio frequency or AC, DC discharge between two electrodes. The space between them is filled with the reacting gases.

Metalorganic chemical vapour deposition (MOCVD) is a chemical vapour deposition process that uses organometallic precursors, which refer to compounds containing metal atoms bonded to organic radicals. In general, the metalorganic precursors undergo pyrolysis reactions. Moreover, compared to the conventional CVD process, MOCVD process requires a lower deposition temperature and provides higher deposition yield.

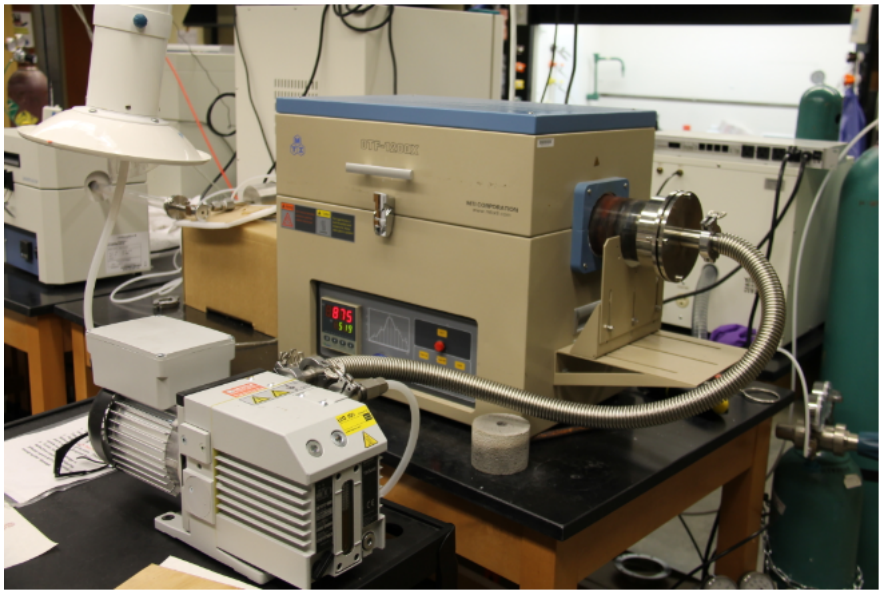

Figure 2.3: Lab use CVD reactor

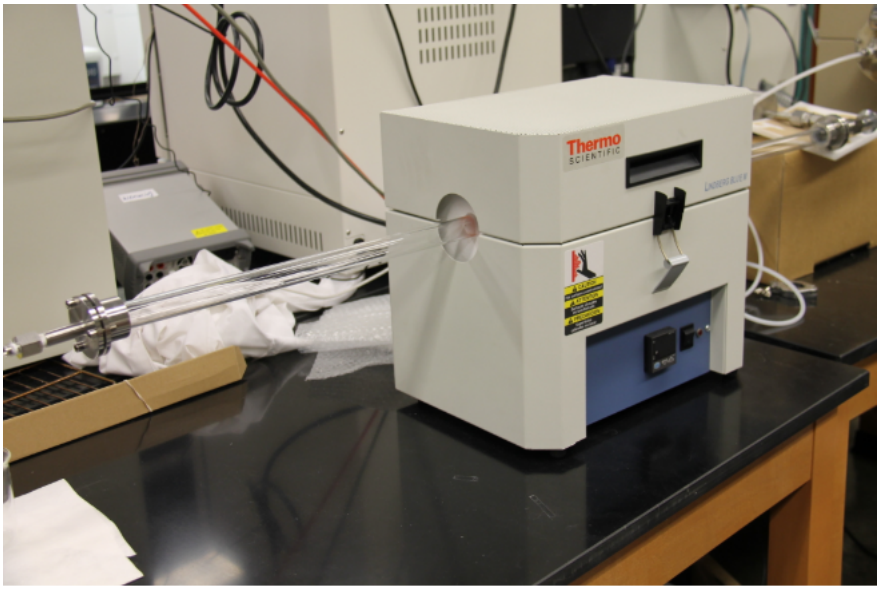

Figure 2.4: In-house built PECVD reactor for silicon oxide coatings.

2.2.2 Laser

Definition

Laser ablation is a direct-approach technique which has significant influence on machining and structuring materials. Applications cover high precision drilling, milling, fusion, and surface preparation, texturation and 2D-3D patterns with complex shapes at micro and nano scales (Billy et al., 2010). Similar to UV lithography, ions beam or electron beam, laser ablation enables the fabrication of micro- and nano- structured functional surfaces with a top-down approach. Ablation principle is that light, at the considered wavelength, is quickly absorbed by the very superficial layers of the target material. This absorption leads to the break of chemical bonds and further to the evaporation of the surface material (Figure 2.5). This technique is based on light-matter interaction (Chen et al., 2007).

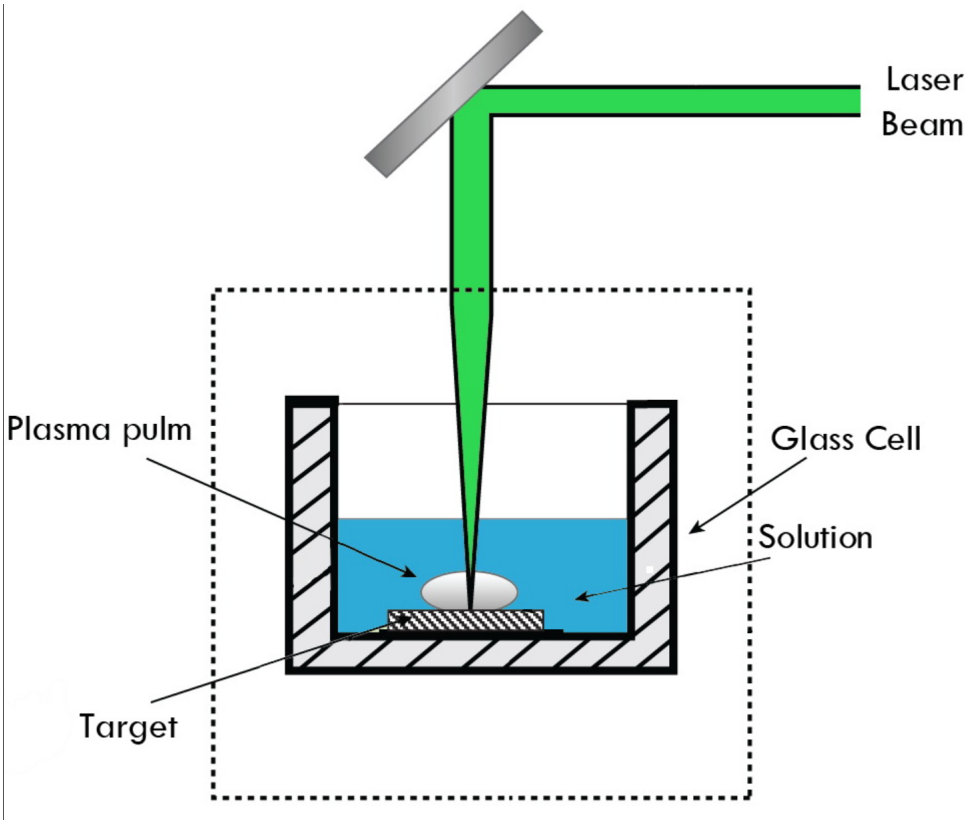

Figure 2.5: Schematic view of ablation process by laser beam.

2.3 Surface Characterization

This section discusses the techniques of surface characterization used in the present study. Micro and nanoscale images of a sample surface are obtained by using a scanning electron microscope (SEM). Atomic force microscope (AFM) is used for determination of the surface roughness. In order to quantify the surface wettability, the contact angle is measured by using the sessile drop technique with KRUSS Easy-Drop systems. Furthermore, the 4-wire technique is used for the measurement of the electrical resistance, enabling the determination of the sample temperature.

2.3.1 Contact angle measurement

The static contact angle is measured by the commercial system of KRÜSS EasyDrop DSA10 as shown in Figure 2.6. For a sample surface, the static contact angle is the mean value of the static contact angles measured at twenty distinct points uniformly distributed on the surface (five measurements are made at each point). The used technique is called "sessile drop technique" that consists of the following steps. First, a small droplet is deposited by a syringe pointed vertically down on to the sample surface. Afterwards, image of the droplet is captured by a charge coupled device camera (cf. Figure 2.7). Then, the captured image is analysed by KRÜSS software to determine the droplet contour and its baseline (the contact line between the droplet and the sample surface). Hence, the static contact angle is determined.

The higher image size and the higher number of pixels are available for evaluating the droplet contour. Therefore, the size of the droplet image should be adjusted to be as large as possible on the screen. Example of a good droplet picture for contact angle determination is shown in Figure 2.6. The width of the droplet is equal to about 2/3 of the width of the whole image. The contour of the droplet is light, without any parasite by light reflection from the sample surface. Lighting was adjusted so that the area above the baseline has a uniform brightness and so that the droplet contour

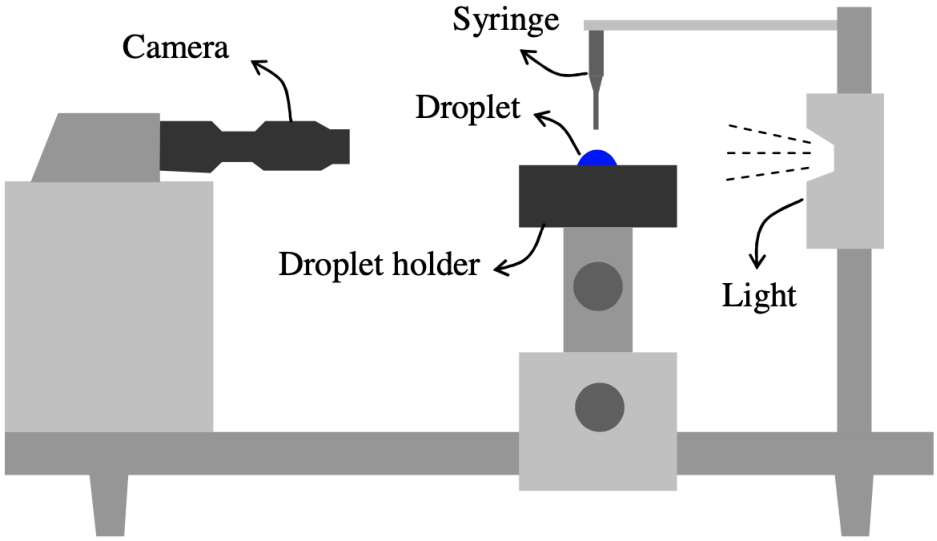

Figure 2.6: Block diagram of the KRÜSS EasyDrop DSA10 system.

is not clipped. The reflected image of the droplet should be light to enable an easy determination of baseline by the image analysis software.

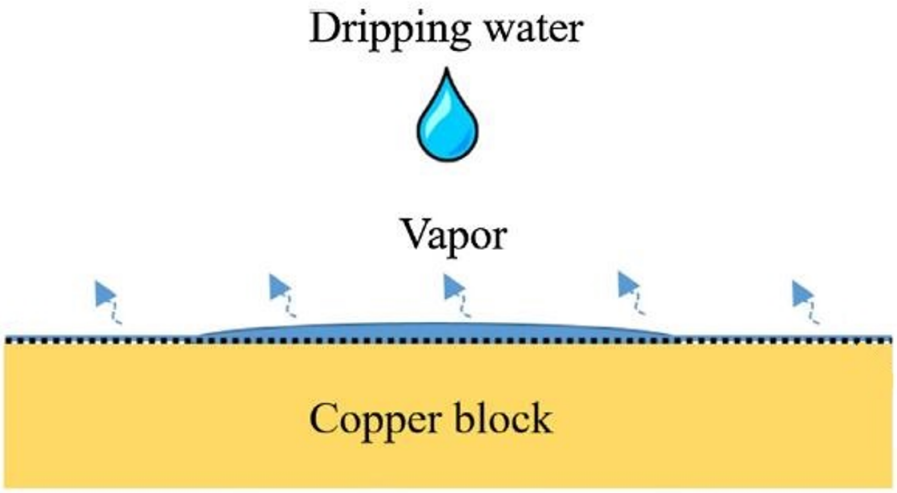

Figure 2.7: Diagram of a liquid droplet and its baseline (Wang et al., 2017).

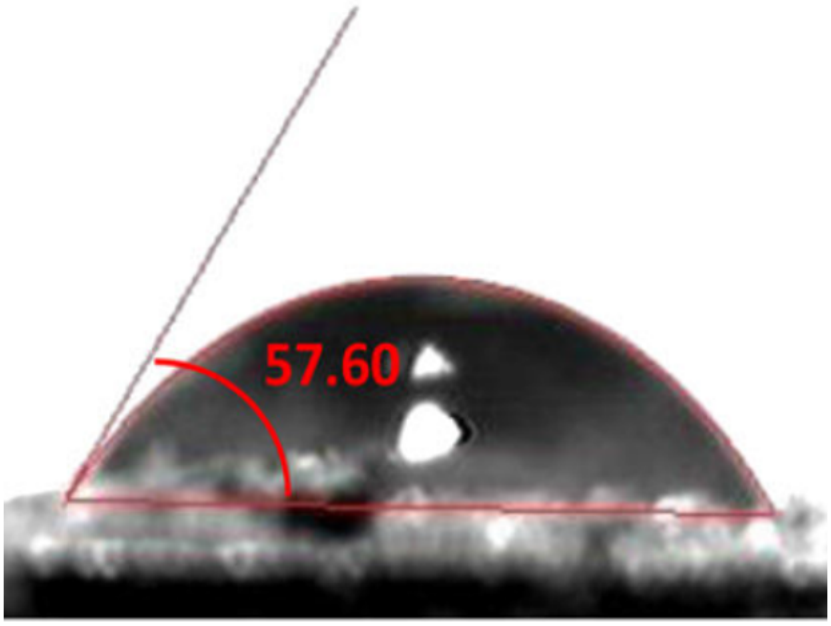

Figure 2.8: Example of a clear picture for determination of the contact angle (Morshed, Paul, and Khan, 2012).

Contact angle hysteresis measurement

If the contact angle is measured when the volume of the droplet is increasing, practically this is done just before the contact line starts to advance; the so-called "advancing contact angle" θ_a is obtained (Figure 2.9). If the volume of the drop decreases and the contact angle is determined just before the contact line starts to recede, the so-called "receding contact angle" θ_r is obtained. Usually θ_a is significantly higher than θ_r and the static contact angle θ is included between θ_r and θ_a. The difference θ_a - θ_r is the so-called contact angle hysteresis.

The KRÜSS set-up enables the change of the droplet volume at a controlled flow rate through a system of pump and syringe. To measure the contact angle hysteresis, the droplet volume is set to increase from about 10 to 14 μl and afterwards to decrease from 14 to 6 μl. The evolution of the droplet volume with time is recorded by the CCD camera. Then, the images given by the recorded video are analysed by the

KRÜSS software. The contact angle and the droplet diameter at each instant are thereby determined. A plot of these two parameters enables the determination of the dynamic angle (θ_a and θ_r) and the contact angle hysteresis.

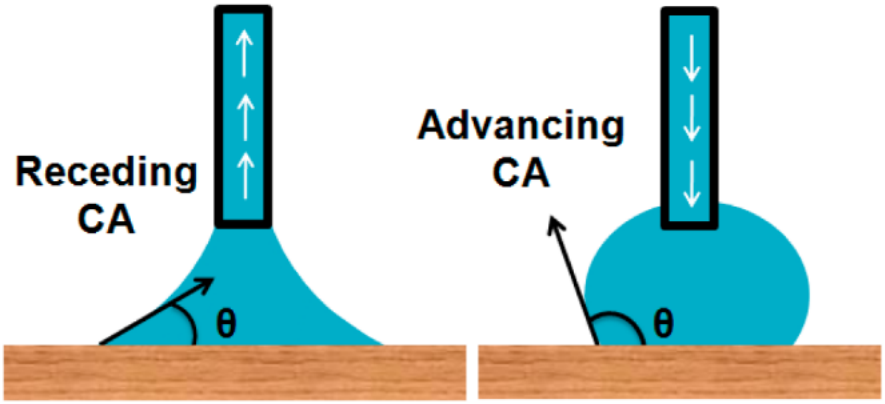

Figure 2.9: Determination of the contact angle hysteresis: a) increasing the droplet volume to obtain the advancing angle and b) decreasing the droplet volume to obtain the receding angle (Ahmad and Kan, 2016).

Some others techniques besides the sessile drop technique, have been used to determine the contact angle such as, captive air bubble method, capillary rise method and Washburn method for porous materials (Gu, 2015).

2.3.2 Atomic force microscope

The atomic force microscope (AFM) is for analysing samples surface, especially for visualinze surface image with micro- and nano- scale resolution. The first AFM was developed by Binnig, Quate and Gerber in 1986 (Binnig, Quate, and Gerber, 1986), to overcome a limitation of the scanning tunneling microscope (STM) developed by Binning and Rohrer in 1981 (Binnig and Rohrer, 1987). The STM only enables imaging materials that conducts a tunnelling current, while AFM opened the door to imaging other materials, such as polymers and biological samples.

The AFM consists of a sharp tip (probe) as shown in Figure 2.10, located at the free end of a cantilever. The tip is usually a couple of microns long and less

than 10 nm in diameter. Its tip can be modified to measure the properties such as chemical, magnetic, electrical, ferroelectric and mechanical. It can also be used for nano-fabrication. The deflection of the cantilever is measured using a laser spot reflected from the top surface of the cantilever into an array of photodiodes, providing the total contact force between the tip and the sample. When the tip is brought into a sample surface, different forces such as chemical bonding, van der Waals forces, capillary forces, electrostatic forces, mechanical contact force, etc.

For the physically or mechanically modifying surface by AFM nanofabrication, AFM tip is used to manipulate nanoclusters or nanoparticles, which are weakly absorbed by the surface, to a target surface and form nanocoatings. The procedure can be introduced in contact mode and non-contace mode. For the contact mode, nanoparticles are displaced by applying higher load. While for non-contact mode, nanoparticles are always applying lower load. Non-contact mode is to turn off the feedback system as the tip approaches the target nanoparticles while scanning. The tip could contact the particle and can further push it to a new position. AFM can also be used under force lithography or direct mechanical modification and also polarize ferroelectric materials. A rigid tip is used to modify a relatively soft sample surface. While the tip may break if the sample is too hard.

Chemecally modifying methods contains nanografting and nanopen reader and writer as shown in figure 2.12. For nanografting, it is evolved from force lithography, which is conducted on self-assembled monolayers. An AFM tip is used as a nanoshaver to rmove monolayers and expose the substrate. Nano grafting is conducted in solution, in which contains a molecule different from the self-assembled monolayers.And the molecules in the solution would be absorbed in the shaving area. Unlike nanografting, for nanopen, reader and writer, the desired molucules were coated on the tip. The AFM tip coated with desired molecules was used to displace self-assemble mono-

layers from the surface. And the molecules was absorbed on the surface to form nanostructures.

In most cases, the distance of the tip to the target is modified to maintain a constant force using feedback mechanism. Because if the tip is scanned at a constant height, it may collide with the sample surface, causing damage. Typically, the sample is mounted on a piezoelectric tube that can move the sample in the vertical direction for maintaining a constant force, and the horizontal directions for scanning the sample. The resulting map of z as a function of (x,y) represents the topography of the sample surface.

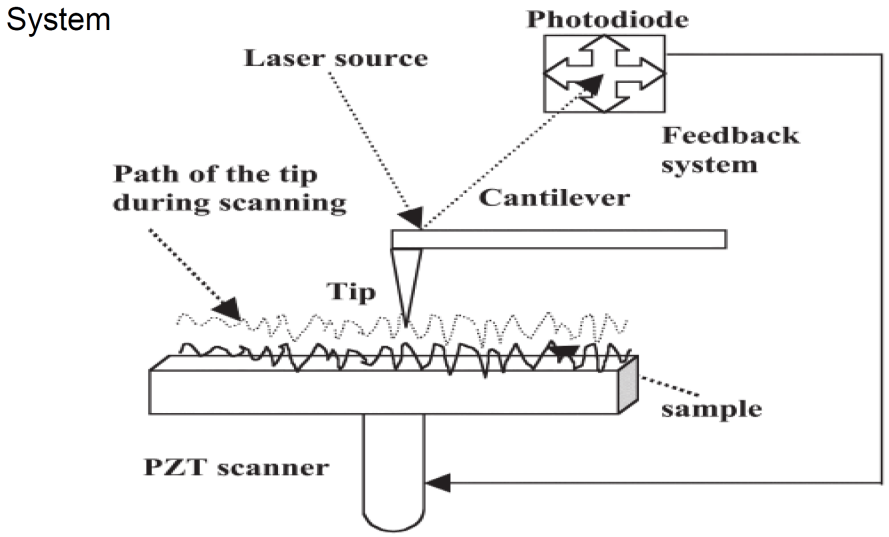

Figure 2.10: Schematic illustration for the measurement of sample topography with AFM (Tang, Shi, and Zhou, 2004).

2.3.3 Scanning electron microscope

The scanning electron microscope (SEM) is a microscope that uses a high-energy beam of electrons instead of light to form an image (Zanini et al., 2007). The electrons interact with the atoms of the sample surface, producing signals that contain information about the surface topography, composition and other properties such as electrical conductivity. The scanning electron microscopes have developed new areas

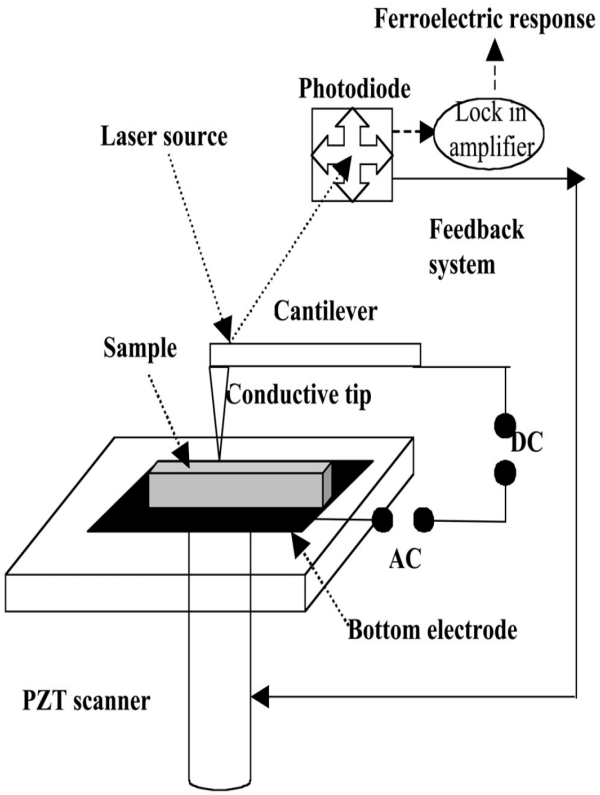

Figure 2.11: AFM nanofabrication (Béa et al., 2006).

of study in the medical and physical science communities since their development in the 1950's. Researchers can use the SEM to examine a much bigger variety of specimens since its magnifications can go to more than 300 000 X.

A beam of electrons focuses on a spot volume of the sample surface during the SEM inspection, which would lead to the energy transfer to the spot. Once the beam hits the sample, electrons and X-rays are ejected from the sample (Figure 2.13). The incident electrons, also referred to as primary electrons, dislodge electrons from the sample itself. The dislodged electrons, named "secondary electron", are attracted and collected by a detector, and then translated into a signal. To produce the SEM image, the electron beam is swept across the area being inspected, producing a lot of such signals. These signals then tend to be analyzed, amplified and translated into the topography images which need inspected. The principle components of a typical SEM are shown in Figure 2.14.

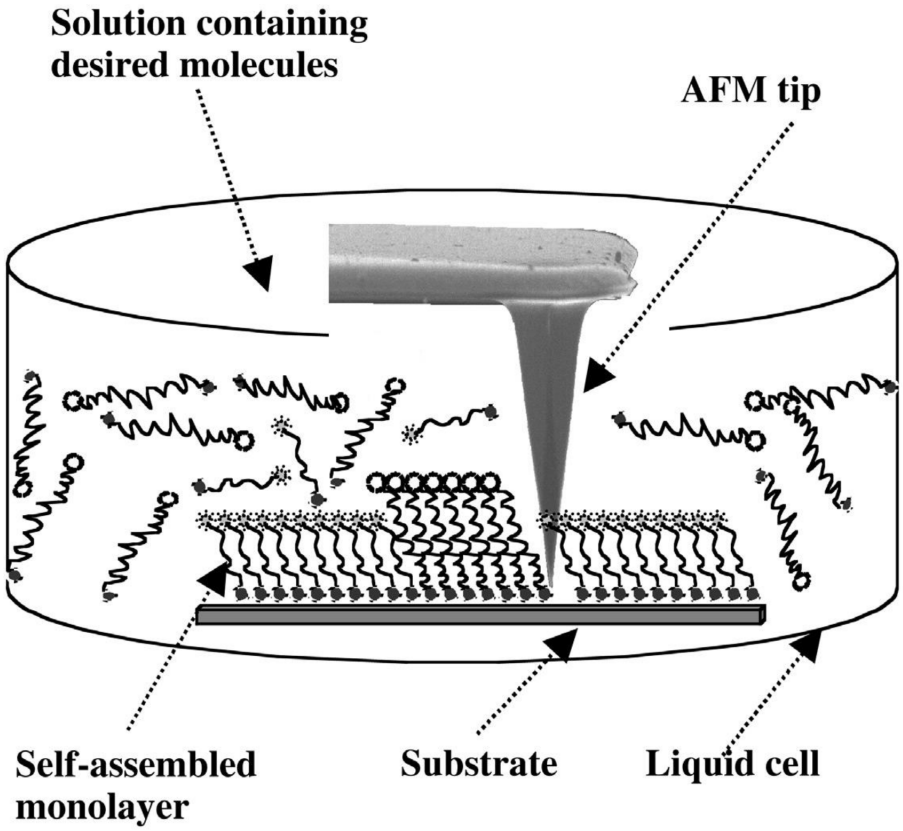

Figure 2.12: Schematic view of AFM tipbased nanografting (Tang, Shi, and Zhou, 2004).

The primary electron beam also produces the emission of backscattered or reflected electrons from the sample surface. These electrons are often used in analytical SEM along with the spectra made from the characteristic X-rays. Indeed, the intensity of signal given by the backscattered electron is strongly related to the atomic number of the sample, and thus the backscattered-electron images can provide information about the distribution of different elements in the sample.

The SEM are advantageous over the traditional microscopes. Indeed, it has a larger depth of field that allows focusing more specimens at one time. It also has much higher resolution, so closely spaced specimens can be magnified at much higher levels. Furthermore, the SEM enables more control in the degree of magnification since electromagnets rather than lenses are used. The scanning electron microscope has become one of the most useful instruments in research today.

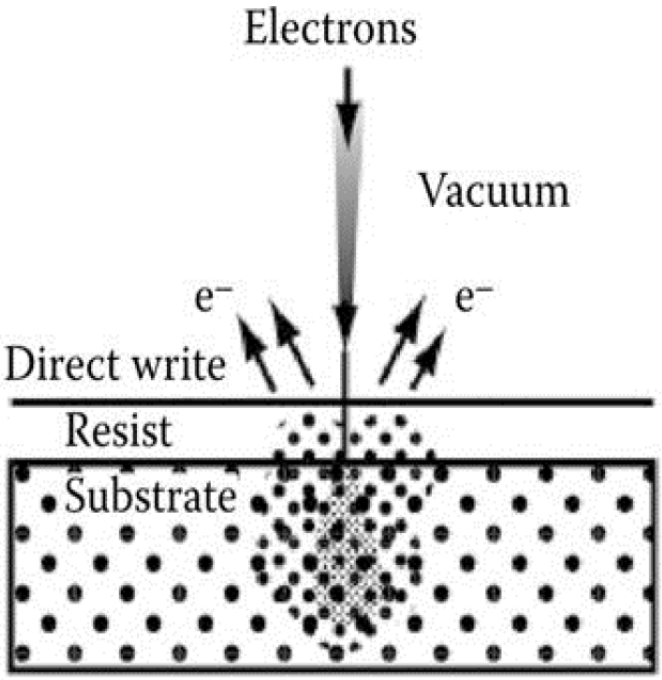

Figure 2.13: Electron-beam lithography line widths of 0.1 μm and less.

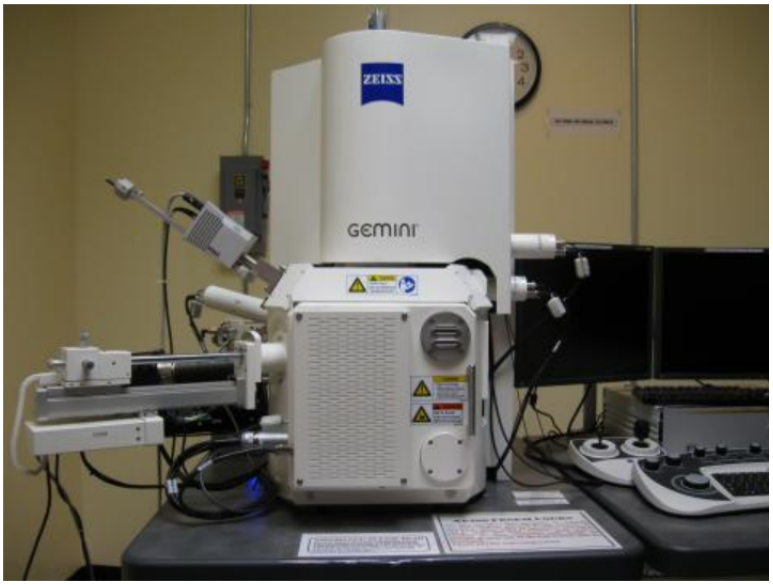

Figure 2.14: Schematic view of a typical SEM.

A field-emission cathode is used in the electron gun of the SEM to provide an electron beam that is smaller in diameter and higher in electron energy than conventional thermionic emitters such as tungsten or lanthanum hexaboride (LaB_6)-tipped filaments, which would improve the resolution and quality of images made by SEM. This microscope uses a filed-emission cathode named FEG-SEM, which has full name of "Field-emission gun scanning electron microscope". FEG-SEM produces clearer, less electro-statically distorted images with spatial resolution down to 1 nm, which is three to six times better than the conventional SEM.

Resistance and Temperature Calibration

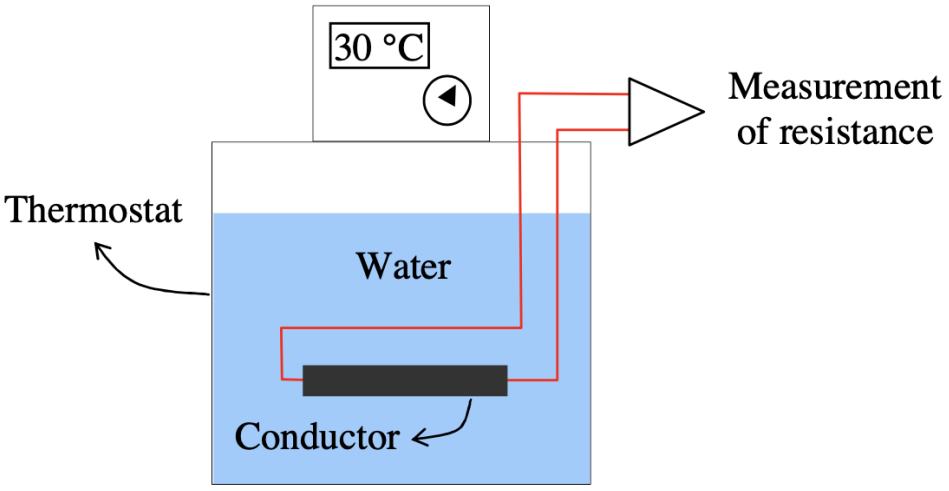

Figure 2.15: Schematic view of experimental setup for R/T calibration .

The present technique enables an accurate determination of temperature with relatively low uncertainties ($< 0.2°C$). Therefore, it was used to determine the sample temperatures for both pool and flow boiling experiments as described in the following chapters. The so-called resistance/temperature calibration is the determination of K_1 and K_0 experimentally according to the following steps. The conductor is put inside a thermostat containing deionised water (Figure 2.15). In the steady state, the temperature of the conductor is equal to the temperature of water, which is

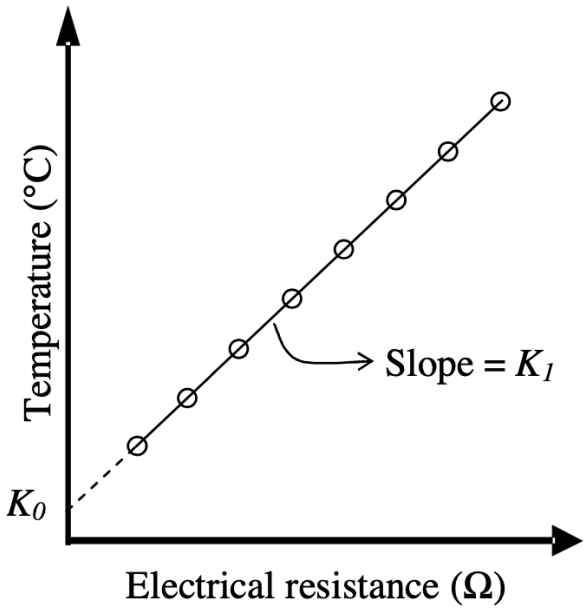

Figure 2.16: Example of T/R curve used for temperature determination from measurement of resistance (Phan, 2010).

measured by a platinum probe of $0.1°C$ accuracy. For temperature between $20°C$ and $90°C$ at the step of $10°C$, the conductor electrical resistance can be measured by using the 4-wire technique. The temperature is then plotted as a function of the electrical resistance. A linear regression of this curve will enable the determination of K_1 and K_0 (Figure 2.16). The temperature of the conductor can be determined by measurements of the resistance given these constants.

Chapter 3

Literature Review

3.1 Two-Phase Flow Instabilities

In recent few decades, the number of studies of two-phase flow heat transfer in microchannels or microgap have been growing a lot. The difficulties of flow pattern transition prediction and calculation of two-phase flow pressure drop in microchannels have been solved. However, the state-of-art of two-phase flow in microchannels is still in developing process and more fundamental experimental and analytical studies remain to be done (Thome, 2004). Several critical reviews on two-phase flow heat transfer in microchannels can be found (Thome, 2004; Kandlikar, 2002b; Huo et al., 2001; Bergles et al., 2003; Kandlikar, 2012; Han, Fedorov, and Joshi, 2016).

Two-phase flow instabilities are highly common complicated phenomena encountered in numbers of two-phase flow heat exchanger equipment. Oscillation of flow rate and system pressure were undesirable and they may cause system control issues, mechanical vibrations, and also may disturb the heat transfer characteristics so that the heat transfer surface may burn-out in some extreme situations (Kakac and Bon, 2008). There have been several reviews of instabilities in two-phase flow systems studied in recent decades (Bergles et al., 2003; Bergles, 1977; Tadrist, 2007).

Two types of widely accepted two-phase flow instabilities, which were static and dynamic instabilities, were proposed by (Boure, Bergles, and Tong, 1973). Many other researches classified more types of instabilities based on Boure's studies. The distinctions of these two types of instabilities were studied by Kakac and Bon (2008).

A flow is said to be in static instability if the new operating conditions tend to a different equilibrium point. In other words, the original operating point is not an equilibrium point. A flow is said to be in dynamic instability if there are sufficient interaction and delayed feedback between the inertia of flow and compressibility of the two-phase mixture.

Static instabilities include boiling crisis, flow excursion flow regime transition, etc. The characteristics and the mechanisms were well identified. Dynamic instabilities include thermal oscillations, pressure drop oscillations, density-wave oscillations, acoustic instabilities, parallel channel instabilities, etc. Among these instability modes, the most widely studied have been flow excursion instability and density-wave oscillations.

Many types of flow instabilities, which have been shown in macro-scale channels, were also happened in microchannels. Several studies of flow instabilities in single and parallel micro-channel flow boiling were briefly mentioned below.

Qu and Mudawar (2003) have investigated two-phase flow boiling of water in the heat sink with 21 copper parallel micro-channels (Qu and Mudawar, 2003). Two types of two-phase instability were discovered: pressure drop oscillation and parallel channel instability (Figure 3.1).

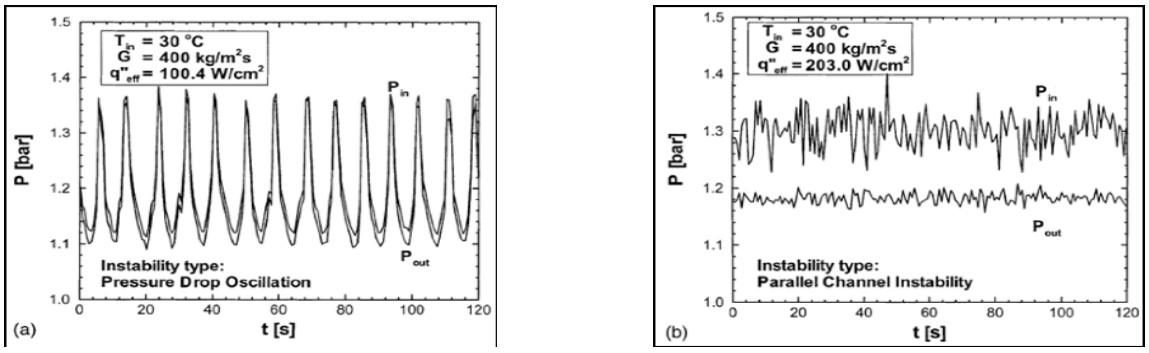

Figure 3.1: Pressure drop instability and parallel channel instability

Pressure oscillation produces periodic, large amplitude flow vibrations, which are because of interaction between vapor generated in channels and compressible volume

at the upstream of the flow in the heat sink. On the other hand, parallel channel instability produces only mild flow vibrations, which are because of wave oscillation within each channel and feedback interaction between channels. The severe flow instability can cause dry-out on the heated surface much earlier, which would lower the Critical Heat Flux (CHF). However, this kind of instability could be eliminated simply by throttling the flow upstream of the heat sink.

Kennedy et al. (2000) studied the onset of nucleate boiling and flow instability in uniformly heated microchannels with subcooled water flowing through 22 cm long tubes, with diameter of 1.17 mm and 1.45 mm, respectively. Demand curves were generated and used for the specification of the onset of nucleate boiling and flow instability points.

Brutin, Topin, and Tadrist (2003) investigated two-phase heat transfer performance and two-phase flow instabilities in a rectangular microchannel with a hydraulic diameter of 890 μm. Two-phase flow oscillation phenomena in flow boiling was evidenced. Reverse flow in the channel was captured. They found that the growing vapor slug blocked the two-phase flow and pushed the flow back to the entrance. The pressure drop fluctuations amplitudes and characteristic frequencies were also studied.

Balasubramanian and Kandlikar (2005) experimentally studied pressure drop vibrations and flow patterns in six parallel channels with a hydraulic diameter of 333 μm. In their study, reverse flow and flow maldistribution in the parallel channels were observed. Kandlikar then studied flow boiling instabilities in parallel microchannels and methods to stabilize them in the following years (Kandlikar et al., 2006).

To mitigate flow instabilities, inlet flow restrictions were often employed in either conventional channels or microchannels. The upstream throttling can effectively isolate the boiling part from compressible vapor volume. Some other methods to

reduce the flow instabilities such as diverging channel design and seeded bubbles in the channels were also investigated as reviewed in the following.

Wallis and Heasley (1961) studied the effect of inlet and outlet restrictions for conventional channel. They found that a restricted inlet with increased single-phase flow friction had a stabilizing effect. While an outlet with increased the two-phase friction could also reduce the flow instability.

Kandlikar et al. (2006) investigated two methods to stabilize the flow boiling and avoid the reverse flow in parallel microchannels experimentally. In their study, they placed pressure drop elements at the inlet of microchannels to induce a significant large flow resistance in the reverse flow direction. They also drilled artificial nucleation cavities to lower the wall superheat during the flow boiling. They found that fabricated nucleation sites with the 4% area pressure drop elements could eliminate the instabilities and the reverse flow.

Lu and Pan (2008) investigated the effects of converging and diverging channels on reducing flow boiling instabilities in parallel microchannel heat sink. Their study found that the diverging cross-section design is better than a uniform cross-section design in reducing two-phase flow instabilities.

3.2 Enhancement of Flow Boiling in Microgaps and Microchannels with Surface Treatment

Lee and Lee (2001a) and Yang and Fujita (2004) studied two-phase flow boiling in micro and minigap with gap heights ranging from 0.2 mm to 2 mm using R-133 as the working fluid. Lee developed a two-phase heat transfer coefficient correlation for the flows in micro and minigap. Their pressure drop data in the following research well agreed with the correlation obtained from water-vapor two-phase flow in the microgap (Lee and Lee, 2001b). Flow patterns such as bubbly and annular flow were observed, and gap height was found to be the factors to impact flow patterns and heat

transfer characteristics in Yang's study (Yang and Fujita, 2004). While gap height decreased, annular flow became dominant.

Sheehan, Kim, and Bar-Cohen (2009) and Sheehan and Bar-Cohen (2010) studied wall temperature during the flow boiling process using FC-72 as the working fluid in a microgap with infrared imaging techniques. Wall temperature fluctuations were ascribed to local dry-out and rewetting during film evaporation. They found that both the flow regime and input heat flux would influence the wall temperature. Kim et al. (2010) and Kim et al. (2008) studied a cooling strategy for high power light-emitting diodes (LEDs). The microgap cooling system with subcooled flow boiling of FC-72 were mounted directly on the LEDs. The maximum heat flux generated from the LEDs was measured as $20W/cm^2$. Three microgap heights from 110 μm to 500 μm were studied for both single- and two-phase flows. The heat transfer coefficient of two-phase flow was found to be higher than that of single-phase flow for all microgap heights. Generally, the two-phase heat transfer coefficient were higher as the microgap height were smaller, ranging from $10kW/m^2K$ to $7.5kW/m^2K$ for $110\mu m$ and $500\mu m$ microgap heights, respectively. They also compared two-phase heat transfer coefficient with correlations developed by Chen (1966) and Shah (1982). They found that at lower quality, it agreed with Shah's correlation, while at higher quality, it agreed with Chen's prediction.

Alam et al. (2012) studied local heat transfer and pressure drop characteristics of flow boiling of deionized water in a silicon microgap heat sink. The microgap size was 1.27 cm $\times$ 1.27 cm, and it had 5×5 heating elements and temperature sensors. Three gap heights were studied: 180 μm, 285 μm, and 381 μm, and three mass flux were studied: $420kg/m^2s$, $690kg/m^2s$, and $970kg/m^2s$. They tested the effective heat flux from 0 to $110W/cm^2$. Confined bubbly-slug flow and annular flow were observed after nucleate boiling as heat flux increased. At fixed flow rate and input heat flux, smaller gap had confined annular flow while larger gap had confined slug flow. The

main heat transfer mechanism in confined annular flow was the thin film evaporation, which resulted in higher heat transfer coefficient in smaller microgap. It also agreed with Kim's work (Kim et al., 2008; Kim et al., 2010). Surface temperatures were almost uniform along the flow direction for all the microgap heights. In smaller microgap, pressure drop increased with input heat flux increasing. But in larger microgap, pressure drop was independent from heat flux.

Alam et al. (2013) then studied the influence of surface roughness of flow boiling in microgap. The test section size stayed the same. Three gap heights of 500 μm, 300 μm, and 200 μm and three surface roughness levels of 0.6 μm, 1.0 μm, and 1.6 μm were tested in this research. In this study, they found that higher surface roughness would increased nucleation density so that increase the surface wettability and increased two-phase heat transfer coefficient. Rougher surface would also initiate boiling at lower wall superheat and increase the wall temperature uniformity. No significant difference on pressure drop was observed in microgap with the effect of surface roughness. However, increased surface roughness increased pressure instability. Higher pressure oscillation amplitude was observed during the test.

Alam et al. (2011) and Alam et al. (2013) compared the two-phase heat transfer performance differences between microgap and microchannel. Using the same test setup, they tested microgap height from 200 μm to 400 μm. They also the compared the heat transfer performance in the 200 μm high microgap with that in a microchannel with a channel pitch of 200 μm. For uniform surface heat input range from 0 to $60 W/cm^2$, and at the same mass flux of $690 kg/m^2 s$, the test section demonstrated a smaller temperature gradient and smaller amplitude of pressure oscillation in microgap than that in microchannel (Alam et al., 2011). Smaller gap heights would suppressed flow oscillation. In this study, microgap also showed better performance on temperature uniformity than microchannel. And flow boiling in smaller microgap lowered more wall temperature compared to larger microgap. Microgap showed bet-

ter heat transfer performance at relatively high heat flux due to confined slug/annular flow. While microchannel performed better at low heat flux due to early slug/annular flow (Alam et al., 2013). At low mass flux, microgap performed similarly with microchannel.

Alam et al. (2012) further studied the effects of microgap heights on two-phase flow regimes, heat transfer and pressure drop. In this study, they tested microgap heights from 80 μm to 1000 μm. They found that at lower heat flux, for the microgap heights smaller than 500 μm, confined slug flow was the dominant flow pattern. While at higher heat flux, confined annular flow was the dominant flow pattern. For microgap heights larger than 700 μm, bubbly flow was dominant at lower input heat flux and slug and annular flow was dominant at higher input heat flux, which agreed with the results in (Bar-Cohen and Rahim, 2007). Thus, they concluded that confined slug/annular flow occurred in microgap heights smaller than 500 μm, while confinement would be negligible for microgap heights larger than 700 μm. The microgap heights from 100 μm to 500 μm showed best performance in terms of keeping lower and more uniform wall temperature and also obtained high heat transfer coefficients. Smaller microgap heights could suppress pressure and wall temperature oscillation as well.

Morshed et al. (2012) compared heat transfer performance of two-phase flow boiling of DI water in microgap with bare smooth copper surface and copper surface with electro-chemically grown nanowires using DI water. They tested mass flux ranging from 45.9 kg/m^2s to 143.8 kg/m^2s, input heat flux from 0 to 60 W/cm2 and inlet flow temperature ranging from 22 $^\circ C$ to 80 $^\circ C$. In their analysis, the copper surface with nanowires could reduce the wall superheat by up to 12 $^\circ C$. The results also showed that the copper surface with nanowires improved single-phase heat transfer coefficient by up to 25%. The flow boiling in microgap on copper with nanowires

improved two-phase heat transfer coefficient by up to 56% with the pressure drop increase of 20%.

Morshed, Paul, and Khan (2012) further studied the difference between the micro-gap with smooth bare copper surface with four 0.5 mm × 0.5 mm square cross-grooves and smooth copper surface with four nanoparticle deposited cross-grooves. The copper surface with grooves increased critical heat flux (CHF) by up to 15%, and also increased both single- and two-phase heat transfer coefficient by up to 50%. The surface with grooves also lowered the initiated boiling temperature. The nanoparticles deposited grooves might further lower initiated boiling temperature. However, there was no evidence of heat transfer coefficient improvement in their study.

Kosar and Peles studied flow boiling of R-123 from staggered circular micro pin-fin array (Koşar and Peles, 2006) and staggered hydrofoil-shaped micro pin-fin array (Koşar and Peles, 2007) in the microchannel sizing of 10 mm length, 1.8 mm width, and 243 μm height. This configuration introduced the use of micro pin-fin surface enhancement features. The microchannel contained 20 × 12 staggered hydrofoil pin-fins with wetted perimeter of 1030 μm. The diameter of these circular pins is 99.5 μm. The contact angle of R-123a on silicon is near zero, which would result in deactivation of large nucleation sites and high superheat of initiated boiling. They found that, at some conditions, a slight increase of input heat flux would cause a sudden increase in flow boiling, temperature and pressure oscillations. They tested mass flux ranging from 976 kg/m^2s to 2349 kg/m^2s and heat flux ranging from $19W/cm^2$ to $312W/cm^2$. In their study, they found that the heat transfer coefficient would increase with the increasing input heat flux, and stopped increasing when a maximum value was reached. Then the HTC would decrease monotonically with the continued increasing heat flux until reaching CHF.

Krishnamurthy and Peles (2008) investigated flow boiling of water in 1.8 mm wide, 10 mm long, and 250 μm height channel with staggered circular pin-fins in the

diameter of 100 μm and pitch-to-diameter ratio of 1.5. They tested heat flux ranging from $20 W/cm^2$ to $350 W/cm^2$ and mass flux ranging from $346 kg/m^2 s$ to $794 kg/m^2 s$. In this study, they maintained the outlet of the test section at atmospheric pressure. They found that two-phase heat transfer coefficient was somehow dependent on mass flux, but was independent of heat flux, mass flux the range they tested. A correlation was developed to predict heat transfer coefficient using models based on Reynolds analogy. They defined the liquid Reynolds numbers using superficial velocities. A flow pattern map was also developed using gas/ liquid Reynolds numbers and agreed well with the flow map for adiabatic microscale systems developed using DI water.

Lie et al. (2007) studied heat transfer coefficient and bubble characteristic of flow boiling of FC-72 in the microgap with square pin-fins. The pins had a length of 200 μm and height of 70 μm, and both transverse and longitudinal pitches were the same as pin side length. The flow pattern was observed as mostly bubbly flow. Two-phase heat transfer coefficient was found to be independent of mass flux, but it would increase with more input heat flux. The micro pin-fins largely improved bubble departure frequency and two-phase heat transfer coefficient. Bubble active nucleation site density and departure diameter decreased with the increasing mass flux, while bubble departure frequency increased with increasing mass flux. The departing bubbles were also much larger when the input heat flux was larger.

Qu and Abel studied flow boiling heat transfer of water in the microgap with staggered square micro pin-fins (Qu and Siu-Ho, 2009). The microchannel size was 3.38 cm length by 1 cm width. The cross section of a single pin was 200 μm $\times$ 200 μm, and the height was 670 μm. They tested water inlet temperatures of 30 $^\circ C$, 60 $^\circ C$, and 90 $^\circ C$, and mass fluxes ranging from 183 $kg/m^2 s$ to 420 $kg/m^2 s$ for each inlet temperature. The input heat flux was tested from 23.7 W/cm^2 to 248.5 W/cm^2 and outlet pressure varied from 103 kPa to 108 kPa. They observed that at lower quality, two-phase heat transfer coefficient decreased with increasing heat flux.

While the two-phase heat transfer coefficient was fairly constant at quality greater than 0.15, and it was also independent from the mass flux. The mean absolute error of their results was more than 630% compared with the correlation developed by Krishnamurthy and Peles (2008) mentioned previously.

Ma et al. (2009) and Yuan et al. (2009) studied the subcooled flow boiling of FC-72 on the silicon chip with micro pin-fin. The size of micro pin-fin in their studies was less than 100 μm, which was much smaller than channel size whose width was 30 mm and height was 5 mm. Surface with micro pin-fin significant improved heat transfer performance compared to smooth surface in heat transfer coefficient and CHF.

With a similar test setup, Guo, Wei, and Zhang (2011) investigated subcooled flow boiling in the silicon chip micro channel with pin-fin and jet impingement to achieve enhanced heat transfer performance and delayed CHF using FC-72 as the working fluid. As jet velocity increased, the mixing and turbulence in stagnation area would improve so that enhanced heat transfer significantly.

Isaacs et al. (2012) and Isaacs et al. (2013) studied flow boiling in the staggered circular pin-fin in the microgap using R-245fa as the working fluid. The area was 1 cm $\times$ 1 cm and the circular pin's diameter, height, and pitch are 150 μm, 200 μm and 225 μm, respectively. The mass flux they tested was ranging from 598 W/cm^2 to 1639 W/cm^2, and they tested heat flux up to 40 W/cm^2. The inlet liquid was subcooling of 10 $^\circ C$ and 13 $^\circ C$. They did the visualization in this study, and triangular-shaped vapor were observed after nucleation.

A flow separation technique was proposed and studied by Dai et al. (2013). They studied the flow boiling of DI water in the copper microgap of 5 mm (W) $\times$ 26 mm (L) $\times$ 0.34 mm (H). A two-layer copper woven mesh with the thickness of 160 μm was coated on tested copper surface. A part of incoming fluid was separately routed to an opening microjet of diameter 0.8 mm located in the center of the cover of the microgap and entered microgap from the opening microjet as shown in Figure

3.2. The fraction of liquid going through the center opening microjet was totally determined by pressure balance between microgap inlet and the opening microjet during fluid flow through the microgap, so this kind of technique was called passive flow separation. This flow separation technique was found to enhance mixing of the flow and greatly reduce temperature gradient in single-phase flow, as well as to suppress bubble growth and flow instabilities in two-phase flow to delay the surface dry-out process.

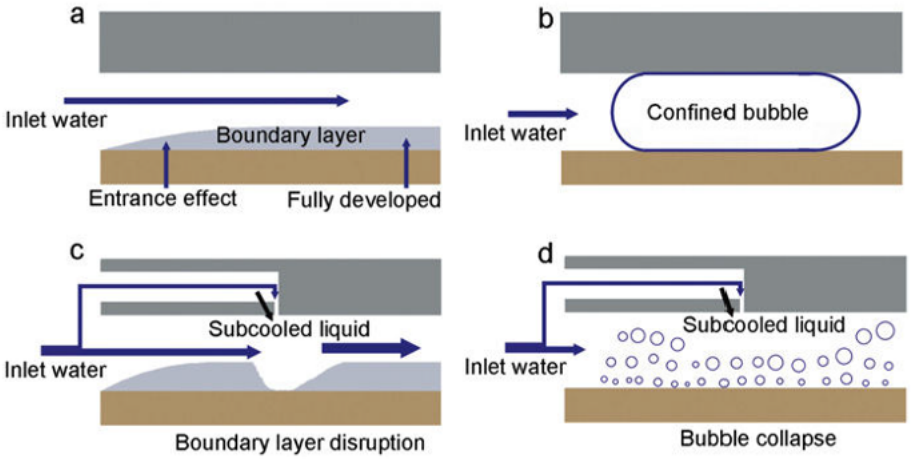

Figure 3.2: Concept of the passive flow separation technique by Dai et al.

Reeser, Bar-Cohen, and Hetsroni (2014) studied heat transfer and pressure drop performance of DI water and HFE-7200 in staggered arrays of micro pin-fins. The arrays had a 0.96 cm $\times$ 2.88 cm area and square pin-fin 153 μm length and 305 μm height. For DI water, the mass flux ranged from $400 kg/m^2 s$ to $1300 kg/m^2 s$ and HFE-7200 ranged from $200 kg/m^2 s$ to $600 kg/m^2 s$. The heat flux ranged from $10 W/cm^2$ to $110 W/cm^2$ and $0 W/cm^2$ to $36 W/cm^2$, respectively. High exit quality up to 0.9 for HFE-7200 was achieved in their study. Heat transfer coefficients were significantly different between DI water and HFE-7200 due to different properties of the working fluid. They also found that heat transfer coefficient correlation developed by Krishnamurthy and Peles (2008) and pressure drop correlation developed by Qu

and Siu-Ho (2009) were not accurate in prediction of their work and needed to be modified.

Ong et al. (2014) studied flow boiling of R1234ze in a radial hierarchical fluid network. The concept was to introduce fluid inlet at the center of test device, and fluid was then directed radially to outlets located on the edge of test device. They utilized different sizes of orifices at inlet to distribute fluid flow to subsection of the test devices. The radial quadrant microgap with circular pin-fin mitigated the pressure gradients and reduced temperature gradient as well. They also studied microgap with staggered pin-fin (27 deg and 45 deg), but the results were not compared with radial quadrant test device. The observed two-phase flow instabilities and believed two-phase flow instabilities were related to the degree of inlet subcooling.

Schultz and coworkers also tested a radial microgap with embedded pin arrays using the same fluid (Yang et al., 2015; Schultz et al., 2015). The test device size was 20.25 mm $\times$ 20.25 mm and had eight core heaters and 16 hotspot heaters, and they studied the effects of local hotspot. They have found that there are 50% increase in mass flow rate, which only led to 8% in two-phase heat transfer coefficients. The rise in mass flow rate did not necessarily mitigate temperature nonuniformity.

Using R-134a in an open-loop, David et al. studied effects of transient heat load on two-phase heat transfer coefficients in a microgap with staggered square pin fins (David et al., 2014). Their results indicated that temperature was maintained near uniform under both steady state and transient heating. Higher heat transfer coefficient was achieved under transient heating than steady-state heating. Heat transfer coefficient varied with vapor quality, and a peak was observed for vapor quality of 0.55.

Tamanna et al. investigated the effect of expanding the microgap height on flow boiling heat transfer and pressure drop characteristics (Tamanna and Lee, 2014; Tamanna and Lee, 2015). The microgap was formed with silicon base and poly-

carbonate cover with the inlet height of 200 μm for all the gaps, and the outlet height increases from 200 μm to 300 μm and to 460 μm. A delay of partial dryout was observed in the 200–460 μm microgap at a heat flux of $79 W/cm^2$, compared to the straight 200–200 μm microgap at a heat flux of 61 W/cm^2. The expanding microgap with outlet height of 300 μm gives the smallest pressure drop, by providing room for the vapor expansion without excessive flow acceleration, and best wall temperature uniformity of all the three tested heights. Further expansion of outlet height 460 μm increased pressure drop due to unstable boiling and vapor acceleration. The fluctuations in temperature caused by unstable boiling in microgap were found to be independent of fluid quality and heat fluxes (Sheehan and Bar-Cohen, 2010).

Woodcock et al. developed a piranha pin fin (PPF) structure in a microgap (Woodcock et al., 2015). They investigated flow boiling of HFE-7000 in PPF-enhanced microchannel and achieved heat flux as high as $700 W/cm^2$. Tested mass fluxes ranged from 1200 kg/m^2 s to $7000 kg/m^2 s$. A staggered array PPF, each of diameter 150 μm and with a 300 μm long tail, was used. The PPFs had open mouths on leading edges, with PPFs wall thickness of 30 μm, and fluid flow could come inside the PPFs and be extracted from the bottom fluid passage of each PPF. This way heat transfer was significantly enhanced in single-phase and two-phase conditions.

In summary, the review on flow boiling in plain microgap and microgap with pin fin surface enhancement revealed the ability of this promising strategy as thermal management method for high heat flux removal. However, further research work is still needed to understand the physics of boiling in microgap and especially in microgap with pin fin surface enhancement. The dependences of boiling mode, two-phase heat transfer coefficient and pressure drop on inlet temperature, heat flux, and mass flux are still unclear and require further study.

Chapter 4

Enhanced Single and Two-phase Heat Transfer of Microgap Heat Sink with Nano-Structure coatings (Black CuO)

4.1 Test Loop

An open test loop was designed for the present experiment, as shown in Figure 4.1. Deionized (DI) water was degassed in a 10 gallon stainless steel water tank at saturation temperature of 46 $^{\circ}C$. The DI water was heated to 75 $^{\circ}C$ by a flexible silicone-rubber heat sheet for about 12 hrs. The air was removed by the vacuum system. The degassed DI water was cooled down to room temperature before the tests. The degassed DI water was pumped from the stainless steel water tank to the test section by a gear pump (ISMATEC _ Regol-z digital) at a constant flow rate. A flow meter (FLR-1619A-B) was used to assure the accuracy of flow rates. The pump and the flow meter was calibrated using a measuring cylinder and stopwatch method prior to tests. Two pressure transducers (OMEGADYNE, INC. PX329-100A10V, 0-100 PSI) were used to measure the pressure drop between the inlet and outlet plenums. The water from the test section outlet was collected by another water tank. The temperature and pressure data were recorded by an Agilent 34972A data acquisition system.

The test sample assembly was consist of a transparent cover plate, a heat insulation housing block, a copper heat sink (26 mm $\times$ 5.5 mm) with a copper heating

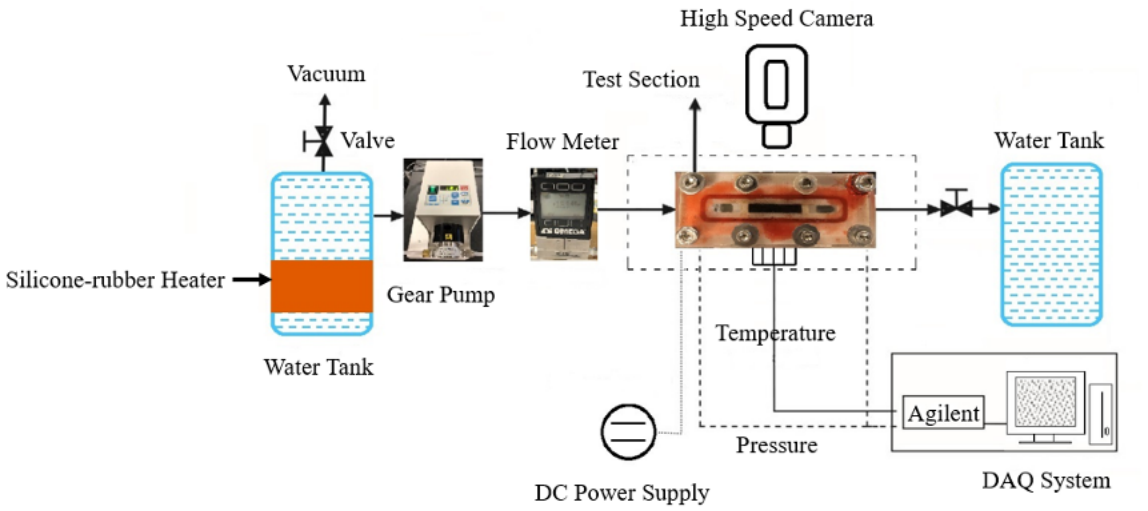

Figure 4.1: Test loop for heat transfer in a micro-gap or channel

block, four cartridge heaters and insulation materials. Major dimensions were specified in Table 4.1. The cover plate was made of high-temperature polycarbonate plastic (Lexan) with 90% transparency and the heat insulation housing was made of G-7 fiberglass. The copper heat sink with heating block were fabricated from oxygen-free high thermal conductivity copper (101 copper, McMaster-Carr). Four 120 V, 500 W cartridge heaters provided input heat flux by a direct current (DC) power supply (BK precision, Programmable PFC D.C. Supply 120 V/10 A, VSP 12010).

The whole test section parts were settled in an aluminum housing and insulated by Nelson Firestop Ceramic Fibers. Black CuO was coating on the copper heat sink served as an enhanced flow boiling heat transfer surface. High-temperature silicone sealant (RTV-106, Momentive) was used as thermal insulations and sealing parts. Eight holes were drilled in two rows to mount thermocouples as shown in Figure 4.2. Five holes were drilled in the upper row with a distance to the surface of 3 mm. Three holes were drilled in the lower row directly below the middle three holes of the upper row. The distance between the two rows is 4.5 mm. The thermocouples were anchored by high thermal conductivity thermal paste for good contact condition and high-temperature silicone sealant.

Table 4.1: Dimensions of the Configurations

Samples	**Parameters**		
Microgap	Height: 0.25 mm	Length: 26 mm	Width: 5.5 mm
Copper Block	-	Length: 26 mm	Width: 5.5 mm
Inlet Restrictor	Height: 0.05 mm	Length: 2 mm	Width: 5.5 mm
Thermocouple Holes	Diameter: 0.85 mm	Depth: 2.5 mm	-

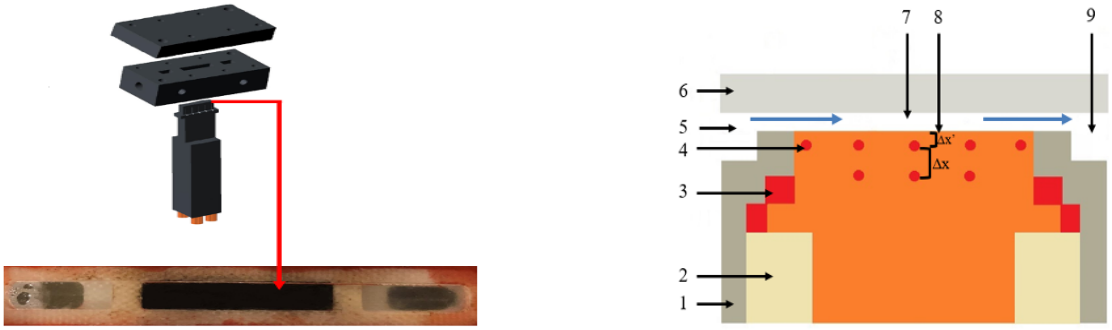

Figure 4.2: 1. G7 Fiberglass housing. 2. Nelson Firestop Ceramic Fibers. 3. High temperature RTV 106 paste. 4. Two-row thermocouples, where, Δx= 4.5 mm and $\Delta x^{'}$= 3 mm. 5. Inlet plenum. 6. Lexan Cover. 7. Flow and microgap. 8. Black CuO coating. 9. Outlet water.

4.2 Fabrication and Characterization of the Test Samples

The copper test surface was cleaned in an ultrasonic bath sequentially with distilled water and ethanol to get rid of the dusts and oil on the surface. Then it was dipped into 10.0% sulfuric acid solution to get rid of the oxidations for 5 minutes. Continually dipped the copper surface into acetone, ethanol, isopropyl alcohol and distilled water for 10 minutes, respectively. And at last it was rinsed with DI water and dried with a mild nitrogen gas flow. A typical wet chemical fabrication method was used to prepare nano-structured CuO coatings on copper substrates. A strong oxidizing alkaline solution was prepared with NaClO2 (3.75 g), NaOH (5 g), Na3PO4 · 12H2O (10 g) per 100ml distilled water (Miljkovic et al., 2013; Wang et al., 2017). The chemical reaction occurs at 95 $^{\circ}C$ for 120 minutes.

For the first 30 minute, the copper was initially oxidized to form a thin oxidation layer, which has a brown color. And future oxidized reacted continually on the

brown layer to form CuO nanostructures, which is black. (Figure 4.3(a)) (Drogowska, Brossard, and Ménard, 1988). As observed by Scanning Electron Microscope (SEM, Zeiss Ultra Plus FESEM), the morphology of sample shows Cu2O are with a thickness of approximately 300 nm, and black CuO has a thickness of about 1 μm, as shown in Figure 4.3(b). Thus, the total thickness of the nano-structured coatings is approximately 1.5 μm. The formation of the coatings is confirmed from X-ray diffraction analysis (XRD). The peaks of CuO can be identified from XRD patterns as shown in Figure 4.3(c), However, no peaks of Cu2O is identified, which may because of the long reaction time in this study.

The nano-structures have blade-like morphology. The blade-like tip converges to a sharp point with a thickness of less than 10 nm and average widths of approximately 300 nm. The surface roughness was measured as Ra = 373 nm by Atomice force microscope (AFM). The contact angle of water on the black CuO nano-structures was tested to be approximately 5 $°C$. Thus, the black CuO coated surface can be determined as a superhydrophilic surface. The microcavity size was found to less than 1 micron, and it has a high nucleation site density. High nucleation density causes high supersaturations, which can significantly enhance the wettability and capillary force.

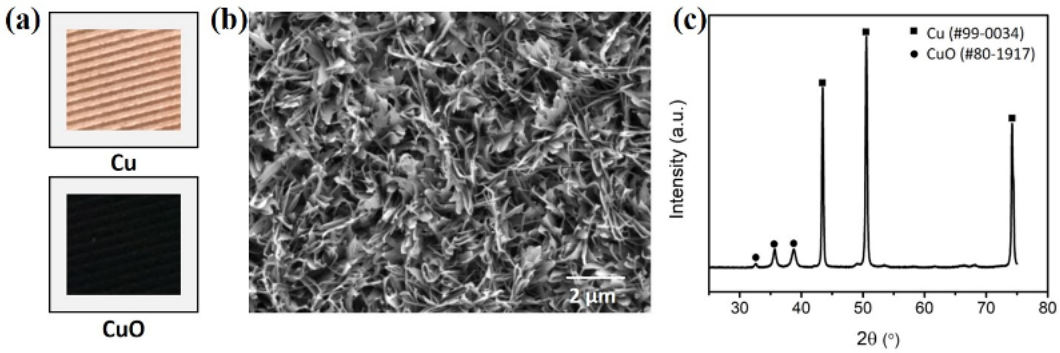

Figure 4.3: Surface morphology and components of surface coatings. (a) Image of surface before and after oxidization. (b) SEM image and (c) XRD patterns of prepared CuO nanosctrucutres.

4.3 Advantages of Fabrications

Due to the good chemical reaction response of copper, surface polishing was not necessary. The wet chemical reacting process can easily be applied to any arbitrarily shaped surfaces, while other surface treating process cannot or be hard to applied to other shaped or over large area surfaces. Furthermore, the chemical reacting temperature in this study maintain around 95 $^{\circ}C$, which is a relatively low reacting temperature compared with other surface treatment methods. And high temperature annealing or drying processes are not required during the whole reacting process.

The particular blade-like morphology of the black CuO nanostructures, with a tip dimension of about 10 nm, ensures high nucleation site density within the structure due to the increased energy barrier for typical flow boiling conditions studied here. Furthermore, due to the unique blade-like morphology of the nanostructures, the oxide growth mechanism is self-limiting. It can create a uniform and thin nanostructure layer independent of oxidation time. And the self-limiting mechanism of the oxidation process is critical to minimizing the coating layer height which can directly minimizing the thermal resistance of the two oxide layers, even though the bulk thermal conductivities of the two copper oxidations (kCuO $\approx$ 20 W/m.K, kCu2O $\approx$ 30 W/m.K (Boure, Bergles, and Tong, 1973)) are an order smaller than the pure copper substrate (kCuO $\approx$ 401 W/m.K).

4.4 Data Reduction

Total input heat flux can be obtained according to the Fourier's Law from two rows of thermocouples shown in Figure 4.2 by the following equations,

$$q'' = k\frac{\Delta T}{\Delta x} \tag{4.1}$$

$$\Delta T = \frac{T_6 + T_7 + T_8}{3} - \frac{T_2 + T_3 + T_4}{3} \tag{4.2}$$

where q'' is the total input heat flux, k is the thermal conductivity of copper, and Δx is the distance between the two rows of thermocouples which is 4.5 mm in this study, as shown in Figure 4.2. T_1 to T_8 are the temperature measured by thermocouples at the location shown in Figure 4.2 (b). The surface temperature along the flow direction above $1 \sim 5$, $T_{i,s}$ was calculated by

$$T_{i,s} = T_i - q'' \frac{\Delta x'}{k} (i = 1 \sim 5). \tag{4.3}$$

The average surface temperature can be known by

$$T_s = \frac{1}{5} \sum_{1}^{5} T_{i,s} \tag{4.4}$$

where T_i is the corresponding thermocouple reading, and $\Delta x'$ is the distance between the first thermocouple row and the top surface which is 3 mm in this study, as shown in Figure 4.2. The single- and two-phase heat transfer coefficient can be obtained as,

$$T_m = (T_{in} + T_{out})/2, \tag{4.5}$$

$$h_{sp} = q_{eff}/(T_s - T_m), \tag{4.6}$$

$$h_{tp} = q_{eff}/(T_s - T_m) \tag{4.7}$$

where T_m is the average water temperature though the microgap. The pressure can be measured at inlet and outlet plenums by pressure transducers, and pressure losses happened at the inlet contraction and outlet expansion. Thus, the pressure drop through the microgap can be calculated as

$$\Delta p = (p_1 - p_2) - (\Delta p_{c1} + \Delta p_{c2}) - (\Delta p_{e1} + \Delta p_{e2}) \tag{4.8}$$

where p_1 and p_2 are inlet and outlet pressure measured by pressure transducers. Δp_{c1} is the contraction pressure losses from the deep plenum to the shallow plenum and Δp_{c1} is the contraction pressure losses from the shallow plenum to the microgap; Δp_{e1} is the expansion pressure losses from the shallow plenum to the deep plenum and Δp_{e1} is the expansion pressure losses from the microgap to the shallow plenum, respectively.

Total heat loss of the system was calculated in the condition that no water was flowing through the smooth copper surface microgap. At a given constant heat input, the temperature at two row position was collected by the DAQ system. The effective heat flux of zero mass flux can be calculated using equation (4.6). This calculated heat flux was the heat loss of the whole test section. Heat loss could be found at all surface temperature gradient. A correlation of heat loss and surface temperature was generated for further data reduction for this test set-up in this study.

4.5 Uncertainty Anlysis

Uncertainties in instruments and measurements were estimated as: mass flux, ± 1.8 $kg/(m^2s)$, local temperature, $\pm 0.5°C$ and pressure, ±0.25%. Error propagation in the value was calculated using the Kline and McClintock method. The uncertainty of the heat flux q'' was ±6%.

4.6 Visualization Study

Figure 4.4 shows our visualization study for two-phase flow pattern of both bare surface and Black CuO coated surface at the same mass flux G = 151 $kg/(m^2s)$ and surface temperature = 104 $°C$. For the onsite boiling on both walls, nucleation boiling starts in downstream region of the microgap. However, boiling on black CuO coated wall at a lower heat flux was much effective.

Two-phase flow patterns associated with increasing heat flux were very different for the bare copper surface and the black CuO coated surface. For bare copper surface, there was a quick transition from bubbly flow to bubbly-slug flow and then annular flow.eventually reaching dryout condition at critical heat flux (CHF). In the Figure 4.4 (b), at the onset boiling in the microgap, lots of small bubbles formed on the smooth copper surface, grew and coalesced together. When the bubbles were big enough, they started to depart from the surface and flushed to the downstream to the outlet of the microgap. At the bubble growth process, subcooled flow condensed the bubbles induced the temperature increasing on the surface.

In the Figure 4.4 (a), two-layer flow was observed. The lower layer flow was observed to be faster than the bulk flow. The lower layer flow could be driven by both pump and also the strong capillary force. Thin film boiling was more effective to prevent bubble slug in the channel. The rewetting process is faster than that of bare copper surfaces. No large amount and large size bubbles were observed during the boiling process in the black CuO coated surface microgap. Because of the near-zero-contact angle microcavity and large nucleation site density, bubbles formed on the thin film flow and departed at a super small size, as shown in Figure 4.5. No bubble coalescence was observed in the microgap. Then the liquid layer dissipated to the edges of the channel. That could mainly cause the more uniform temperature distribution and reduced the surface temperature compared with that of bare surface. It can also effectively remove a lot of heat load from the hot surface. More results would be discussed in next part of this paper.

4.7 Results and Discussions

Heat loss of the whole test section was measured and calculated using the two-row thermocouple measurement method as mentioned in the previous part. The relation between total heat loss and the surface temperature was as shown in Figure 4.6.

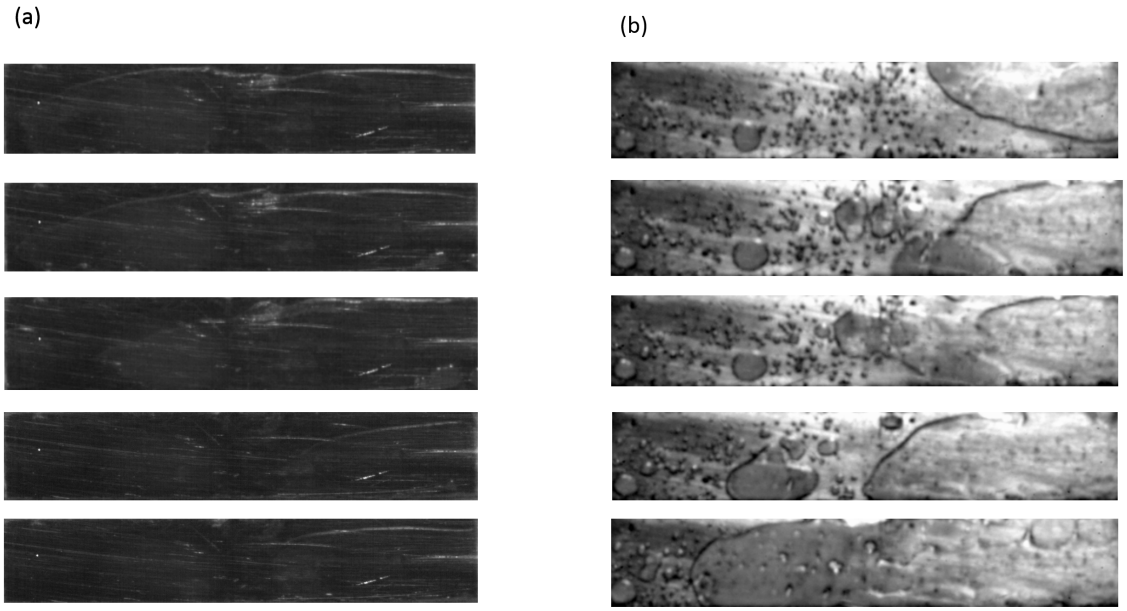

Figure 4.4: Flow pattern at G = 151 $kg/(m^2s)$ and surface temperature = 104 $^\circ C$. (a) Black CuO Coated Surface (b) Smooth surface.

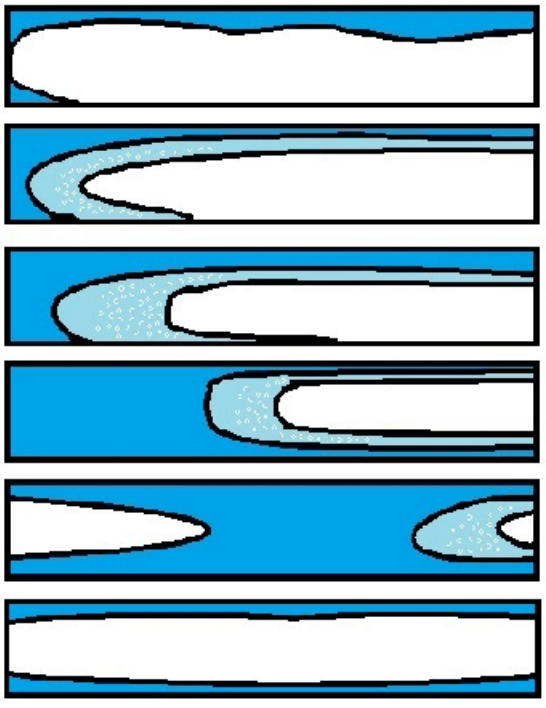

Figure 4.5: Sketch View of Two-layer Flow.

Comparing with the total heat flux input, the heat loss was relatively small and could be almost negligible. The small heat loss contributed to the two-row thermocouple design.

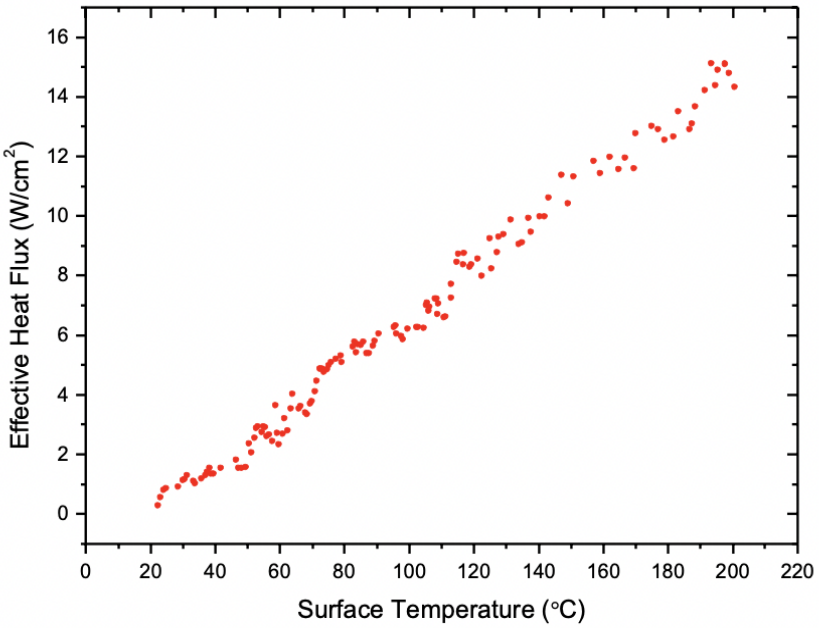

Figure 4.6: Heat Loss of the Test Set-up.

In this study, Two sets of experiments were conducted to examine the effects of black CuO coated surfaces and smooth plate surface on flow boiling. The black CuO coated surface has much higher active nucleation site densities, larger heat transfer area and additional capillarity compared with smooth plate surface. CHFs and HTCs will be obtained on the black CuO coated surface. In addition, the surface temperature will be analyzed to see how it works on nucleate boiling and capillary evaporation.

4.7.1 Decreased Surface Temperature

As shown in Figure 4.7, the results revealed that the surface temperatures were reduced by 23.1 $\pm 0.6°C$ and 31.3 $\pm 0.6°C$ at the heat flux of 23.0 and 60.0 W/cm^2, respectively, in the two-phase regime at the mass flux of 373.7 $kg/(m^2s)$. At the CHF condition, the black CuO coated surface can withstand higher surface temperature compare with that of bare Cu surface. Larger heat transfer areas on black CuO nano-structured surface is considered to be the main reason of the decreasing of the surface temperature for single-phase flow. As shown in Figure 4.8, the surface temperatures were reduced by up to 7 $°C$ and 12 $°C$ in the single-phase regime at a heat flux of 12.7 W/cm^2 and 27.5 W/cm^2, respectively, at the mass flux of 373.7 $kg/(m^2s)$.

The enhancement for two-phase convective heat transfer should be a result of surface temperature decreasing and a more uniform distributed surface temperature on the heating surface. Higher heat transfer areas and higher supersaturations prior to surface flooding causes the decreasing of the surface temperature as shown in Figure 4.9. This is due to the fast rewetting process and the liquid thin film boiling causing the lower surface temperature on the downstream of the microgap. Moreover, temperature jump on the bare copper surface microgap could be a result of insufficient liquid flow supply in the downstream section. While for the flow in black CuO coated surface microgap, no temperature jump was found in the downstream section. At a higher superheat, two-phase convective heat transfer is dominant and the surface temperature goes down at the point near the outlet. This is due to the liquid film becomes thinner at the downstream section. The thinner liquid film boiling can be more effective to release heat from the surface at the downstream. The uniformity of the temperature of the black CuO surface is further discussed in the following subsection.

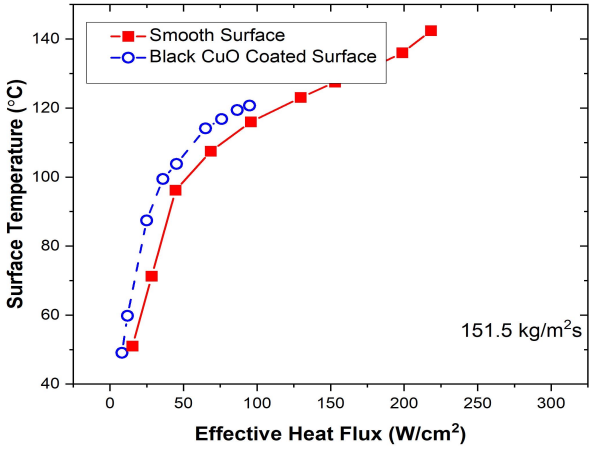

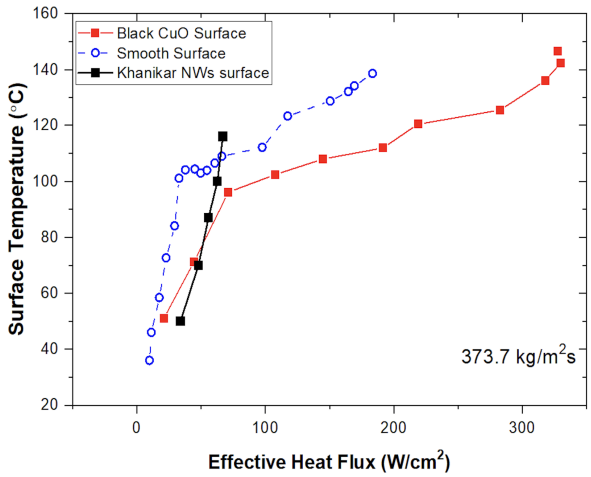

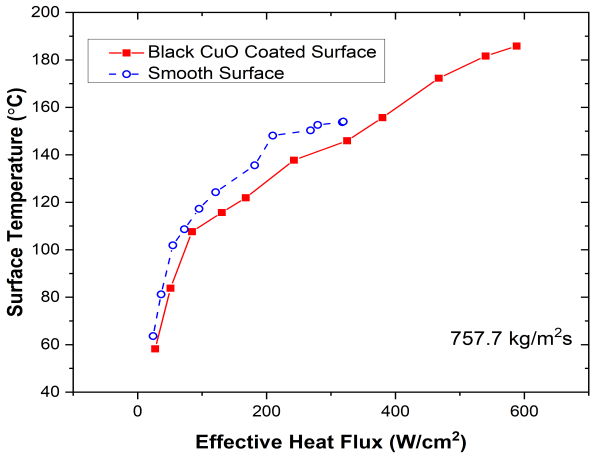

Figure 4.7: Surface Temperature in a microgap with Black CuO coating.

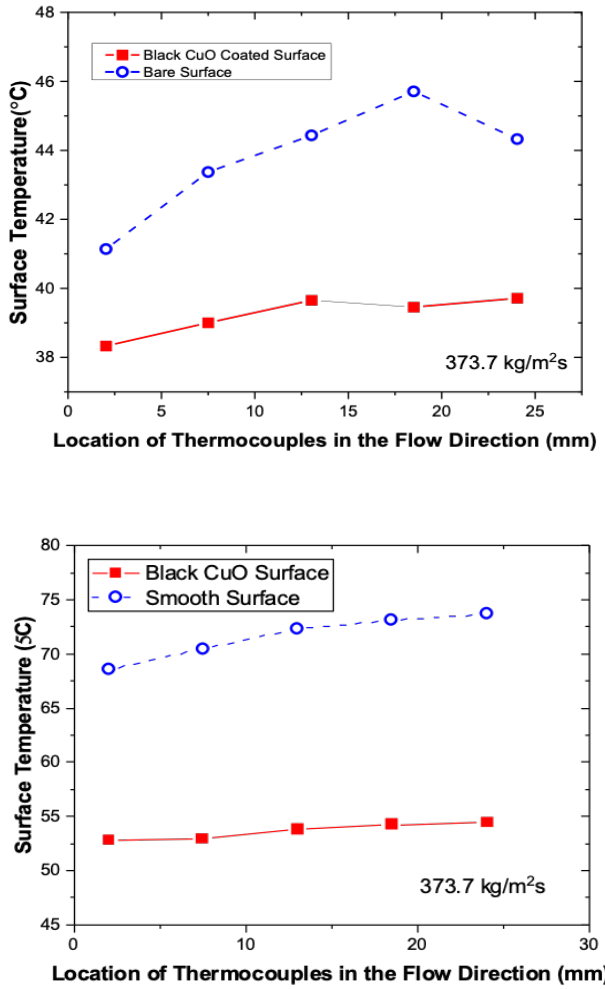

Figure 4.8: Temperature distribution on the heating wall in a microgap along the flow direction. (a) Surface temperature distribution in single-phase heat transfer at a heat flux of 12.7 W/cm^2. (b) Surface temperature distribution in single-phase heat transfer at a heat flux of 27.5 W/cm^2.

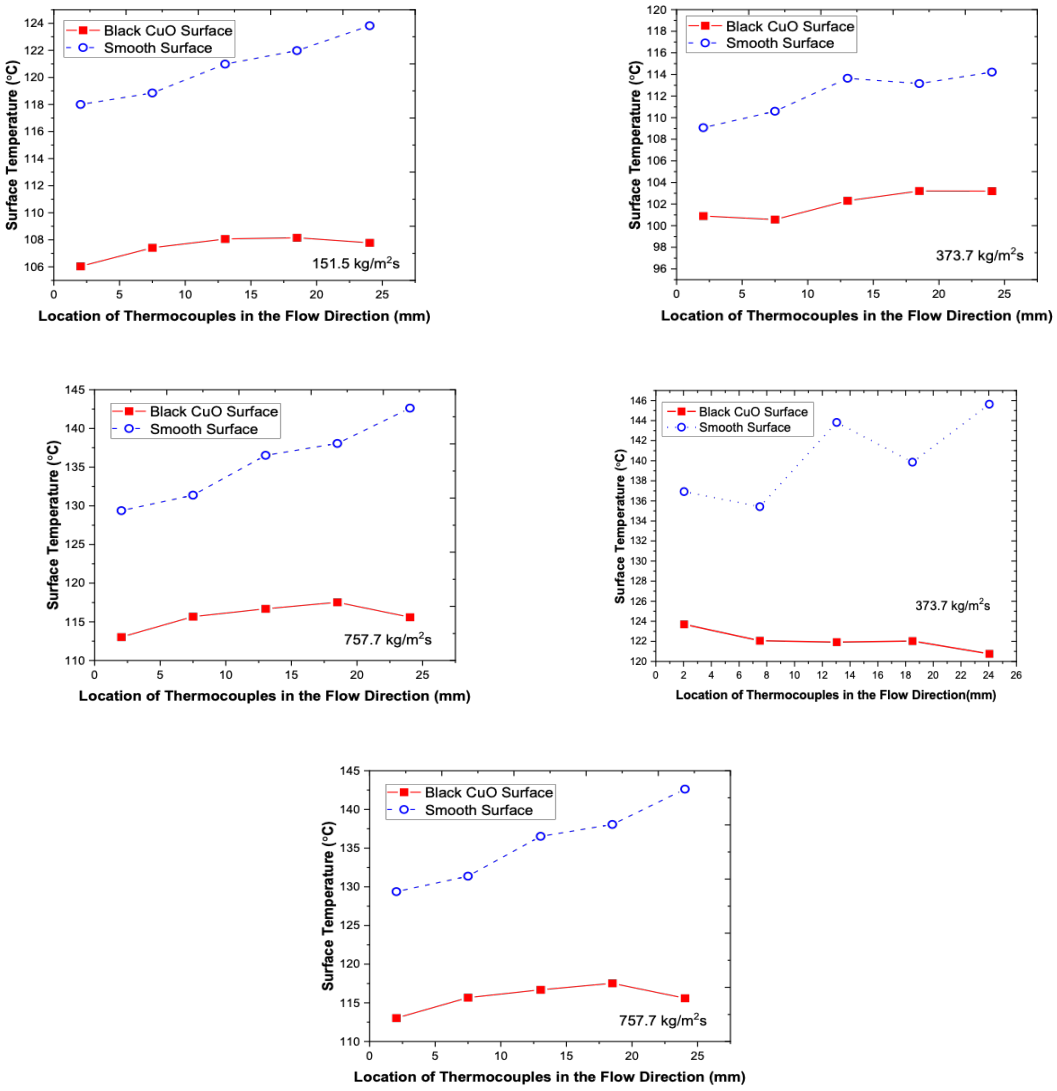

Figure 4.9: Temperature distribution in two-phase heat transfer on the heating wall in a microgap along the flow direction.

4.7.2 Statistical Analysis

The enhancement for both single-phase convective heat transfer should be a result of a more evenly distributed surface temperature on the heating surface.

To compare the variation of surface temperature over the location of thermocouples in the flow direction between the Black CuO surface and the smooth surface, different statistical analyses were conducted.

First, the variance calculated as $s^2 = \sum_i^n (x_i - \bar{x})^2/(n-1)$ is a straightforward tool to compare the variation of variables where x_i is the observation, $\bar{x}$ is the sample mean and n is the sample size. A smaller variation results in a smaller value of variance. Secondly, the boxplot is a method for graphically depicting groups of numerical data through their quartiles, specifically, are the minimum, the maximum, the medium, the 25th percentile and the 75th percentile. Boxplots have lines extending from the boxes and whiskers indicating data distribution and variability. Side-by-side boxplots can be drawn for different groups comparison. The shorter a boxplot is, the less variability the data has.

Thirdly, to do inference and see if experimental results are repeatable in the long run, F-test is applied to compare the true variance of two groups. F-test has an F distribution under the null hypothesis that $H_0 : s_1^2 = s_2^2$. The alternative hypothesis used in this project is the two-tail test of two groups variances are different such that $H_\alpha : s_1^2 \neq s_2^2$. The test statistic is $F = s_1^2/s_2^2$ which equals 1 when the variances are equal. The assumption for F-test that the population is approximately normally distributed can be checked by using shapiro test. The conclusion from F-test is drawn based on p-value. Statistically, if the p-value is less than some predetermined significance level, i.e., $p < 0.05$, then the true variances from the two groups are significantly different. Otherwise, there is no significant difference between the two groups variances.

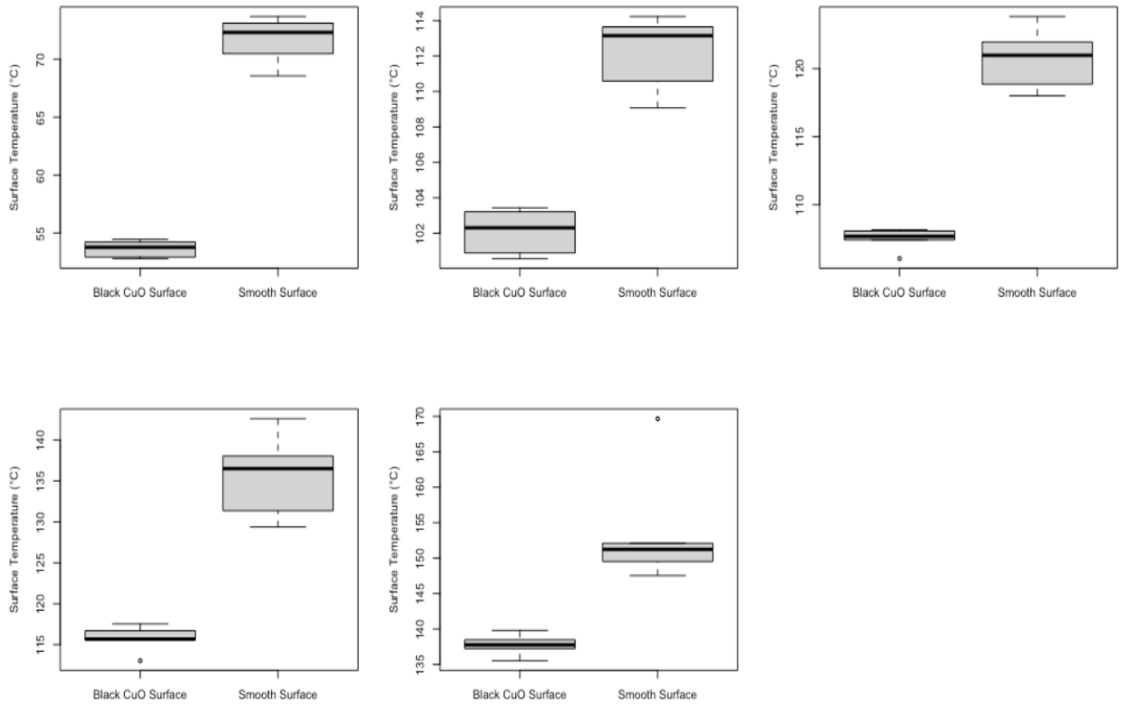

Figure 4.10: Statistical Analysis on the Uniformity of the Temperature

The side-by-side boxplots in Figure 4.10 show that for the five groups comparisons, the Black CuO surface has much less variation in surface temperature than the smooth face with much shorter boxplot. Shapiro-Wilk normality test shows the normality distribution assumption is satisfied. Almost all the F-tests providing p-value < 0.05 indicate that the Black CuO surface is significantly more uniform in temperature compared to the smooth surface, except for the case 2, which may not have significant variance differences in temperature.

The black CuO nano-structured coated surface was effective in enabling more evenly distributed surface temperature as shown in Figure 4.8. At a low input heat flux, single-phase convective heat transfer is dominant and the surface temperature goes up from the inlet to the outlet due to the diminishing entrance effects and the reduced temperature difference between fluid and the heating walls.

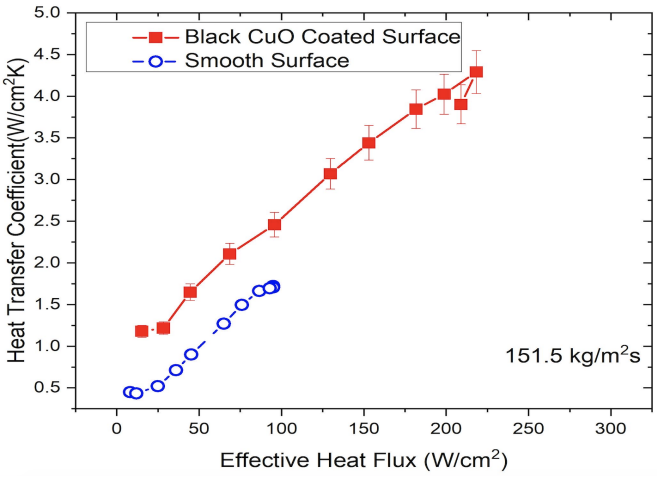

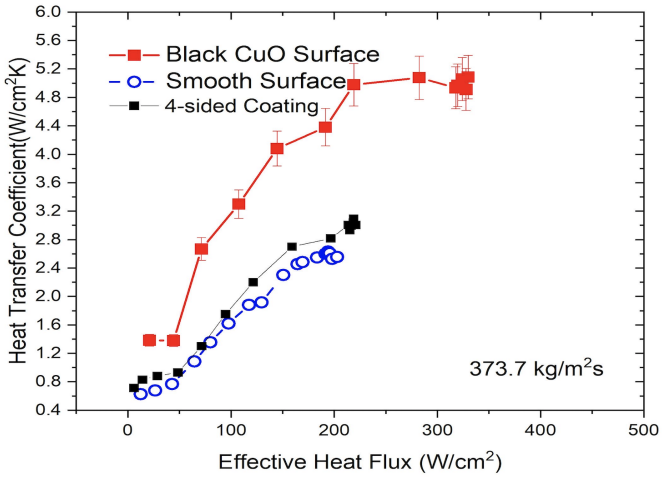

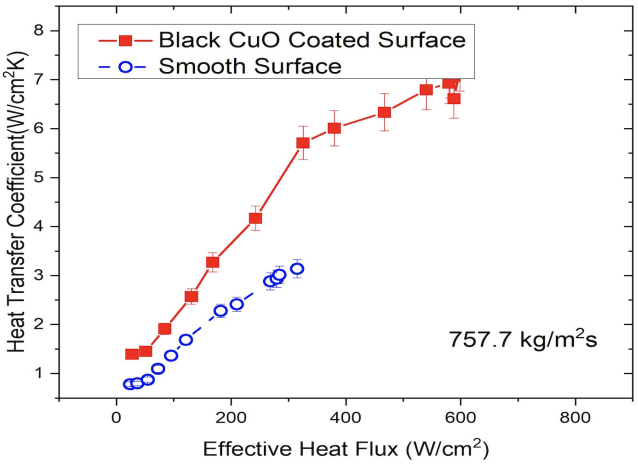

Figure 4.11: Boiling heat transfer coefficient for Black CuO coated surface and smooth surface.

The black CuO nanowires are highly desired in increasing heat transfer rates (Figure 4.11) by forming a thin film liquid on the surface and effectively cooling the hot areas. These effects effectively achieve a more uniform temperature distribution and reduces the average surface temperature (Figure 4.8, 4.9).

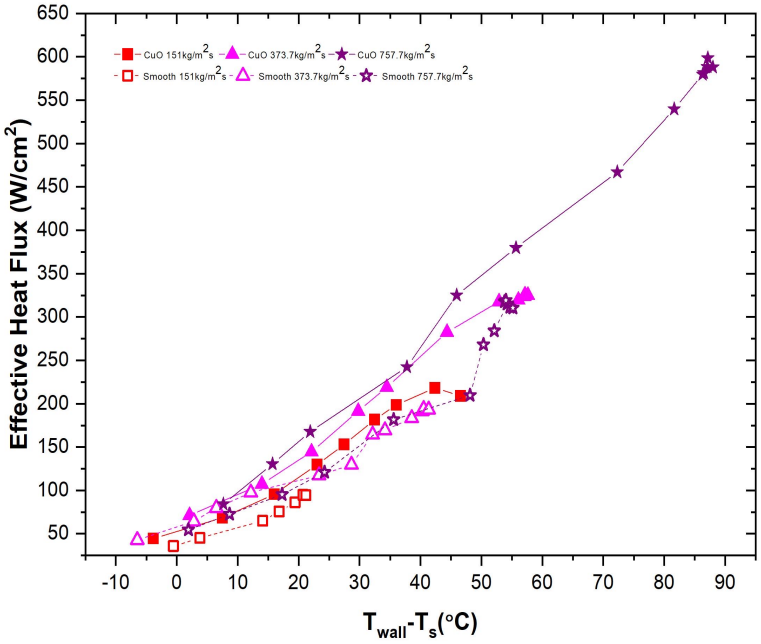

Figure 4.12: Boiling Curve

In the flow boiling study, vapor quality is an important parameter to describe vapor mass fraction in a saturated mixture. Saturated liquid has a vapor quality of 0% and saturated vapor has a vapor quality of 100%. Vapor quality of flow boiling revealed phase change capacity of the microgap. In Figure 4.14, vapor quality at the outlet of the microgap was calculated in the condition of CHF, at the mass flux from 151.5 kg/m^2s to 757.7 kg/m^2s. For the flow boiling in bare copper surface microgap, in the CHF condition, the vapor quality at the outlet is less than 0.2 for all mass flux. This is mainly because the early annular flow induced dry-out was reached and the bubbles generated by the nucleate boiling is fewer than that of black CuO microgap.

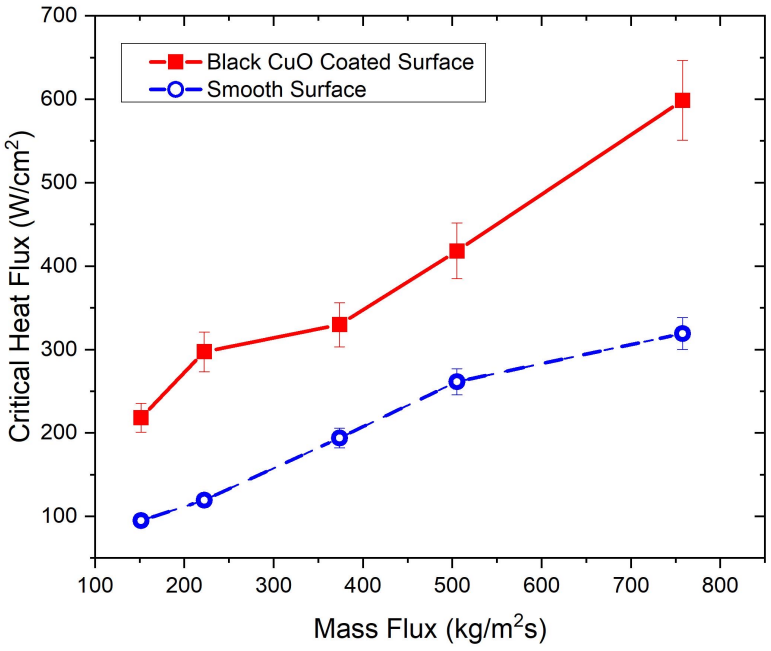

Figure 4.13: Critical Heat Flux for the black CuO coated surface and smooth surface.

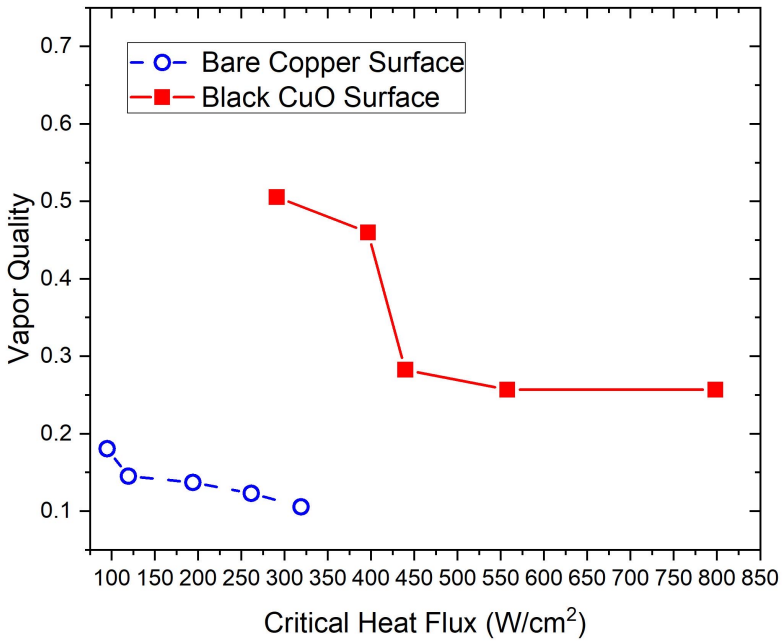

Figure 4.14: Critical Heat Flux for the black CuO coated surface and bare copper surface.

For the flow boiling in black CuO coated surface microgap. When the mass flux was lower, the vapor quality can reach 0.68 at the mass flux of 151.5 kg/m^2s. This is mainly because the two-layer flow was dominant at a lower mass flux. Thin film liquid boiling can generate much more vapor bubbles than bulk liquid, which can delay the annular flow and the local dryout process. The sudden drop of the vapor quality happened from mass flux 222.2 kg/m^2s to 373.7 kg/m^2s. As mentioned in previous subsection, the thin film liquid flow was driven by the strong capillary force of the black CuO surface. When the flow velocity and heat input keep increasing, the thin film liquid boiling was not effective than that of at lower heat and mass flux. While the overall phase change on the black CuO coated surface is much more effective than that of on the bare copper surface.

4.7.3 Enhanced CHF, Heat Transfer Coefficient and pressure drop

For now, at all flow, the CHF for black CuO surface can approach about two times of that on bare surface (Figure 4.13), which is significantly improved. This is due to the increase of the capillarity induced increase of the thin film liquid flow. Because of the two layer flow mentioned in previous sections, the thin film liquid flows faster than the bulk flow and moreover, the thin film liquid boiling is more effective to remove heat from the surface. Due to the lower layer thin film liquid flow, bubbles generated in the thin film liquid flow can be departed at a super small size and carried away by the bulk flow at a high frequency. No large slugged bubbles in the microgap during the nucleation boiling process cause no local dry-out at a lower heat flux. High frequency rewetting processes also cause the decreasing surface temperature and delay the local dry-out process, so that increase the CHF significantly.

As shown in Figure 4.11, heat transfer increased about 168% and 40% at the heat flux of 25 W/cm^2 and 91 W/cm^2, respectively, at a mass flux of 151.5 kg/m^2s. The enhancement of heat transfer coefficient at lower surface temperature is mainly

because of higher surface roughness, surface wettability and the coating-promoted nucleate boiling. While at a higher heat flux, the less increase of HTC could result from the additional thermal resistance compared with those at lower heat flux. The overall heat transfer coefficient could achieve up to 150% with a slightly pressure drop increase.

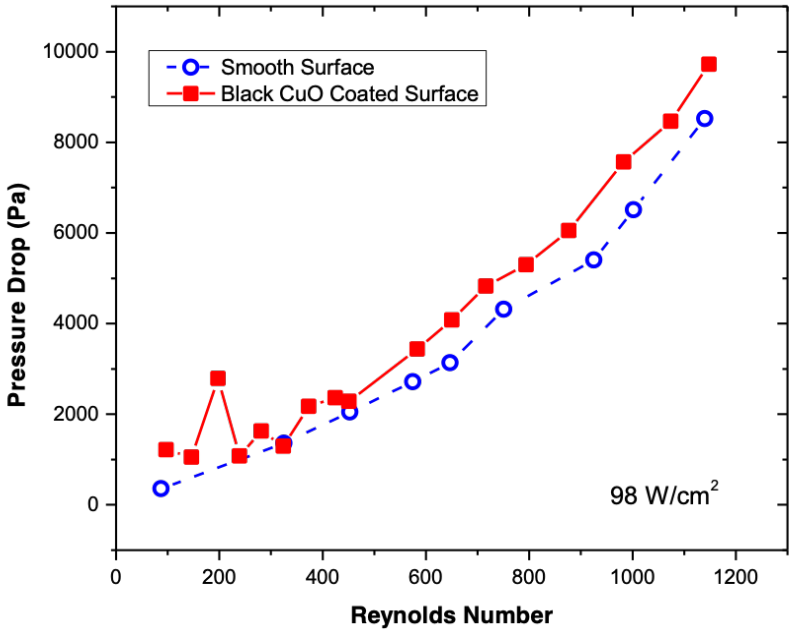

Figure 4.15: Pressure drop for bare surface and Black CuO surface at the heat flux of $98 W/cm^2$.

Figure 4.15 shows the results of pressure drop for the two surfaces: bare copper surface, black CuO coated surface at different Reynolds number. Compared to bare copper surface, the maximum pressure drop increased for CuO coated surface. For CuO coated surface, at Reynolds number equals to 200, there was a peak in the curve. That is mainly because it was two-phase flow in the channel, which caused the higher pressure drop compared with pressure drops at nearby Reynolds number ($220 \leq$ Re ≤ 500). The pressure drop increase at high Reynolds number for it is mainly due to

the introduced surface roughness of the black CuO. High roughness introduced high flow resistance, which could increase pressure drop.

4.8 Results Comparison with other outstanding studies

Results comparison with Copper Nanowire

In the few decades, a large number of outstanding studies were investigated on flow boiling in microgap. Among them, flow boiling in microgaps on copper substrate were developing very fast. A lot of researchers study the flow boiling in various coatings on copper surface. Copper nanowires and carbon nanotubes were the most popular coatings applied to the flow boiling studies.

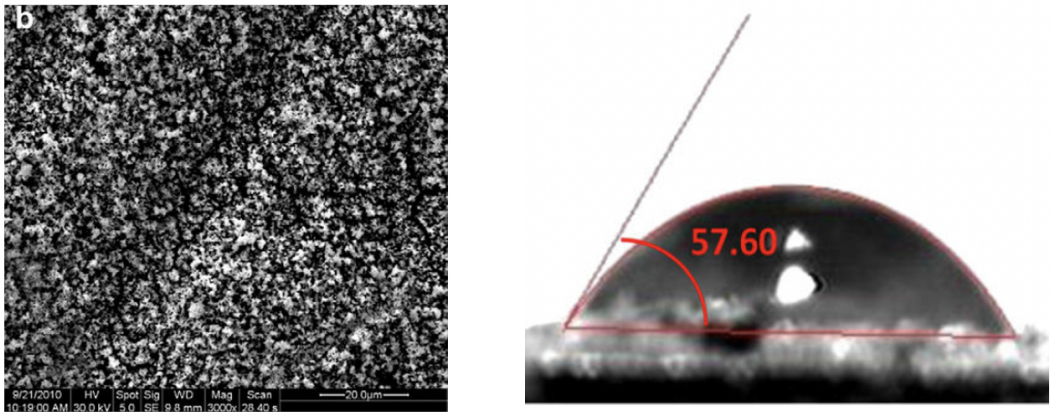

Figure 4.16: SEM picture of Copper Nanowire Surface and Contact Angle of water on Copper Nanowire Surface (Morshed, Paul, and Khan, 2012).

In the Moshed's study, he studied the flow boiling in microgap with copper nanowire coatings surface (Morshed, Paul, and Khan, 2012). The characteristic of copper nanowire is shown in Figure 4.16. The contact angle of water on copper nanowire surface was 57.6 $°C$ compared with that on black CuO coated surface about 5 $°C$. The difference of contact angle could cause different surface capillary force and bubble departure diameter. The microcavity size of copper nanowire was found to be from 1 μm to 10 μm, and are not uniform on the surface. This could

cause the significant difference of surface active nucleation density. The height of the copper nanowire was about 60 μm compared with 1.5 μm of black CuO coatings. Thus, much higher thermal resistance could cause the less increase of HTC and CHF. In Moshed's study, for the visualization results, bubble nucleation and bubble flow pattern for copper nanowire coated surface has been observed to be similar to that of bare copper surface. This was mainly because of the wettability of those two surface was likely to be similar. Thus, the rewetting process cannot be that efficient on copper nanowire surface. These could cause the increasing of the surface temperature and lower the CHF and HTC compared with those of black CuO coated surface.

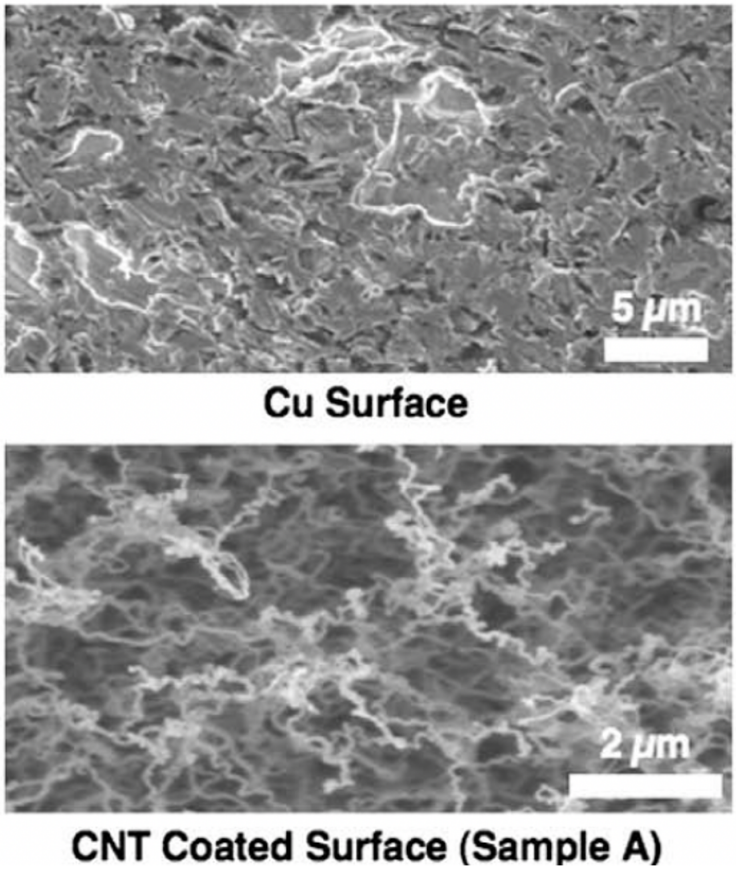

Figure 4.17: SEM picture of Carbon Nano Tube surface (Khanikar, Mudawar, and Fisher, 2009).

In Mudarwar's and Khanikar's study, they tested the flow boiling in microgap with carbon nanotube coated surface(Khanikar, Mudawar, and Fisher, 2009). The characteristic of the CNT is shown in Figure 4.17. The CNT coating was formed by microwave plasma chemical vapor deposition (MPCVD). In their study, they found that large contact resistance between the CNT coating and the copper surface was caused by the coating fabrication process. There were also two main issues of the CNT coating. The first is that it is difficult in assessing the orientation, density and quality of CNT coating anchoring to the large size copper surface. The second issue is that high flow velocities could fold the CNT coatings towards the wall. These issues could reduce the depth of CNT coatings induced microcavities. Thus, in their study, heat transfer performance enhancement was not high enough at higher mass flux. At a lower mass flux, the main increasing mechanism of black CuO coating was higher nucleation density, which can cause much more bubbles generated on the surface and thus remove the heat from the surface. The lower CHF in their studies compare with that of bare copper surface microgap in my study was mainly because the dimension of the channel was different. And the hydraulic diameter of the microgap in my study is smaller than that in Mudarwar's and Khnikar's study.

4.9 Conclusions

The effect of a new type of copper nanowire on single and two-phase convective heat transfer performance of a microgap heat sink has been investigated experimentally in this study. For a given microgap size, heat transfer performance enhancement in both single and two-phase regime were demonstrated in low and high flow rate conditions. The nano-structure black CuO coating can significantly increase the heat transfer performance with slightly pressure drop increasing. The main flow boiling pattern has been visualized using a high speed camera. The main conclusions are drawn as follows,

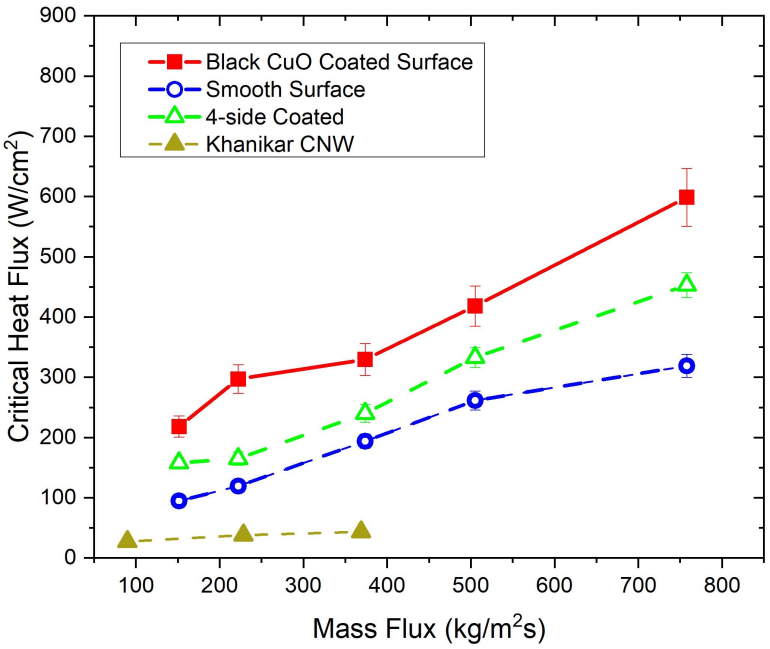

Figure 4.18: Results Comparison with Khanikar's and Mudarwar's (1)

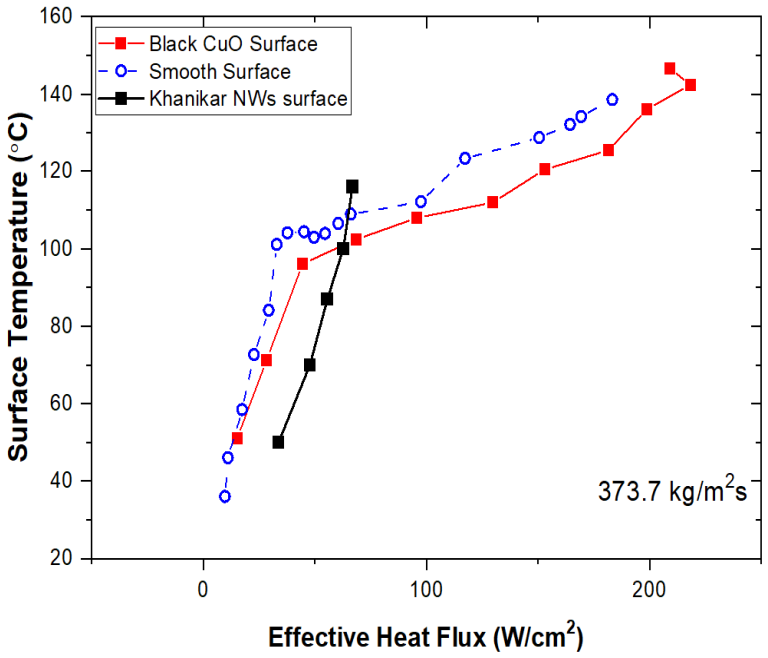

Figure 4.19: Results Comparison with Khanikar's and Mudarwar's (2)

(a) According to the water surface tension force, the flows through the microgap could rewet the dry-out surface and enhance the CHF significantly. The enhancement of CHF is up to $\sim$ 130% at the flow rate 25 kg/m^2s.

(b) Induced by the rewetting process, the black CuO coated surface temperature reduced up to $\sim$ 30 $^\circ C$ at low heat flux conditions compared with bare surface. The highest wall temperature of black CuO coated surface could withstand up to 35 $^\circ C$ higher than that of bare copper surface as observed in this study.

(c) The enhancement of single-phase HTC could achieve up to 168% at the flow rate of 38 kg/m^2s. However, for two-phase HTC, the increasing was not as high as that of single-phase, because of the mean water temperature. The enhancement of HTC of two-phase could also reach up to 40% at the same input heat flux. For the overall HTCs, the enhancement could achieve up to 150% with a slight pressure drop increase.

(d) The surface temperature along the flow direction became more uniform at both single and two-phase.

Chapter 5

Conclusion and Future Study

5.1 Conclusion

The present study investigated the flow boiling heat transfer in microgap for the purpose of developing compact cooling systems which can be applied to miniaturized power components. Surface treatments at nano- and microscales were used as innovative techniques to improve the heat transfer performance as well as to delay the associated local dry-out. To achieving these goals, flow boiling experiments were performed in order to highlight the impact of nanocoatings on nucleate boiling processes, especially on bubble growth and departure mechanisms.

The interest in nanocoatings was firstly inspired by the emergence of nanofluids for which, recent studies show that during nanofluid boiling, nanoparticles deposit on the heated surface, leading to modifications of the surface wettability, the heat transfer coefficient and the critical heat flux. However, due to controversial results in the literature, the role of nanoparticle deposition on boiling heat transfer is not fully understood yet, and further works is required for a better understanding of the involved mechanisms.

Therefore, in the first part of this work, experiments were performed to explore the mechanism of flow boiling on super hydrophilic surface as well as its impact on flow boiling on a smooth surface. For the surface with almost near-zero-contact angle, water can effectively wet and penetrate coatings. Those microcavities are ideal for vapor embryo formation. Thus surface with much more cavities than other coated

surfaces can provide an ideal environment for increased bubble nucleation sites. More nucleation site density and more microcavities can also provide much more surface area, which can increase CHF and HTC significantly.

Moreover, Two-layer flow was observed in this study. The lower layer flow was observed to be faster than the bulk flow. The lower layer flow could be driven by both pump and also the strong capillary force. Thin film evaporation could be more effective. And the rewetting process is faster than that on other surfaces.

There was no large amount and large size bubble observed during the boiling process in black CuO coated microgap. That might because a large amount of bubble was formed on the lower layer flow (thin film) and departure at a super small size, and then flushed away to the outlet.

Therefore, intrinsic surface wettability is critical for boiling heat transfer. Improving the wettability could significantly increase the nucleate boiling and enhance the CHF and HTC of capillary boiling. The super hydrophilic surface functionalized black CuO can create ideal interfaces for nucleate boiling, resulting in enhanced HTC and CHF during boiling and evaporation.

5.2 Future Work

In the future, it will definitely be interesting to characterize the surfaces with heterogeneous properties of wettability, such as, a super hydrophobic surface containing artificial unwetted nucleation sites. Graphene is widely using for studies in the last decades. Graphene has a high thermal conductivity on both vertical and horizontal directions. Copper based Nickel-Graphene has great job on duration and attachment. Such surfaces will probably allow a super high CHF on the surface. In terms of hydrodynamics, the two-phase pressure drop would be decreased. In terms of heat transfer, the heat transfer coefficient would be enhanced.

Furthermore, flows on copper surface with varies of geometric structures should be investigate. A novel structure based on microchannels has been developed for enhance heat transfer performance, called bridged microchannels. There are five microchannels on the surface with bridges between them. This structure may change the flow pattern by switching the bubbles at the onset boiling process. In addition the nanoporous surfaces with partial wetting might track nanobubbles and yield drag reduction. These fundamental studies may substantially advance flow boiling performance.

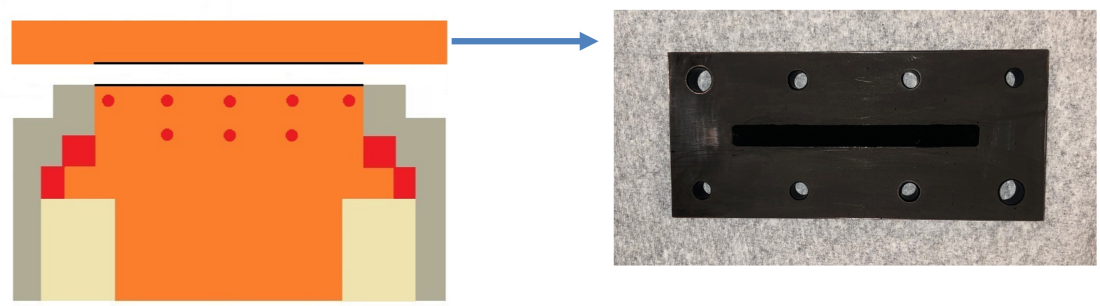

Figure 5.1: Microgap with nanostructured walls (4-side coating).

In order to study the scalability of flow boiling in microgap with nanostructured walls in stead of that of single coated wall. Another experiment was done in this study. As shown in Figure 5.1, four sides of the wall in the microgap were coated with black CuO. The test setup and experiment processes were the same with those of previous study in this dissertation.

5.2.1 Results and discussions

As shown in Figure 5.2 and Figure 5.3, the CHF enhancement was 70% and 45% compared with those of bare copper surface at the mass flux of 151.5 kg/m^2s and 737.7 kg/m^2s, respectively. And HTC enhancement was 18% at the heat flux of $135W/cm^2$ But the enhancement was lower than that of black CuO coated surface. This may because of the separation of the flow in the microgap for two-phase flow

boiling, which could cause the less liquid flow in the microgap. Further tests and visualization studies should be done in the future.

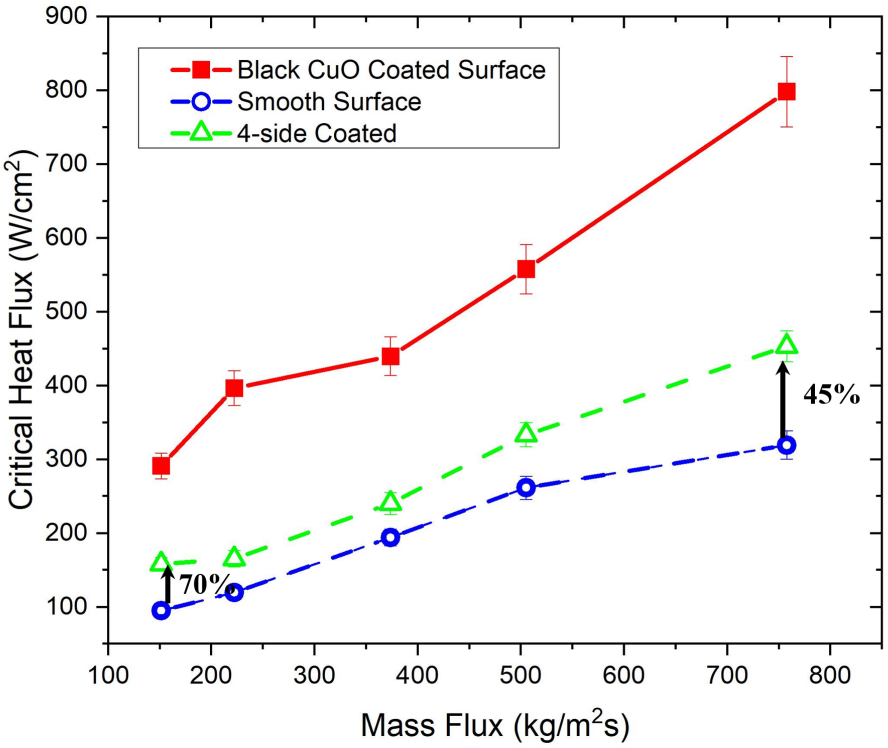

Figure 5.2: Increasing effective heat flux in 4-side coated walls microgap.

For the pressure drop results in Figure 5.4, 46% reduction of pressure drop at Re=230 was found in this study. This may due to the effectively managing the bubble confinement, and separating liquid and vapor flows. More data and tests are necessary in the future study.Another issue we notice during the experiment process was that the temperature of the outlet was always below 100 $^{\circ}C$. This may because the flow separated during the nucleate boiling process. Partial of the liquid flows on the top side of the microgap and cannot be heated to vapor phase. This may cause the outlet temperature below the saturation temperature. More test should be done to prove this phenomenon.

However, the visualization study of flow boiling in nanostructured coated walls in microgap is a big challenge for this research. Thus, it is difficult to find out the

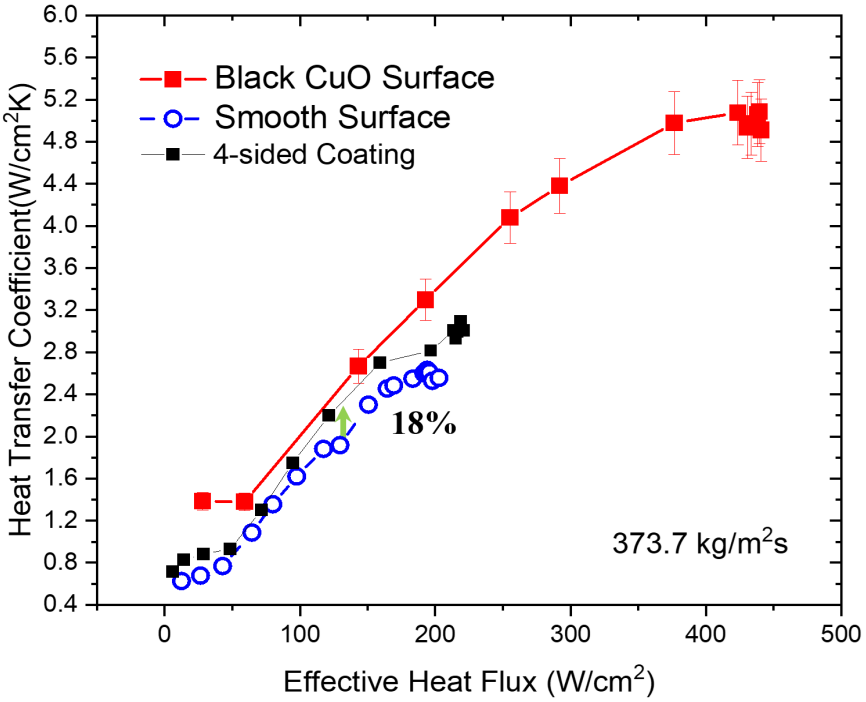

Figure 5.3: Increasing heat transfer coefficient in 4-side coated walls microgap.

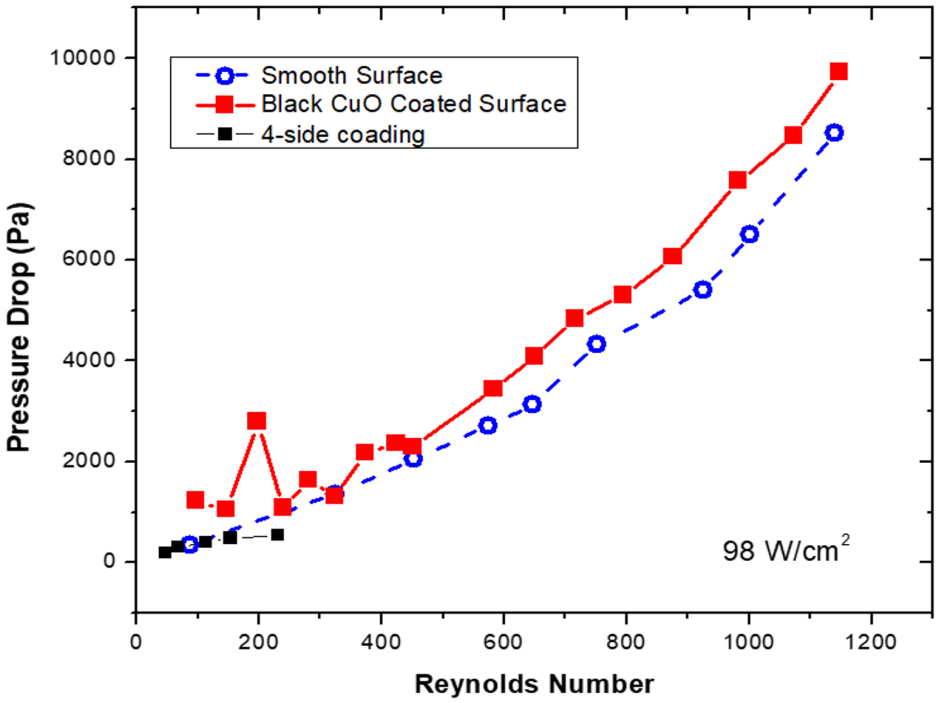

Figure 5.4: Pressure drop in 4-side coated walls microgap.

mechanism of the enhancement of the heat transfer and also the reduction of the pressure drop. The design of the experiment was also need to be discussed. For a microgap with nanostructure coated walls, heating from all the sides of the walls could be better to find out the mechanism and also for the electronic devices in nowadays.

Bibliography

Ahmad, Ishaq and Chi-wai Kan (2016). "A review on development and applications of bio-inspired superhydrophobic textiles". In: *Materials* 9.11, p. 892.

Alam, Tamanna, Poh Seng Lee, Christopher R Yap, and Liwen Jin (2011). "Experimental investigation of microgap cooling technology for minimizing temperature gradient and mitigating hotspots in electronic devices". In: *2011 IEEE 13th Electronics Packaging Technology Conference*. IEEE, pp. 530–535.

Alam, Tamanna, Poh Seng Lee, Christopher R Yap, and Liwen Jin (2013). "A comparative study of flow boiling heat transfer and pressure drop characteristics in microgap and microchannel heat sink and an evaluation of microgap heat sink for hotspot mitigation". In: *International Journal of Heat and Mass Transfer* 58.1-2, pp. 335–347.

Alam, Tamanna, Poh Seng Lee, Christopher R Yap, Liwen Jin, and K Balasubramanian (2012). "Experimental investigation and flow visualization to determine the optimum dimension range of microgap heat sinks". In: *International journal of heat and mass transfer* 55.25-26, pp. 7623–7634.

Balasubramanian, Prabhu and Satish G Kandlikar (2005). "Experimental study of flow patterns, pressure drop, and flow instabilities in parallel rectangular minichannels". In: *Heat Transfer Engineering* 26.3, pp. 20–27.

Baptista, Andresa, Francisco Silva, Jacobo Porteiro, José Míguez, and Gustavo Pinto (2018). "Sputtering physical vapour deposition (PVD) coatings: A critical review on process improvement and market trend demands". In: *Coatings* 8.11, p. 402.

Bar-Cohen, Avram and Emil Rahim (2007). "Modeling and prediction of two-phase refrigerant flow regimes and heat transfer characteristics in microgap channels". In: *International Conference on Nanochannels, Microchannels, and Minichannels*. Vol. 4272, pp. 1141–1160.

Bar-Cohen, Avram and Emil Rahim (2009). "Modeling and prediction of two-phase microgap channel heat transfer characteristics". In: *Heat Transfer Engineering* 30.8, pp. 601–625.

Bar-Cohen, Avram, Peng Wang, and Emil Rahim (2007). "Thermal management of high heat flux nanoelectronic chips". In: *Microgravity Science and Technology* 19.3-4, pp. 48–52.

Béa, H, M Bibes, M Sirena, G Herranz, K Bouzehouane, E Jacquet, S Fusil, Patrycja Paruch, Matthew Dawber, J-P Contour, et al. (2006). "Combining half-metals and multiferroics into epitaxial heterostructures for spintronics". In: *Applied physics letters* 88.6, p. 062502.

Bergles, AE (1977). "Review of instabilities in two-phase systems". In: *Two-phase flows and heat transfer, Vol. 1*.

Bergles, AE and SG Kandlikar (2005). "On the nature of critical heat flux in microchannels". In: *J. Heat Transfer* 127.1, pp. 101–107.

Bergles, Arthur E, John H Lienhard V, Gail E Kendall, and Peter Griffith (2003). "Boiling and evaporation in small diameter channels". In: *Heat transfer engineering* 24.1, pp. 18–40.

Billard, Alain and Frédéric Perry (2005). "Pulvérisation cathodique magnétron". In: *Techniques de l'ingénieur. Matériaux métalliques* M1654.

Billy, E, F Maillard, A Morin, L Guetaz, F Emieux, C Thurier, P Doppelt, S Donet, and S Mailley (2010). "Impact of ultra-low Pt loadings on the performance of anode/cathode in a proton-exchange membrane fuel cell". In: *Journal of Power Sources* 195.9, pp. 2737–2746.

Binnig, Gerd, Calvin F Quate, and Ch Gerber (1986). "Atomic force microscope". In: *Physical review letters* 56.9, p. 930.

Binnig, Gerd and Heinrich Rohrer (1987). "Scanning tunneling microscopy—from birth to adolescence (Nobel Lecture)". In: *Angewandte Chemie International Edition in English* 26.7, pp. 606–614.

Boure, JA, AE Bergles, and LS Tong (1973). "Review of two-phase flow instability". In: *Nuclear engineering and design* 25.2, pp. 165–192.

Brutin, David, Frederic Topin, and Lounes Tadrist (2003). "Experimental study of unsteady convective boiling in heated minichannels". In: *International Journal of Heat and Mass Transfer* 46.16, pp. 2957–2965.

Callizo, Claudi Marti´ n, Rashid Ali, and Bjo¨ rn Palm (2008). "Dryout incipience and critical heat flux in saturated flow boiling of refrigerants in a vertical uniformly heated microchannel". In: *International Conference on Nanochannels, Microchannels, and Minichannels*. Vol. 48345, pp. 705–712.

Caney, Nadia, Philippe Marty, and J Bigot (2006). "Experimental Flow Boiling Study in Mini-Channels". In: *International Heat Transfer Conference 13*. Begel House Inc.

Cassie, ABD and S Baxter (1944). "Wettability of porous surfaces". In: *Transactions of the Faraday society* 40, pp. 546–551.

Chen, H, X Chen, Y Zhang, and Y Xia (2007). "Ablation induced by single-and multiple-femtosecond laser pulses in lithium niobate". In: *Laser Physics* 17.12, pp. 1378–1381.

Chen, John C (1966). "Correlation for boiling heat transfer to saturated fluids in convective flow". In: *Industrial & engineering chemistry process design and development* 5.3, pp. 322–329.

Dai, Xianming (2013). "Boiling and Evaporation on Micro/nanoengineered Surfaces". In:

Dai, Xianming, Fanghao Yang, Ruixian Fang, Tsegaye Yemame, Jamil A Khan, and Chen Li (2013). "Enhanced single-and two-phase transport phenomena using flow separation in a microgap with copper woven mesh coatings". In: *Applied thermal engineering* 54.1, pp. 281–288.

David, T, D Mendler, A Mosyak, A Bar-Cohen, and G Hetsroni (2014). "Thermal management of time-varying high heat flux electronic devices". In: *Journal of Electronic Packaging* 136.2.

Drogowska, Maria, Louis Brossard, and Hugues Ménard (1988). "Influence of anions on the passivity behavior of copper in alkaline solutions". In: *Surface and Coatings Technology* 34.4, pp. 383–400.

Dupré, Athanase and Paul Dupré (1869). *Théorie mécanique de la chaleur*. Gauthier-Villars.

Faghri, Amir and Zhen Guo (2005). "Challenges and opportunities of thermal management issues related to fuel cell technology and modeling". In: *International Journal of Heat and Mass Transfer* 48.19-20, pp. 3891–3920.

Fang, Ruixian (2011). "Experimental and numerical analysis of enhanced microchannel cooling using micro-synthetic jets". PhD thesis. University of South Carolina.

Fowkes, Frederick M (1964). "Attractive forces at interfaces". In: *Industrial & Engineering Chemistry* 56.12, pp. 40–52.

Gao, Lichao and Thomas J McCarthy (2007). "How Wenzel and Cassie were wrong". In: *Langmuir* 23.7, pp. 3762–3765.

Garimella, Suresh V (2006). "Advances in mesoscale thermal management technologies for microelectronics". In: *Microelectronics Journal* 37.11, pp. 1165–1185.

Good, Robert J and LA Girifalco (1960). "A theory for estimation of surface and interfacial energies. III. Estimation of surface energies of solids from contact angle data". In: *The Journal of Physical Chemistry* 64.5, pp. 561–565.

Gu, Yongan Peter (2015). "Contact angle measurement techniques for determination of wettability". In: *Encyclopedia of surface and colloid science*. CRC Press, pp. 1491–1504.

Guo, Dong, JJ Wei, and YH Zhang (2011). "Enhanced flow boiling heat transfer with jet impingement on micro-pin-finned surfaces". In: *Applied Thermal Engineering* 31.11-12, pp. 2042–2051.

Han, Xuefei, Andrei Fedorov, and Yogendra Joshi (2016). "Flow boiling in microgaps for thermal management of high heat flux microsystems". In: *Journal of Electronic Packaging* 138.4.

Hannemann, RJ (2003). *Thermal control of electronics: Perspectives and prospects*. Tech. rep.

He, Bo, Neelesh A Patankar, and Junghoon Lee (2003). "Multiple equilibrium droplet shapes and design criterion for rough hydrophobic surfaces". In: *Langmuir* 19.12, pp. 4999–5003.

Hetsroni, G, A Mosyak, Z Segal, and E Pogrebnyak (2003). "Two-phase flow patterns in parallel micro-channels". In: *International Journal of Multiphase Flow* 29.3, pp. 341–360.

Huo, X, YS Tian, VV Wadekar, and TG Karayiannis (2001). "Review of Aspects of Two Phase Flow and Boiling Heat Transfer in Small Diameter Tubes". In: *Compact Heat Exchangers and Enhancement Technology for the Process Industries, Davos, Switzerland*, pp. 335–346.

Isaacs, Steven A, Yogendra Joshi, Yue Zhang, Muhannad S Bakir, and Yoon Jo Kim (2013). "Two-phase flow and heat transfer in pin-fin enhanced micro-gaps with non-uniform heating". In: *International Conference on Micro/Nanoscale Heat Transfer*. Vol. 36154. American Society of Mechanical Engineers, V001T12A003.

Isaacs, Steven A, Yoon Jo Kim, Andrew J McNamara, Yogendra Joshi, Yue Zhang, and Muhannad S Bakir (2012). "Two-phase flow and heat transfer in pin-fin en-

hanced micro-gaps". In: *13th InterSociety Conference on Thermal and Thermomechanical Phenomena in Electronic Systems*. IEEE, pp. 1084–1089.

Kakac, S and B Bon (2008). "A review of two-phase flow dynamic instabilities in tube boiling systems". In: *International Journal of Heat and Mass Transfer* 51.3-4, pp. 399–433.

Kandlikar, Satish, Srinivas Garimella, Dongqing Li, Stephane Colin, and Michael R King (2005). *Heat transfer and fluid flow in minichannels and microchannels*. elsevier.

Kandlikar, Satish G (2002a). "Fundamental issues related to flow boiling in minichannels and microchannels". In: *Experimental Thermal and Fluid Science* 26.2-4, pp. 389–407.

Kandlikar, Satish G (2002b). "Two-phase flow patterns, pressure drop, and heat transfer during boiling in minichannel flow passages of compact evaporators". In: *Heat Transfer Engineering* 23.1, pp. 5–23.

Kandlikar, Satish G (2012). "History, advances, and challenges in liquid flow and flow boiling heat transfer in microchannels: a critical review". In: *Journal of heat transfer* 134.3.

Kandlikar, Satish G and William J Grande (2003). "Evolution of microchannel flow passages–thermohydraulic performance and fabrication technology". In: *Heat transfer engineering* 24.1, pp. 3–17.

Kandlikar, Satish G, Wai Keat Kuan, Daniel A Willistein, and John Borrelli (2006). "Stabilization of flow boiling in microchannels using pressure drop elements and fabricated nucleation sites". In:

Kennedy, JE, GM Roach Jr, MF Dowling, SI Abdel-Khalik, SM Ghiaasiaan, SM Jeter, and ZH Quershi (2000). "The onset of flow instability in uniformly heated horizontal microchannels". In: *J. Heat Transfer* 122.1, pp. 118–125.

Kew, Peter A and Keith Cornwell (1997). "Correlations for the prediction of boiling heat transfer in small-diameter channels". In: *Applied thermal engineering* 17.8-10, pp. 705–715.

Khanikar, Vikash, Issam Mudawar, and Timothy Fisher (2009). "Effects of carbon nanotube coating on flow boiling in a micro-channel". In: *International Journal of Heat and Mass Transfer* 52.15-16, pp. 3805–3817.

Kim, Dae Whan, Emil Rahim, Avram Bar-Cohen, and Bongtae Han (2008). "Thermofluid characteristics of two-phase flow in micro-gap channels". In: *2008 11th*

Intersociety Conference on Thermal and Thermomechanical Phenomena in Electronic Systems. IEEE, pp. 979–992.

Kim, Dae-Whan, Emil Rahim, Avram Bar-Cohen, and Bongtae Han (2010). "Direct submount cooling of high-power LEDs". In: *IEEE Transactions on Components and Packaging Technologies* 33.4, pp. 698–712.

Koşar, Ali and Yoav Peles (2006). "Convective flow of refrigerant (R-123) across a bank of micro pin fins". In: *International Journal of Heat and Mass Transfer* 49.17-18, pp. 3142–3155.

Koşar, Ali and Yoav Peles (2007). "Boiling heat transfer in a hydrofoil-based micro pin fin heat sink". In: *International Journal of Heat and Mass Transfer* 50.5-6, pp. 1018–1034.

Krishnamurthy, Santosh and Yoav Peles (2008). "Flow boiling of water in a circular staggered micro-pin fin heat sink". In: *International Journal of Heat and Mass Transfer* 51.5-6, pp. 1349–1364.

Kuo, C-J and Y Peles (2008). "Flow boiling instabilities in microchannels and means for mitigation by reentrant cavities". In: *Journal of Heat Transfer* 130.7.

Kuo, Cheng Yung and Chie Gau (2010). "Control of superhydrophilicity and superhydrophobicity of a superwetting silicon nanowire surface". In: *Journal of The Electrochemical Society* 157.9, K201.

Lafuma, Aurélie and David Quéré (2003). "Superhydrophobic states". In: *Nature materials* 2.7, pp. 457–460.

Lee, Han Ju and Sang Yong Lee (2001a). "Heat transfer correlation for boiling flows in small rectangular horizontal channels with low aspect ratios". In: *International Journal of Multiphase Flow* 27.12, pp. 2043–2062.

Lee, Han Ju and Sang Yong Lee (2001b). "Pressure drop correlations for two-phase flow within horizontal rectangular channels with small heights". In: *International journal of multiphase flow* 27.5, pp. 783–796.

Lie, YM, JH Ke, WR Chang, TC Cheng, and TF Lin (2007). "Saturated flow boiling heat transfer and associated bubble characteristics of FC-72 on a heated micro-pin-finned silicon chip". In: *International Journal of Heat and Mass Transfer* 50.19-20, pp. 3862–3876.

Lin, Liwei (1991). "Bubble forming on a micro line heater". In: *Proceedings of ASME Winter Annual Meeting, Micromechanical Sensors, Actuators and Systems, 1991*, pp. 147–163.

Lu, Chun Ting and Chin Pan (2008). "Stabilization of flow boiling in microchannel heat sinks with a diverging cross-section design". In: *Journal of Micromechanics and microengineering* 18.7, p. 075035.

Ma, Aixiang, Jinjia Wei, Minzhe Yuan, and Jiabin Fang (2009). "Enhanced flow boiling heat transfer of FC-72 on micro-pin-finned surfaces". In: *International Journal of Heat and Mass Transfer* 52.13-14, pp. 2925–2931.

Madrid, Francesc, Nadia Caney, and Philippe Marty (2007). "Study of a vertical boiling flow in rectangular mini-channels". In: *Heat Transfer Engineering* 28.8-9, pp. 753–760.

Mattox, Donald M (2010). *Handbook of physical vapor deposition (PVD) processing*. William Andrew.

Mehendale, SS, AM Jacobi, and RK Shah (2000). "Fluid flow and heat transfer at micro-and meso-scales with application to heat exchanger design". In:

Miljkovic, Nenad, Ryan Enright, Youngsuk Nam, Ken Lopez, Nicholas Dou, Jean Sack, and Evelyn N Wang (2013). "Jumping-droplet-enhanced condensation on scalable superhydrophobic nanostructured surfaces". In: *Nano letters* 13.1, pp. 179–187.

Morshed, AKMM, Titan C Paul, and Jamil A Khan (2012). "Effect of cross groove on flow boiling in a microgap". In: *Heat Transfer Summer Conference*. Vol. 44786. American Society of Mechanical Engineers, pp. 457–463.

Morshed, AKMM, Fanghao Yang, M Yakut Ali, Jamil A Khan, and Chen Li (2012). "Enhanced flow boiling in a microchannel with integration of nanowires". In: *Applied Thermal Engineering* 32, pp. 68–75.

Mudawar, Issam (2001). "Assessment of high-heat-flux thermal management schemes". In: *IEEE transactions on components and packaging technologies* 24.2, pp. 122–141.

Ong, Chin Lee, Stephan Paredes, Arvind Sridhar, Bruno Michel, and Thomas Brunschwiler (2014). "Radial hierarchical microfluidic evaporative cooling for 3-d integrated microprocessors". In: *Proc. 4th European Conference on Microfluidics, Limerick*.

Owens, Daniel K and RC Wendt (1969). "Estimation of the surface free energy of polymers". In: *Journal of applied polymer science* 13.8, pp. 1741–1747.

Phan, Hai Trieu (2010). "Effects of nano-and micro-surface treatments on boiling heat transfer". PhD thesis.

Qu, Weilin (2004). *Transport phenomena in single-phase and two-phase micro-channel heat sinks*. Purdue University.

Qu, Weilin and Issam Mudawar (2003). "Measurement and prediction of pressure drop in two-phase micro-channel heat sinks". In: *International Journal of Heat and Mass Transfer* 46.15, pp. 2737–2753.

Qu, Weilin and Abel Siu-Ho (2009). "Experimental study of saturated flow boiling heat transfer in an array of staggered micro-pin-fins". In: *International Journal of Heat and Mass Transfer* 52.7-8, pp. 1853–1863.

Quéré, David (2005). "Non-sticking drops". In: *Reports on Progress in Physics* 68.11, p. 2495.

Reeser, A, A Bar-Cohen, and G Hetsroni (2014). "High quality flow boiling heat transfer and pressure drop in microgap pin fin arrays". In: *International Journal of Heat and Mass Transfer* 78, pp. 974–985.

Revellin, Remi and John R Thome (2007). "Experimental investigation of R-134a and R-245fa two-phase flow in microchannels for different flow conditions". In: *International Journal of Heat and Fluid Flow* 28.1, pp. 63–71.

Revellin, Rémi and John R Thome (2008). "A theoretical model for the prediction of the critical heat flux in heated microchannels". In: *International Journal of Heat and Mass Transfer* 51.5-6, pp. 1216–1225.

Rovira, Antonio, María José Montes, Manuel Valdes, and José María Martínez-Val (2011). "Energy management in solar thermal power plants with double thermal storage system and subdivided solar field". In: *Applied Energy* 88.11, pp. 4055–4066.

Rulison, Christopher (1999). "So you want to measure surface energy". In: *A tutorial designed to provide basic understanding of the concept solid surface energy, and its many complications, TN306/CR*, pp. 1–16.

Schaller, Robert R (1997). "Moore's law: past, present and future". In: *IEEE spectrum* 34.6, pp. 52–59.

Schultz, Mark, Fanghao Yang, Evan Colgan, Robert Polastre, Bing Dang, Cornelia Tsang, Michael Gaynes, Pritish Parida, John Knickerbocker, and Timothy Chainer (2015). "Embedded two-phase cooling of large 3D compatible chips with radial channels". In: *International Electronic Packaging Technical Conference and Exhibition*. Vol. 56901. American Society of Mechanical Engineers, V003T10A007.

Serizawa, Akimi, Ziping Feng, and Zensaku Kawara (2002). "Two-phase flow in microchannels". In: *Experimental Thermal and Fluid Science* 26.6-7, pp. 703–714.

Shah, M Mohammed (1982). "Chart correlation for saturated boiling heat transfer: equations and further study". In: *ASHRAE transactions* 88.

Sheehan, Jessica and Avram Bar-Cohen (2010). "Spatial and temporal wall temperature fluctuations in two-phase flow in microgap coolers". In: *ASME International Mechanical Engineering Congress and Exposition*. Vol. 44441, pp. 1701–1708.

Sheehan, Jessica, Dae Whan Kim, and Avram Bar-Cohen (2009). "Thermal Imaging of Two-Phase Coooled Microgap Channel Wall". In: *International Electronic Packaging Technical Conference and Exhibition*. Vol. 43604, pp. 491–499.

Tadrist, L (2007). "Review on two-phase flow instabilities in narrow spaces". In: *International Journal of Heat and fluid flow* 28.1, pp. 54–62.

Tamanna, Alam and Poh Seng Lee (2014). "Investigation of flow boiling characteristics in expanding silicon microgap heat sink". In: *Fourteenth Intersociety Conference on Thermal and Thermomechanical Phenomena in Electronic Systems (ITherm)*. IEEE, pp. 458–465.

Tamanna, Alam and Poh Seng Lee (2015). "Flow boiling heat transfer and pressure drop characteristics in expanding silicon microgap heat sink". In: *International Journal of Heat and Mass Transfer* 82, pp. 1–15.

Tang, Qian, San-Qiang Shi, and Limin Zhou (2004). "Nanofabrication with atomic force microscopy". In: *Journal of Nanoscience and Nanotechnology* 4.8, pp. 948–963.

Thome, John R (2004). "Boiling in microchannels: a review of experiment and theory". In: *International Journal of Heat and Fluid Flow* 25.2, pp. 128–139.

Ullmann, Amos and Neima Brauner (2007). "The prediction of flow pattern maps in minichannels". In: *Multiphase Science and Technology* 19.1.

Wallis, GB and JH Heasley (1961). "Oscillations in two-phase flow systems". In: *Journal of Heat Transfer* 83.3.

Wang, Guodong and Ping Cheng (2009). "Subcooled flow boiling and microbubble emission boiling phenomena in a partially heated microchannel". In: *International Journal of Heat and Mass Transfer* 52.1-2, pp. 79–91.

Wang, Pengtao, Raikan Dawas, Mohammad Alwazzan, Wei Chang, Jamil Khan, and Chen Li (2017). "Sweating-boosted air cooling using nanoscale CuO wick structures". In: *International Journal of Heat and Mass Transfer* 111, pp. 817–826.

Wenzel, Robert N (1936). "Resistance of solid surfaces to wetting by water". In: *Industrial & Engineering Chemistry* 28.8, pp. 988–994.

Woodcock, Corey, Xiangfei Yu, Joel Plawsky, and Yoav Peles (2015). "Piranha Pin Fin (PPF)—Advanced flow boiling microstructures with low surface tension dielectric fluids". In: *International Journal of Heat and Mass Transfer* 90, pp. 591–604.

Wu, HY and Ping Cheng (2003). "Visualization and measurements of periodic boiling in silicon microchannels". In: *International Journal of Heat and Mass Transfer* 46.14, pp. 2603–2614.

Wu, HY and Ping Cheng (2004). "Boiling instability in parallel silicon microchannels at different heat flux". In: *International Journal of Heat and Mass Transfer* 47.17-18, pp. 3631–3641.

Wu, HY, Ping Cheng, and Hao Wang (2006). "Pressure drop and flow boiling instabilities in silicon microchannel heat sinks". In: *Journal of Micromechanics and Microengineering* 16.10, p. 2138.

Yang, Fanghao, Mark Schultz, Pritish Parida, Evan Colgan, Robert Polastre, Bing Dang, Cornelia Tsang, Michael Gaynes, John Knickerbocker, and Timothy Chainer (2015). "Local measurements of flow boiling heat transfer on hot spots in 3D compatible radial microchannels". In: *International Electronic Packaging Technical Conference and Exhibition*. Vol. 56901. American Society of Mechanical Engineers, V003T10A006.

Yang, Yang and Yasunobu Fujita (2004). "Flow boiling heat transfer and flow pattern in rectangular channel of mini-gap". In: *International Conference on Nanochannels, Microchannels, and Minichannels*. Vol. 41642, pp. 573–580.

Young, Thomas (1805). "III. An essay on the cohesion of fluids". In: *Philosophical transactions of the royal society of London* 95, pp. 65–87.

Yuan, Minzhe, Jinjia Wei, Yanfang Xue, and Jiabin Fang (2009). "Subcooled flow boiling heat transfer of FC-72 from silicon chips fabricated with micro-pin-fins". In: *International Journal of Thermal Sciences* 48.7, pp. 1416–1422.

Zalba, Belen, Jose Ma Marın, Luisa F Cabeza, and Harald Mehling (2003). "Review on thermal energy storage with phase change: materials, heat transfer analysis and applications". In: *Applied thermal engineering* 23.3, pp. 251–283.

Zanini, Stefano, Claudia Riccardi, Marco Orlandi, and Elisa Grimoldi (2007). "Characterisation of SiOxCyHz thin films deposited by low-temperature PECVD". In: *Vacuum* 82.2, pp. 290–293.

Zisman, W Adu (1964). "Relation of the equilibrium contact angle to liquid and solid constitution". In: ACS Publications.